1329

Université de Neuchâtel

Institut de Microtechnique

MONOLITHICALLY INTEGRATED INTERFEROMETER FOR OPTICAL DISPLACEMENT MEASUREMENT

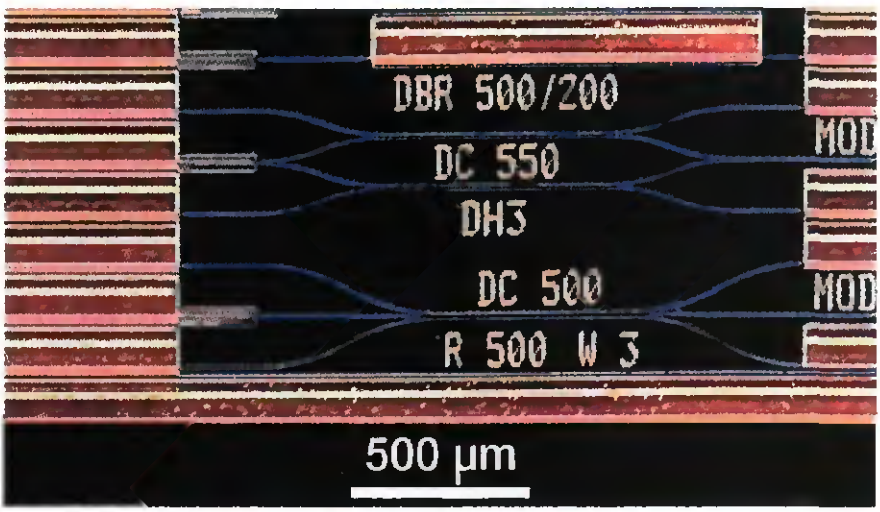

Thèse

Présentée à la Faculté des sciences
pour obtenir le grade de docteur ès sciences

par

Daniel Hofstetter

Neuchâtel, juin 1996

Université de Neuchâtel

Institut de Microtechnique

MONOLITHICALLY INTEGRATED INTERFEROMETER FOR OPTICAL DISPLACEMENT MEASUREMENT

Thèse

Présentée à la Faculté des sciences
pour obtenir le grade de docteur ès sciences

par

Daniel Hofstetter

Neuchâtel, juin 1996

IMPRIMATUR POUR LA THÈSE

Monolithically integrated interferometer for optical displacement measurement

de M. Daniel Hofstetter

UNIVERSITÉ DE NEUCHÂTEL

FACULTÉ DES SCIENCES

La Faculté des sciences de l'Université de Neuchâtel sur le rapport des membres du jury,

Messieurs R. Dändliker, N. de Rooij,
H. Heidrich (Berlin) et H. Zappe (PSI, Zürich)

autorise l'impression de la présente thèse.

Neuchâtel, le 16 août 1996

Le doyen:

R. Dändliker

R. Dändliker

ABSTRACT

A monolithically integrated optical displacement sensor in the GaAs/AlGaAs material system has been developed, fabricated and characterized. The device was a double Michelson interferometer with an integrated light source, photodetectors, couplers and phase shifters. A key point of the work was the development of a single growth-step distributed Bragg reflector laser which served as the light source of the interferometer circuit. Special attention was also directed at the establishment of a bandgap-engineering technique (vacancy-enhanced disordering) allowing the definition of absorbing areas for the pumped laser section and the photodetector and transparent areas for the waveguiding sections and the grating section of the laser. The combination of the vacancy-enhanced disordering and the laser process enabled the fabrication of a fully integrated optical Michelson interferometer with quadrature signal detection. The maximal measurement distance with this double Michelson interferometer was 25 cm, and a maximal resolution of 20 nm was seen. Although using relatively simple standard processes, complex optical functions could be realized on a single chip.

ACKNOWLEDGMENTS

I would like to thank

- R. Dändliker for directing this thesis and for many helpful discussions.
- H.P. Zappe for supervising this work. He introduced me into the basics of cleanroom work as well as into the field of III-V-based integrated optics. Without his patience in revising my English manuscripts, I would have managed neither to publish a paper nor to write my PhD thesis.
- M.T. Gale and H.W. Lehmann, who created a productive atmosphere in their research groups. Many discussions with them and their co-workers J. Söchtig, H. Teichmann, J.E. Epler, and P. Riel were necessary to animate in me the interest for interferometry, III-V-processing, and semiconductor laser fabrication.
- K. Knop for allowing me to carrying out this PhD work at the Paul Scherrer Institute in Zurich.
- H. Schütz, R. Widmer, D. Jeggle, A. Vonlanthen, H. Meier, H.P. Schweizer, R. Stutz, J. Pedersen, and H. Siegwart for their technical and PC support.
- N.F. de Rooij, H. Heidrich, and H.P. Zappe for their interest in this work and also for being members of the jury.
- My family and my friends for their support and patience during my education.

Zurich, June 1996
Daniel Hofstetter

LIST OF PUBLICATIONS

This thesis is an overview of our work in the area of monolithically integrated optical displacement sensing using III-V-semiconductors. Appendix B contains the following reprints of our journal publications.

I D. Hofstetter, H.P. Zappe, J.E. Epler and J. Söchtig, **Single-growth-step GaAs/AlGaAs distributed Bragg reflector lasers with holographically-defined recessed gratings**, *Electron. Lett.*, vol. 30, no. 22, pp. 1858 - 1859, 1994

II D. Hofstetter, H.P. Zappe and J.E. Epler, **Ridge waveguide DBR lasers with non-absorbing grating and transparent integrated waveguide**, *Electron. Lett.*, vol. 31, no. 12, pp. 980 - 982, 1995

III D. Hofstetter, H.P. Zappe, J.E. Epler and P. Riel, **Monolithically integrated DBR laser, detector and transparent waveguide fabricated in a single growth step**, *IEEE Photon. Technol. Lett.*, vol. 7, no. 9, pp. 1022 - 1024, 1995

IV D. Hofstetter, H.P. Zappe, J.E. Epler and P. Riel, **Multiple wavelength Fabry-Pérot lasers fabricated by vacancy-enhanced quantum well disordering**, *Appl. Phys. Lett.*, vol. 67, no. 14, pp. 1978 - 1980, 1995

V D. Hofstetter, H.P. Zappe and R. Dändliker, **A monolithically integrated optical displacement sensor in GaAs/AlGaAs**, *Electron. Lett.*, vol. 31, no. 24, pp. 2121 - 2122, 1995

VI D. Hofstetter, H.P. Zappe and R. Dändliker, **Monolithically integrated Michelson interferometer with direction determination**, to appear in *IEEE Photon. Technol. Lett.*, vol. 8, no. 10, 1996

VII D. Hofstetter, H.P. Zappe and R. Dändliker, **Optical displacement measurement with GaAs/AlGaAs-based monolithically integrated Michelson interferometers**, submitted to *IEEE J. Ligthwave Technol.*, August 22, 1996

CONTENTS

1. INTRODUCTION 1
   1.1 BACKGROUND 1
   1.2 OVERVIEW 2

2. PRINCIPLE OF OPERATION 5
   2.1 THE MICHELSON INTERFEROMETER: A HISTORICAL SUMMARY 5
   2.2 INTEGRATED OPTICAL DISPLACEMENT MEASUREMENT CHIP 6
      2.2.1 Waveguides and layer structure 6
      2.2.2 Directional couplers and Y-couplers 8
      2.2.3 Lasers 8
      2.2.4 Detectors 9
      2.2.5 Phase shifters 9
      2.2.6 The entire interferometer 10
   2.3 INTEGRATION REQUIREMENTS 11
      2.3.1 Transparency of the waveguides 11
      2.3.2 Integration of light sources into PICs 11
      2.3.3 Electrical and optical device isolation 12

3. SIMULATION 16
   3.1 WAVEGUIDES 16
      3.1.1 Effective index approximation 16
      3.1.2 Simulation of the ridge waveguide 19
   3.2 LASERS 21
   3.3 GRATING 22
   3.4 COUPLERS 23
   3.5 INTERFEROMETER 25

4. VACANCY-ENHANCED DISORDERING 29
   4.1 PRINCIPLE AND COMPARISON TO OTHER METHODS 29
      4.1.1 Growth methods 29
      4.1.2 Methods based on QW intermixing 30
   4.2 MECHANISM AND PROCESS 30
      4.2.1 VED mechanism 30
      4.2.2 Process details 31
   4.3 PHOTOLUMINESCENCE RESULTS 32
   4.4 MULTIPLE WAVELENGTH FABRY-PEROT LASERS 34

5. DBR LASERS 38
   5.1 PRINCIPLE OF OPERATION AND FEATURES 38
   5.2 GRATING FABRICATION 40
   5.3 DEVICE BEHAVIOR 42

5.3.1 Electrical and spectral properties 42
5.3.2 Temperature tuning 44
5.4 INTEGRATION 46

6. MONOLITHICALLY INTEGRATED OPTICAL DISPLACEMENT MEASUREMENT CHIP 51
6.1 PROCESS RECAPITULATION 51
6.1.1 Layer structure 51
6.1.2 Interferometer process 52
6.2 CHIP DESCRIPTION 55
6.3 MEASUREMENT SETUP 56
6.4 MEASUREMENT RESULTS 58
6.5 DIRECTION DETERMINATION 60

7. CONCLUSIONS 65
7.1 POSSIBLE APPLICATIONS 65
7.2 IMPROVEMENTS 66

APPENDIX A 68
A.1 CALCULATIONS 68
A.1.1 3x3-coupler solved by coupled mode theory 68
A.1.2 Interferometer with parasitic reflection in sensing arm 69
A.2 SPECIAL PROCESS STEPS 71
A.2.1 Waveguide dry etching 71
A.2.2 Metals 71
A.3 FULL PROCESS DESCRIPTIONS 72
A.3.1 Broad area laser process 72
A.3.2 Fabry-Pérot laser process 74
A.3.3 DBR laser process 77
A.3.4 Interferometer process 82

APPENDIX B 91
B.1 ABSTRACTS OF PUBLICATIONS I - VII 91
B.2 PUBLICATIONS I - VII 95

1. INTRODUCTION

Contactless optical displacement sensing has a large field of industrial and scientific applications. These include, for example, precise mechanical measurement systems, the monitoring of moving stages of CNC machine tools, and also the displacement control of mobile parts in microsystems. One possibility to optically realize displacement measurements is by use of the Michelson interferometer. In this device, the interference between a reference and measurement beam, which are produced by a fixed reference and a movable object mirror, respectively, allows detection of the displacement of the latter. The following work describes the design, fabrication and characterization of a GaAs/AlGaAs-based monolithically integrated displacement sensor. The final device is configured as a double Michelson interferometer and consists of a laser, waveguides, detectors and phase shifters.

1.1 BACKGROUND

The first experiment with a Michelson-type interferometer was carried out by A.A. Michelson in 1881 [1], [2], [3]. This historical experiment proved that the speed of light was not influenced by the relative motion of the earth in a hypothetical ether. Since, in those days, only gas vapor discharges were available as light sources, a displacement measurement at distances up to 1 meter was limited by the coherence length. Today, with the use of highly coherent lasers, we are able to measure an interference signal at a distance of several meters without any obvious reduction of the signal contrast.

Following the deployment of semiconductor lasers, Michelson interferometers based on integrated optics became very attractive for optical displacement measurement, predominantly because of their reduced size and enhanced robustness; numerous types have been fabricated and tested. One of these approaches has been described by Ulbers [4] and was commercially available (Hommelwerke GmbH) for some time. The device consisted of a double Michelson interferometer on a silicon chip; the light was guided through planar waveguides. One of the reference arms contained an additional phase shifter to produce two signals in phase quadrature. An external gradient index (GRIN) lens was used for the collimation of the measurement beam; a temperature- and current-stabilized diode laser served as light source. Finally, an external dual-photodetector was necessary to measure the two interferometer signals. The packaged measurement head with all interferometer components was 65 mm long and 17 mm in diameter. The maximal measurement distance of this interferometer was 250 mm with a resolution of 250 nm; a maximal measurement speed of 200 mm/s was guaranteed by the manufacturer.

The integrated optical Michelson interferometer fabricated by Jestel [5] (University of Dortmund, FRG) used ion-exchanged stripe waveguides on a glass substrate, thermooptic phase modulators to define the relative phase shift between the two reference arms and directional couplers to divide the incoming light into reference and sensing beams. This device was driven with a diode laser as well, used external photodetectors and one externally-mounted beam-shaping element. Optical heterodyning by single sideband detection using a staircase modulating function which was applied to one phase modulator enabled the detection of displacements with a very high resolution, 1 nm.

Displacement detection is also possible with Mach-Zehnder type interferometers; Voirin [6] (CSEM Neuchâtel) reported an integrated optical Mach-Zehnder interferometer for displacement sensing. This sensor was fabricated in glass with ion-exchanged stripe waveguides and wavelength-stabilized within to 10^{-6}. The usual external elements (laser, detectors, and GRIN lens) were necessary to operate the interferometer. A maximal measurement distance of 120 mm with a resolution of ±100 nm was reported.

Recently, Ura [7] published a monolithically integrated optical position sensor. This III-V-semiconductor-based device was configured as a Michelson interferometer and consisted of a DFB laser, planar waveguides and grating couplers. The grating coupler served as beam splitter and also as collimation lens for the measurement beam. Despite the restricted measurement distance of 20 mm and the lack of a direction determination, this element demonstrated the possibility of monolithically integrating active and passive optical components.

In this work, we discuss a monolithically integrated double Michelson interferometer, which unites active optical components, such as lasers, phase shifters and detectors with passive ones, waveguides and couplers, on a single chip. This goal could only be realized through the use of III-V-semiconductors. The advantages of monolithically integrated circuits include: no tedious alignment procedures, extremely small physical size and high robustness. In addition, such devices may be fabricated in mass production. Furthermore, the emission wavelength of lasers fabricated in the GaAs/AlGaAs material system can be chosen between 760 nm and 860 nm. Thus the wavelength can be set near to the Rb or Cs gas absorption lines, allowing frequency stabilization using these standards.

1.2 OVERVIEW

The integration of active and passive optical components into a photonic integrated circuit depends strongly on the process compatibility of the single elements. Areas with different bandgaps were necessary, for example, to fabricate lasers and transparent waveguides on the same piece of semiconductor. Furthermore, a special laser type with only one cleaved facet

mirror had to be developed. Finally, since the signals to be measured were very small, excellent isolation between laser and detector was needed. These principal integration requirements, and some general aspects of the single components, are described in chapter 2 of this dissertation.

Small changes in the physical dimensions or structure of photonic components can lead to significant changes in device behavior; thus, the most suitable design must be found by the use of simulation programs. This software was partly commercially available, but part of it had to be developed during this work. In chapter 3, we will have a closer look at the simulation of waveguides, lasers, couplers, the grating and also the entire interferometer.

There are several techniques to define sections with a different bandgap on the same chip. Most of them are relatively sophisticated. Among these techniques, those using quantum well intermixing are suitable because they can be done after growth with few additional processing steps. For this dissertation, we developed a vacancy-enhanced disordering process which will be described in detail in chapter 4. The processing, some fabricated laser devices and their features will be presented.

The special light source of our interferometer circuit is a distributed Bragg reflector (DBR) laser. The fabrication and testing of this circuit element will be addressed in chapter 5. With regard to the integration of DBR laser and interferometer, a first simple monolithically integrated device, consisting of laser, waveguide and monitoring photodiode will be described.

Different kinds of interferometers were fabricated; the first were single Michelson interferometers with no direction determination. In a second fabrication run, double Michelson interferometers with one phase-shifted reference arm were produced. This configuration allowed us to detect both the direction and the magnitude of the movement. The two interferometer types were characterized in terms of coherence length of the employed laser, signal contrast and maximal resolution. The most interesting interferometer results will be shown in chapter 6 of this work.

In the conclusions of chapter 7, we will give an outlook of future potential applications, possible improvements of the single components and the whole system. The performance of the presented interferometers will be compared to that of previously mentioned similar devices.

The appendix contains some additional information such as descriptions of special processing steps, detailed processing plans of all used processes, and algebraic calculations.

[1] A.A. Michelson, "The relative motion of the earth and the luminiferous ether", *Amer. J. Sci.*, vol. 22, pp. 120 - 129, 1881

[2] A.A. Michelson, "On the application of interference methods to spectroscopic measurements", *Phil. Mag.*, vol. 34, pp. 280 - 299, 1892

[3] M. Born and E. Wolf, "Interference and interferometers", *Principles of optics*, Pergamon Press, 6th edition, pp. 256 - 323, 1984

[4] G. Ulbers, "An integrated optics sensor on silicon for the measurement of displacement, force and refractive index", *Proc. SPIE*, vol. 1506 "Micro-Optics II", pp. 99 - 110, 1991

[5] D. Jestel, A. Baus and E. Voges, "Integrated-optic interferometric microdisplacement sensor in glass with thermo-optic phase modulation", *Electron. Lett.*, vol. 26, pp. 1144 - 1145, 1990

[6] G. Voirin, L. Falco, O. Boillat, O. Zogmal, P. Regnault and O. Parriaux, "Monolithic double interferometer displacement sensor with wavelength stabilization", *Proc. European Conference of Integrated Optics 93*, pp. 12-28 - 12-29, 1993

[7] S. Ura, T. Suhara and H. Nishihara, "Integrated-optic interferometer position sensor", *IEEE J. Lightwave Technol.*, vol. 7, pp. 270 - 273, 1989

2. PRINCIPLE OF OPERATION

In the first section of this chapter, we will describe the basic concepts of displacement sensing using Michelson interferometers. The second section will treat the individual components and the working principle of an integrated optical interferometer. It includes some aspects of waveguide fabrication; the fabrication of all active devices will be described in separate chapters. The last section will briefly illustrate the requirements for monolithic interferometer production.

2.1 THE MICHELSON INTERFEROMETER: A HISTORICAL SUMMARY

Contactless displacement measurements can basically be carried out by time-of-flight measurements, by triangulation or by interferometric methods. The last approach often uses the classical Michelson interferometer, in which the light is divided into two orthogonal beams by a beam splitter. As shown in figure 2.1, the two light rays are then reflected by a fixed reference mirror and a movable object mirror, respectively. After passing through the beam splitter again, they are guided into the same interferometer arm and there

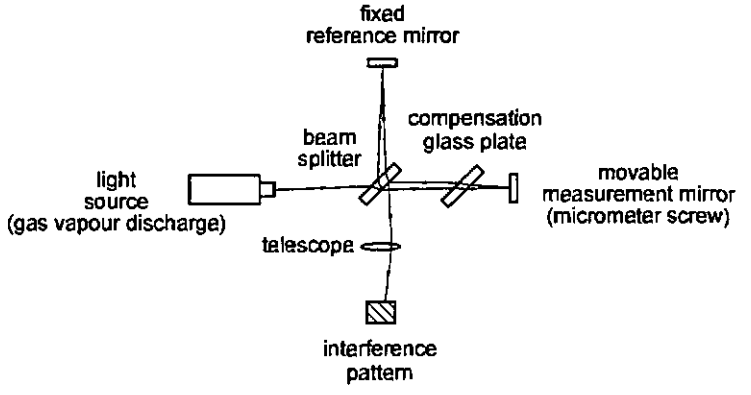

Fig. 2.1 - The classical experimental setup used by A.A. Michelson (1881)

produce an interference pattern. The investigation of this interference pattern is useful for either displacement or spectroscopic measurements. Counting the moving interference fringes allows detection of the displacement of the measurement mirror. A measurement of the fringe contrast as a function of mirror displacement (autocorrelation function) can be used to determine the linewidth of the light source (spectroscopic measurement). However, the first application of this experiment in 1881 was neither a displacement nor a spectroscopic measurement, but rather a proof for the non-existence of the luminiferous ether.

In the experimental setup used by Michelson, an additional glass plate in the measurement arm compensated the two passes of the light in the reference arm through the beam-splitting glass plate. The contrast of the interference fringes was measured by comparing it with the one produced by two parallel glass plates. The signal contrast is often referred to as visibility, possibly because the human eye was used as detector in this experiment. Using nearly collimated light resulted in a circular interference pattern, which was helpful for the determination of the movement direction. The latter was indicated by the shrinking or the expansion of the interference rings.

In today's approaches, the eye is replaced by photodetectors. The trick to electrically detect a direction change consists thus of using two photodetectors instead of only one. Both of them are placed in the interference pattern and are separated by one quarter of the fringe period.

When measuring the autocorrelation function of a light source using a Michelson interferometer, interference fringes can be seen as long as the difference in the optical path length between reference and measurement arm is smaller than the *coherence length* of the light source. If the path length difference is zero, the mirrors are said to be in optical contact. Since all his light sources were gas vapor discharges using, for instance, O_2, H_2, Na, Cd, or Hg, Michelson could measure interference using only moderate deviations from this optical contact criterion. For the red Cd-line for example, which exhibited a nearly ideal, Gaussian-shaped autocorrelation function and therefore also a Gaussian lineshape, the maximal possible deviation was around 0.5 m. This corresponded to a coherence length of 1 m and a linewidth of 500 MHz. Other discharges, such as Na, showed more complicated autocorrelation functions and lineshapes.

When stabilizing their laser light source on a gas absorption line, modern laser interferometers, for example the LAS 780 laser interferometer of Hytron [8], can be used as length standards; their accuracy is better than 10^{-8}.

2.2 INTEGRATED OPTICAL DISPLACEMENT MEASUREMENT CHIP

By taking advantage of the small size of a semiconductor laser, we can use it as the light source of an integrated optical Michelson interferometer. In such integrated optical devices, the light propagates in waveguides instead of the free space. This requires the fabrication of waveguides as well as of active components. These subjects will be addressed in the following section.

2.2.1 Waveguides and layer structure

As seen in the introduction of this work, many attempts have been made to fabricate integrated optical interferometers. So far, most of them were not monolithically integrated in the strict sense of the word; they did not combine light emitters and detectors with the interferometer on the same piece of

material. Since efficient light emitters can not yet be fabricated in silicon or glass, we decided to use III-V-semiconductors as substrate material for a truly monolithic chip. The successful use of these materials for semiconductor lasers allowed the fabrication of other kinds of optically active and passive structures such as waveguides, beam splitters, phase shifters and detectors. Basis for the fabrication of all these components is the definition of a waveguiding structure.

A slab waveguide is a planar structure consisting, in general, of a waveguide core with a slightly higher refractive index and two (upper and lower) cladding layers with a lower refractive index. In the GaAs/AlGaAs material system, we have the possibility of growing epitaxial layers with continually changing composition and refractive index. Depending on the Al mole fraction, material with a refractive index between 3.64 for GaAs and 2.94

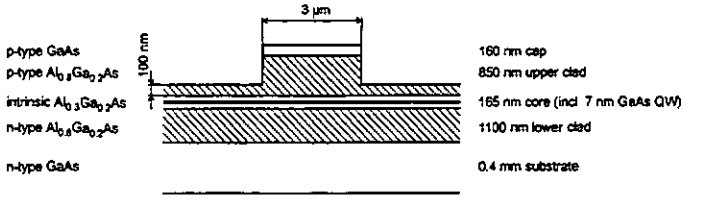

Fig. 2.2 - Cross section through a ridge waveguide structure in the GaAs/AlGaAs material system.

for AlAs (measured at $\lambda = 820$ nm) can be grown on each other without any strain [9]. This is due to the nearly perfect lattice matching between GaAs and AlAs; the two materials have a lattice mismatch of only 0.127 % [10]. As shown in figure 2.2, we used an $Al_{0.3}Ga_{0.7}As$ layer ($n = 3.421$) for the core of our slab waveguides while the cladding layers consisted of $Al_{0.8}Ga_{0.2}As$ ($n = 3.112$). This three layer slab waveguide structure led to optical confinement in the vertical direction.

In the horizontal direction, confinement could be achieved by using ridge waveguides. Such ridges were fabricated using a dry etching process (see appendix). They had a width of 3 µm, and the residual clad thickness above the core was approximately 100 nm. This thickness was an important design parameter for the waveguide; it allowed the customization of the mode behavior of a single waveguide or the coupling strength between two neighboring waveguides. All curves used in our interferometers had radii of 500 µm which appeared to be the absolute minimum for acceptable radiation loss. Smaller curve radii require a strongly index-guided waveguide structure in order to reduce radiation loss in the curves. This stronger index-guiding can be achieved through a deeper waveguide etch, if necessary through the core. By this measure, the relative index step between the effective indices under the ridge and beside the ridge can be enlarged considerably. This allows the realization of smaller curve radii. As a possible drawback, we have

to deal with multimode waveguides. In section 3.1, some design rules and examples of such waveguiding structures will be presented.

Another important detail is the very thin quantum well (QW) layer in the center of the core. This layer determines the absorption edge of the material and therefore also the emission wavelength of electro- or photoluminescence (PL). In chapter 4, we will see how a partial intermixing of this layer can be used to selectively blue-shift the PL spectrum of the material. In our case, the waveguiding areas typically had a 25 nm blue-shifted absorption edge in order to reduce absorption loss due to band-edge absorption. Furthermore, the use of a QW helps to decrease the threshold current density of semiconductor lasers; a reduction by a factor of 10 with respect to the devices without a QW has been reported in the literature [11]. The layers of our slab waveguides were grown by metalorganic vapor phase epitaxy (MOVPE). Substrate and lower cladding were n-doped, the core with the QW remained not-intentionally-doped, and the upper cladding layer was p-doped. In order to form good p-contacts, an additional highly p-doped, thin cap layer was employed.

2.2.2 Directional couplers and Y-couplers

The directional couplers [12] used in our interferometer circuits consisted of two parallel ridge waveguides, 1 μm apart. Because of the small separation, the electric fields in the two waveguides are coupled to each other, and the resulting electric field overlap transports energy from one waveguide into the other. The length of the parallel section required for a particular splitting ratio can be simulated approximately by using coupled mode theory. Our preliminary experiments showed, however, that the coupling ratio of the couplers of a certain design varied by ±20 %. This large variation was understood as process-dependent: a small difference of the etch depth changes the confinement of the optical mode in the waveguides and therefore the coupling strength between them. For our waveguide design, a coupling length of 500 μm usually resulted in a splitting ratio of around 50:50 %.

As an alternative to the directional couplers, we used also Y-couplers for the splitting of the incoming laser light into reference and sensing beams. A Michelson interferometer using these elements has, as opposed to the one using a directional coupler, an additional intrinsic loss of 3 dB; but, on the other hand, the waveguide loss of the directional coupler is much larger due to the longer optical path. The design of our Y-couplers was very simple: no tapered section was used to support a well-defined mode before splitting [13]. We employed two curved waveguides with the same curve radius to split the light. This non-ideal design resulted in some variations of the splitting ratio, similar to that observed with the directional couplers. The reason for these variations is likely an undesired mode-conversion in the splitting region of the coupler.

2.2.3 Lasers

All further components of the interferometer circuit were based on the layer structure and the waveguide concept described above. For optically active devices such as lasers, detectors or phase shifters, dopants forming a p-i-n-junction were required. Details concerning the operation principle of semiconductor lasers can be found in many textbooks and publications [14], [15], [16], [17]. In such semiconductor lasers, the laser cavity is typically formed by a pair of cleaved facet mirrors. As we will see in chapter 5, such a Fabry-Pérot laser is not an ideal candidate for the monolithic integration with an optical integrated circuit. Because of its potential for monolithic integration, its relatively simple fabrication, and its excellent spectral properties, we decided to use a so-called distributed Bragg reflector laser (DBR-laser) [18]; here the laser cavity is built between one cleaved facet and one wavelength-selective Bragg mirror. Processing and characterization details will be presented in chapter 5.

2.2.4 Detectors

The detectors of this integrated optical circuit were configured as waveguide photodiodes. They had the same, unshifted absorption edge as the material of the pumped laser section. The working principle of such a photodetector is the inverse of that of a semiconductor laser [19], [20]: one absorbed photon produces an electron-hole pair; these two particles are separated by the electric field of the p-i-n-junction and generate a measurable photocurrent. The detectors used in these experiments were 500 μm long and reverse biased at -12 V. The leakage dark current density at this reverse voltage was typically less than 10 mA/m^2.

2.2.5 Phase shifters

In each of the two reference arms of our double interferometer, we inserted a phase shifter. Its working principle is based on the quantum-confined Stark effect (QCSE) [19], [21], [22]. The QCSE uses the exciton absorption peaks of the QW, which shift to smaller energy when an electric field is applied perpendicular to the substrate plane. The final effect is an electric field-induced, variable red-shift of the absorption edge, or, when measuring at a fixed wavelength, a field-dependent change of the absorption index of the material. As can be calculated using the Kramers-Kronig-relations, such a change of the absorption index is always coupled to a change of the real refractive index or the optical path length. We use this change in optical path length for the generation of a variable phase shift between the two interferometer signals.

The phase shifters in our interferometers were 340 μm long; this length, and the use of only one QW, allowed a one-pass phase shift of $\pi/16$, which was just one quarter of the desired value. To achieve with these shifters the maximal possible refractive index change of $\Delta n = 0.5 \times 10^{-3}$, a reverse voltage

of -12 V had to be applied. Under these conditions, an intensity reduction of around 10 dB was seen in the reference beam. As we will see in chapter 6, this intensity reduction was not overly detrimental for the measurement of an interference signal.

2.2.6 The entire interferometer

The arrangement of the individual components in a so-called double Michelson interferometer is very similar to that presented in the work of Jestel. As shown in the following figures, the light of the DBR laser is split by

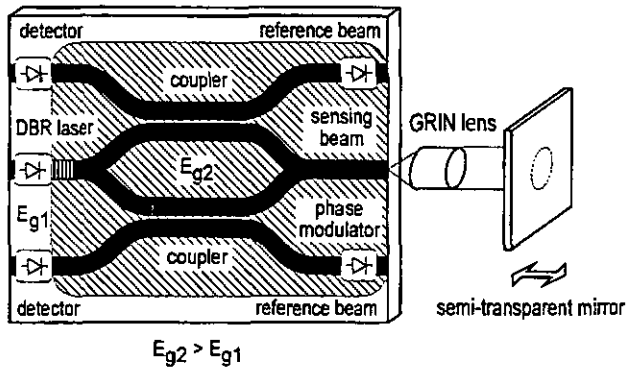

Fig. 2.3 - The arrangement of the single components to a double Michelson interferometer with directional couplers

a first Y-coupler into two nearly independent single Michelson interferometers, which share only light source and sensing beam. In both of these interferometers, the light then passes through either a directional

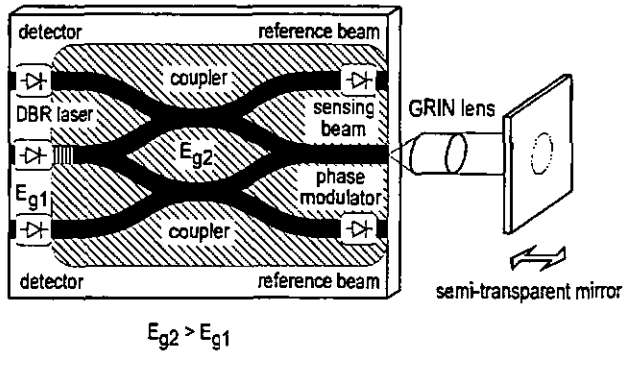

Fig. 2.4 - The arrangement of the components to a double Michelson interferometer with Y-couplers

coupler (figure 2.3) or two cascaded Y-couplers (figure 2.4). These couplers divide the light into two reference and two sensing beams each; the latter are combined into a single sensing beam through a final Y-coupler. The light of

each reference beam is then reflected at the cleaved facet mirror, passes again through the coupler(s), interferes with a fraction of the light reflected by the external semi-transparent mirror, and is guided into the corresponding upper or lower photodetector.

In addition, we used two phase shifters in each reference beam in order to allow a variation of the intrinsic phase between reference and sensing beam. As mentioned in the previous section, the length of these shifters was a little too short for switching between 0° and 90° phase difference; we achieved a phase shift of only 20°. An improvement of the phase shifter behavior is possible either through a longer phase shifter or through the use of more quantum wells. While the first method increases also the parasitic intensity modulation, the second generates high laser threshold currents. The total length of the entire interferometer was 1.95 mm for the Y-coupler-based devices and 2.6 mm for the directional coupler-based interferometers. The width of these devices was 0.35 mm.

2.3 INTEGRATION REQUIREMENTS

The monolithic integration of active and passive optical components into a photonic integrated circuit (PIC) requires, in general, a technique to define areas with different bandgap energy, the development of an integratable light source, and a good optical and electrical isolation between light emitters and detectors. Since the technologies and processes of the first two requirements are subject of special chapters, we give in this section only a brief overview and motivation.

2.3.1 Transparency of the waveguides

In order to produce waveguides which are transparent for the emission wavelength of the monolithically integrated laser, we have to define areas with a different bandgap energy across the chip. One possibility to solve this problem is selective area growth [23]. This method uses structured SiO_2 masks allowing simultaneous epitaxy with different growth rates, and, therefore, the growth of QWs with different thicknesses. Other possibilities are selective partial intermixing of the QW using impurities [24], [25] or vacancies [26]. The main advantage of the two latter methods is that they require no additional regrowth. We decided to use the vacancy-enhanced disordering (VED) process to achieve the selective intermixing of the QW because it appeared to be realizable in the most straight-forward manner. In chapter 4, we will extensively discuss the processing and the measurement results of these experiments.

2.3.2 Integration of light sources into PICs

A second important step towards the monolithic integration of light emitters and optical interferometers is the development of an integratable,

process-compatible, stable light source. In the past, numerous approaches, including evanescent coupling between waveguides and absorbing regions (requiring an additional impedance matching layer and regrowth) [27], [28], butt coupling between laser and photodetector (needing a mirror dry etch technique) [29] or the use of surface emitting lasers and photodiodes (requiring high-quality dry-etched mirrors) [30], have been developed to address the integration issue. In our work, the use of a single-growth-step DBR laser looked most promising with respect to both process compatibility and feedback stability. The development and the characterization of this DBR laser and its integration within a simple PIC will be presented in chapter 5.

2.3.3 Electrical and optical device isolation

In interferometric systems, very small optical signals often have to be measured. This requires good optical and electrical isolation between laser and detector. For obtaining electrical isolation, we employed an ion implantation process (H^+, $4x10^{15}$ cm^{-2}, 40/70/100 keV) [31] during which all waveguiding areas remained unimplanted, except 2 μm wide stripes across the waveguides. These small implanted stripes are shown schematically in figure 2.5; they destroyed the electrical connection between active laser region and passive interferometer region, while the optical connection was not

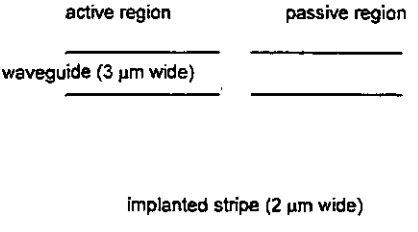

Fig. 2.5 - Schematic top view of an implanted stripe across the waveguide

adversely affected. To protect the waveguides from being implanted, we used a 2.8 μm thick photoresist layer; this photoresist mask could be removed after implantation by an oxygen plasma ash. The optical loss induced through the implanted stripe was on the order of 1 - 2 dB. Optical isolation was accomplished by a deep isolation trench between laser and detector; this trench was filled with the p-metalization layers.

[8] Hytron laser interferometer LAS 780, product description, in German

[9] J.-P. Weber, "Propagation of light in periodic structures: application of the surface-emitting laser diode", *Dissertation UC Berkeley*, 1990

[10] S.M. Sze, *"Physics of semiconductor devices"*, J. Wiley & Sons, 2nd edition, pp. 848, 1981

[11] N. Holonyak, Jr., R.M. Kolbas, R.D. Dupuis, and P.D. Dapkus, "Quantum-well heterostructure lasers", *IEEE J. Quantum Electron.*, vol QE-16, no. 2, pp. 170 - 186, 1980

[12] S. Somekh, E. Garmire, A. Yariv, H.L. Garvin, and R.G. Hunsperger, "Channel optical waveguide directional couplers", *Appl. Phys. Lett.*, vol. 22, no. 2, pp. 46 - 47, 1973

[13] M. Izutsu, Y. Nakai, and T. Sueta, "Operation mechanism of the single-mode optical-waveguide Y-junction", *Optics Lett.*, vol 7, no.3 pp. 136 - 138, 1982

[14] P. Zory, *"Quantum Well Lasers"*, Academic Press, Boston, 1993

[15] A. Yariv, *"Optical Electronics"*, Saunders College Publishing, 4th edition, pp. 552 - 591, 1991

[16] M.B. Panish, I. Hayashi, and S. Sumski, "Double-heterostructure injection lasers with room-temperature thresholds as low as 2300 A/cm^2 ", *Appl. Phys. Lett.*, vol 16, no. 8, pp. 326 - 327, 1970

[17] R.G. Hunsperger, *"Integrated Optics: Theory and Technology"*, 3rd edition, Springer Verlag, pp. 184 - 192, 1991

[18] F.K. Reinhart, R.A. Logan and C.V. Shank, "GaAs-$Al_xGa_{1-x}As$ injection lasers with distributed Bragg reflectors", *Appl. Phys. Lett.*, vol. 27., no. 1, pp. 45 - 48, 1975

[19] D.A.B. Miller, D. S. Chemla, T.C. Damen, A.C. Gossard, W. Wiegmann, T.H. Wood, and C.A. Burrus. "Band-edge electroabsorption in quantum well structures: the quantum-confined Stark effect", *Phys. Rev. Lett.*, vol. 53, no. 22, pp. 2173 - 2176, 1984

[20] D. Moss, F. Ye, P.E. Jessop, J.G. Simmons, H.G. Champion, I. Templeton, and F. Chatenoud, "Ridge waveguide quantum-well wavelength

division demultiplexing detector with four channels", *IEEE Photon. Technol. Lett.*, vol. 4, no. 7, pp. 756 - 759, 1992

[21] M. Glick, F.K. Reinhart, G. Weimann, and W. Schlapp, "Quadratic electro-optic light modulation in a GaAs/AlGaAs multiquantum well heterostructure near the excitonic gap", *Appl. Phys. Lett.*, vol. 48, no. 15, pp. 989 - 991, 1986

[22] J. S. Weiner, D.A.B. Miller, and D.S. Chemla, "Quadratic electro-optic effect due to the quantum-confined Stark effect in quantum wells", *Appl. Phys. Lett.*, vol. 50, no. 13, pp. 842 - 844, 1987

[23] K. Yamaguchi, K. Okamoto, and T. Imai, "Selective area growth of GaAs be metalorganic chemical vapor deposition", *Jpn. J. Appl. Phys.*, vol 24, no. 12, pp. 1666 - 1671, 1985

[24] K. Meehan, P. Gavrilovic, N. Holonyak, Jr., R.D. Burnham, and R.L. Thornton, "Stripe-geometry $Al_xGa_{1-x}As$ quantum well heterostructure lasers defined by Si diffusion and disordering", *Appl. Phys. Lett.*, vol. 46, no. 1, pp. 75 - 77, 1985

[25] R.L. Thornton, J.E. Epler, and T.L. Paoli, "Monolithic integration of a transparent dielectric waveguide into an active laser cavity by impurity-induced disordering", *Appl. Phys. Lett.*, vol. 51, no. 24, pp. 1983 - 1985, 1987

[26] J. Beauvais, S.G. Ayling, and J.H. Marsh, "Low-loss extended cavity lasers by dielectric cap disordering with a novel masking technique", *IEEE Photon. Technol. Lett.*, vol. 4, no. 4, pp. 372 - 373, 1993

[27] R.J. Deri, W. Doldissen, R.J. Hawkins, R. Bhat, J.B.D. Soole, L.M. Schiavone, M. Seto, N. Andreadakis, Y. Silberberg and M.A. Koza, "Efficient vertical coupling of photodiodes to InGaAsP rib waveguides", *Appl. Phys. Lett.*, vol. 58, pp. 2749 - 2751, 1991

[28] K.-Y. Liou, U. Koren, E.C. Burrows, M. Oron, B.J. Miller, M. Young, G. Raybon and C.A. Burrus, "Operation of integrated InGaAsP/InP optical amplifier-monitoring detector with feedback control circuit", *IEEE Photon. Technol. Lett.*, vol 2, pp. 878 - 880, 1990

[29] P. Vettinger, M.K. Benedict, G.-L. Bona, P. Buchmann, E.C. Cahoon, K. Dätwyler, H.-P. Dietrich, A. Moser, H.K. Seitz, O. Voegeli, D.J. Webb and P. Wolf, "Full-wafer technology - a new approach to large-scale laser fabrication and integration", *IEEE J. Quantum Electron.*, vol. QE-27, pp. 1319 - 1331, 1991

[30] C.-H. Chen and S.-C. Lee, "Monolithic integration of an AlGaAs/GaAs surface emitting laser diode and a photodetector", *Appl. Phys. Lett.*, vol. 59, pp. 3592 - 3594, 1991

[31] J.C. Dyement, J.C. North, and L.A. D'Asaro, "Optical and electrical properties of proton-bombarded p-type GaAs", *J. Appl. Phys.*, vol. 44, no. 1, pp. 207 - 213, 1973

3. SIMULATION

This chapter will treat the simulation of different component parameters and also the behavior of the entire interferometer. The output of our simulation software was the basis for device design and fabrication. Although, in special cases, only a moderate agreement between calculation and experiment was seen, such calculations helped us to obtain a better understanding of the device and to find suitable starting conditions for our experiments.

3.1 WAVEGUIDES

As shown in the waveguide cross section of figure 3.1, we used for this work ridge waveguides with a width of $w = 3\ \mu m$, a core thickness of $2h = 165$ nm; the residual clad thickness, t, had to be determined by calculation.

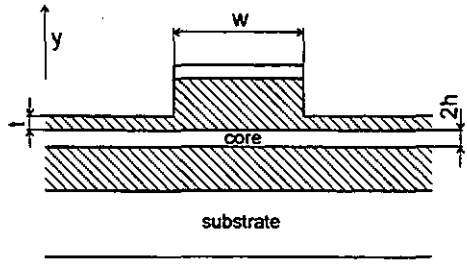

Fig. 3.1 - Cross section and simulated parameters of a ridge waveguide

After epitaxial growth in the y-direction, we therefore had only w and t as free parameters; these could be simulated by using two different software methods. Both residual clad thickness and ridge width define whether a waveguide with a certain core thickness and pre-defined refractive indices supports only its zero-order mode or not. A waveguide in which only the zero-order mode can propagate is referred to as a monomode waveguide. For interferometer circuits, the use of such monomode waveguides is necessary because of the otherwise random phase between reference and sensing beam, but also for their easier theoretical treatment and for increased signal contrast.

3.1.1 Effective index approximation

With the first method, which is called the effective index approximation, we calculated the ridge widths for waveguides which can support the n-th order mode. In order to obtain these results, we solved two independent one-dimensional planar waveguide problems. Figure 3.2 shows a zig-zagging mode, which propagates in a planar (or slab) waveguide of thickness 2h and

refractive indices n_{core} and n_{clad}. The propagation direction is z, and the angle between the zig-zag-mode and the y-direction is θ.

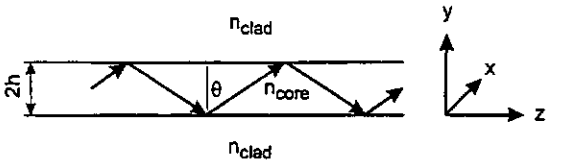

Fig. 3.2 - Definition of the axes in a planar or slab waveguide with zig-zag-mode

Solving the slab waveguide problem means that we have to solve a somewhat simplified wave equation for a traveling TE plane wave. The mathematics which is necessary to calculate the field distribution can be looked up in reference [32]. Since the dependence on time and propagation direction are sinusoidal, and the variation in the x-direction is zero ($\partial E_x(x,y)/\partial x = 0$), we find that

$$E_x(x,y) = E(y) = E_0 \cdot e^{-ik_y y} \tag{3.1}$$

describes the solution of the electric field distribution in the y-direction. In (3.1) , k_y is the propagation constant in the y-direction. Within the core ($|y| < h$), k_y is a real number, $k_{y_{core}}$, which gives an oscillating behavior

$$E_x(y) = E_{core} \cdot \cos(k_{y_{core}} y) \tag{3.2}$$

for E(y); outside the core ($|y| > h$), k_y is an imaginary number, $-i \cdot k_{y_{clad}}$, resulting in an exponential decaying behavior

$$E_x(y) = E_{clad} \cdot e^{-k_{y_{clad}}|y|} \tag{3.3}$$

for E(y). Figure 3.3 shows the field distribution with the corresponding

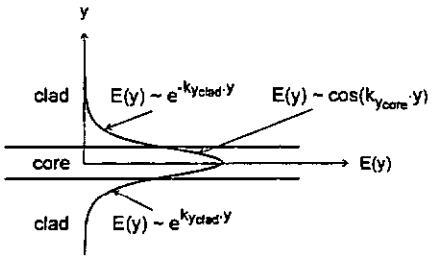

Fig. 3.3 - The electric field distribution in a slab waveguide

propagation constants. The continuity of the electric fields and of their derivatives at y = ±h results in an eigenvalue equation

$$2hk_{y_{core}} - m\pi = 2 \cdot \arctan\left(\frac{k_{y_{clad}}}{k_{y_{core}}}\right) \tag{3.4}$$

in which m is the waveguide mode index.

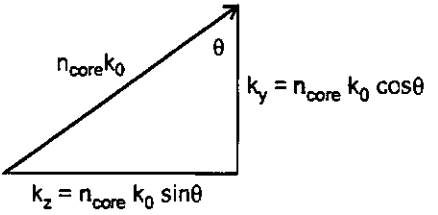

Fig. 3.4 - Propagation constants of a zig-zagging mode in a slab waveguide

The propagation constant, $k_0 = 2\pi/\lambda_0$, of figure 3.4 is defined as the wavenumber of a wave propagating in vacuum. Using figure 3.4 and the definition of the effective refractive index, $n_{eff} = n_{core}\cdot\sin\theta$, which corresponds to the propagation constant seen by the traveling wave in the guide, k_z, we can write the real propagation constant of the core in the following form

$$k_{y_{core}} = k_0\sqrt{n_{core}^2 - n_{eff}^2} \tag{3.5}$$

Similarly we obtain the number for the propagation constant of the exponentially decaying tail

$$k_{y_{clad}} = k_0\sqrt{n_{eff}^2 - n_{clad}^2} \tag{3.6}$$

Inserting the last two equations into (3.4), we end with

$$2hk_0\sqrt{n_{core}^2 - n_{eff}^2} - m\pi = 2 \cdot \arctan\sqrt{\frac{n_{eff}^2 - n_{clad}^2}{n_{core}^2 - n_{eff}^2}} \tag{3.7}$$

For an asymmetric slab waveguide (which has been realized beside the ridge) with two different refractive indices, n_{upclad} and $n_{lowclad}$, in the cladding layers, we can evaluate a more complicate expression

$$2hk_0\sqrt{n_{core}^2 - n_{eff}^2} - m\pi = \arctan\sqrt{\frac{n_{eff}^2 - n_{upclad}^2}{n_{core}^2 - n_{eff}^2}} + \arctan\sqrt{\frac{n_{eff}^2 - n_{lowclad}^2}{n_{core}^2 - n_{eff}^2}} \tag{3.8}$$

for the determination of the effective index.

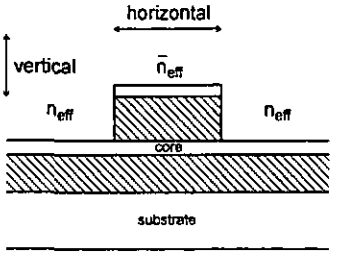

Fig. 3.5 - Refractive indices for the effective index approximation in the horizontal direction

The above slab waveguide problem had to be solved twice in the vertical and once in the horizontal direction; the definition of the directions is shown in figure 3.5. In the vertical direction, it was necessary to find the effective mode indices under the ridge $\bar{n}_{eff}$ using (3.7) and beside the ridge n_{eff} using (3.8). For this purpose, we had to solve equations (3.7) and (3.8) numerically. The results of this calculation were then used to define a new slab consisting of a core with thickness w and refractive index $\bar{n}_{eff}$ and two symmetric cladding layers with refractive index n_{eff}. The solution of this new slab waveguide was obtained using a similar equation like (3.7), but for TM waves. It gave then an approximate value for the effective refractive index in the propagating direction of the wave. This method usually gives good results for optical modes far away from cut-off and simple waveguide cross-sections.

Figure 3.6 shows the effective refractive index of the m = 0, 1, 2..., n-th mode as a function of the ridge width for 165 nm core thickness. We carried out this simulation using a ridge waveguide with zero residual clad thickness beside the ridge, as shown schematically in figure 3.5. The material of the waveguide core was $Al_{0.3}Ga_{0.7}As$ and that of the cladding layers was $Al_{0.8}Ga_{0.2}As$. As seen in figure 3.6, a ridge waveguide with increasing ridge width can support a successively increasing number of optical modes. For a 3 μm wide waveguide, we have a total of 5 allowed modes. In our case, however, the residual clad thickness of 100 nm prevented such an excessive number of supported modes; only up to three were seen in our waveguides, usually generated in the splitting region of Y-couplers.

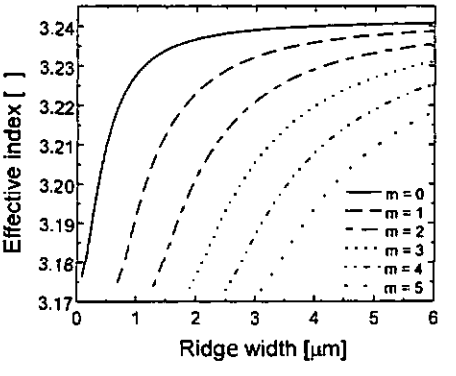

Fig. 3.6 - Effective indices of the different order modes as a function of the ridge width (core thickness = 165 nm)

3.1.2 Simulation of the ridge waveguide

Solving the fields in a ridge waveguide can also be done by finding a solution of the wave equation using a so-called shooting method. This type of algorithm starts with a guess of the eigenvalue of the Helmholtz-equation, implements the boundary conditions at one side, propagates across to the

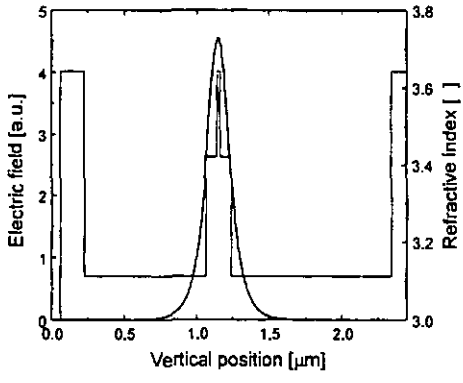

Fig. 3.7 - The solution of the horizontal slab waveguide problem under the ridge

other side using the wave-equation and tests how well the boundary condition at the far side has been fulfilled. Then the algorithm tries to minimize the error function of the calculation by using a new, better eigenvalue. Since the propagation of the mode is calculated in small segments only, the method can use a series development of the wave equation with only three or four terms. This makes the program very fast [33], [34]. Figure 3.7 shows simulated electric field and refractive index distribution as a function of vertical position of the one-dimensional slab waveguide structure as above. The core thickness was again 165 nm. Our experimental results showed, however, that this method appeared not to be sufficiently accurate for our applications. Experimentally tested, 3 µm wide, ridge waveguides with a 180 nm thick residual clad (in the same material system as in figure 2.2) were not monomode, in contrast to the prediction of the program.

A better agreement with our experimental data was achieved by using the so-called method of lines [35]. Here, the same wave equation as above, which simplifies into a Helmholtz-equation for the considered ridge problem, is solved by a semi-vectorial method instead of using the previously described shooting method. Through a one-dimensional discretization of this Helmholtz-equation, the computational effort can be reduced without affecting the accuracy of the results. In our case, the simulation with such a software [36] predicted a minimal residual clad thickness of 220 nm for a 3 µm wide and 165 nm thick monomode waveguide.

In figure 3.8, the simulation of different residual clad thicknesses for monomode behavior, depending on core thickness and ridge width, is presented. The general trend of these calculations was: a thinner core and a wider ridge require, for monomode behavior, a thicker residual clad above the core. We thus see that the finally chosen and fabricated design with 3 µm wide waveguides and a 100 nm thick

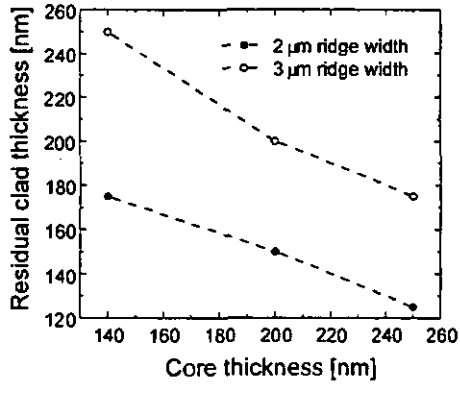

Fig. 3.8 - Minimal residual clad thickness for a monomode waveguide as a function of the core thickness and the ridge width

residual clad was not exactly the ideal one. But experiments showed that we had to consider also the radiation loss in the curved waveguides and, due to absorption loss in the waveguides, also the total interferometer length. These facts prevented the use of the design with a 220 nm thick residual clad which would have produced very weakly index-guided waveguides with an unacceptably large minimal curve radius of 10 mm.

3.2 LASERS

The software used for the simulation of lasers was basically the same as the one used for the ridge waveguides. The main difference was that we could simulate current injection and investigate the behavior of threshold current density and loop gain of two different modes as a function of the etch depth. An arbitrary facet reflectance and device length of the simulated Fabry-Pérot laser structure could be set in the structure file of the program [37].

For the simulation presented below, we assumed exactly the same layer structure and waveguide cross-section as in figure 2.2; the pumped section length was 500 µm and the facet reflectivity was 30 %. Figure 3.9 shows the dependence of the loop gain on the residual clad thickness for the first order mode and, in addition, the threshold current of such a laser structure. The loop gain of the zero order mode was set constant at unity, according to the threshold condition for that mode. If we increased the residual clad thickness (or decreased the etch depth), the gain of the first order mode decreased rapidly from 0.72 towards 0; and at a residual cladding thickness of 180 nm, the mode was no longer guided (cut-off condition for this mode). The threshold current of the structure increased from 6.5 to about 31 mA due to a larger current spreading in the thicker upper cladding layer. In good agreement with the simulation of the last section, we calculated here again a residual clad thickness of about 200 nm for monomode behavior. For the reasons mentioned in the previous section, this 200 nm thick residual upper clad was not realized in our devices; as a consequence, the waveguides were expected to be multimode. Experimental data showed, however, that the laser emitted monomode probably because of the higher total loss of higher order modes.

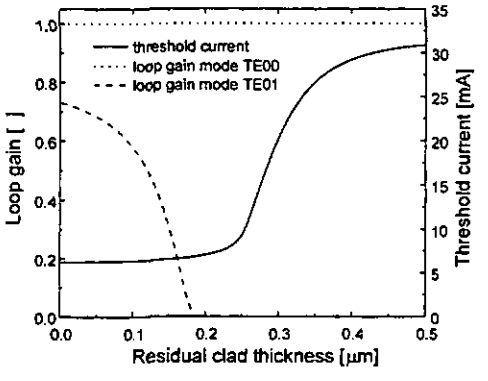

Fig. 3.9 - Calculated parameters of a Fabry-Pérot laser structure

3.3 GRATING

One of the most important parameters for the fabrication of a DBR laser is its grating period. This period determines at which wavelength the laser emission will take place. In order to fabricate a device with a low threshold current, it is necessary to achieve a perfect matching between the center of the material gain peak and the reflectivity peak of the Bragg reflector. The shape and the position of the Bragg peak can be calculated using [38], [39]

$$r(\lambda) = \frac{-i\kappa \cdot \sinh(SL)}{S \cdot \cosh(SL) + i\Delta\beta \cdot \sinh(SL)} \tag{3.9}$$

where

$$\Delta\beta \equiv 2\pi n_{eff}\left(\frac{1}{\lambda} - \frac{1}{\lambda_{Bragg}}\right) \tag{3.10}$$

and

$$S \equiv \sqrt{\kappa^2 - (\Delta\beta)^2} \tag{3.11}$$

In these formulae, κ is the coupling coefficient between the waveguide modes propagating in the forward and the backward-direction, L the length of the grating section, $r(\lambda)$ is the wavelength-dependent grating reflectivity, λ the wavelength, λ_{Bragg} the Bragg resonance wavelength and n_{eff} the effective refractive index of the structure.

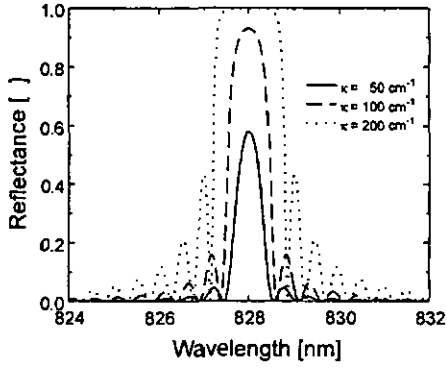

Fig. 3.10 - Calculated Bragg filter curves of a grating with 381 nm period and different values for κ.

Using these formulae and the waveguide design of figure 2.2, we calculated several grating reflection curves as shown in figure 3.10. The width of the central, so-called stopband, is defined as the distance between the two first points with zero reflectance. This width depends on the coupling coefficient and can therefore be used to determine the latter experimentally. The maximum reflectance changes with increasing κ, and reaches (for our grating length and period) 100 % for κ = 200 cm^{-1}. The filter curve which has been realized in our devices has a width of approximately 1 nm and its height indicates a maximal reflectance of 92 %. Of course, the maximal reflectance of the grating is also determined by

the length of the periodic corrugation. In this example, we assumed a length of 200 μm. The period of this grating was 381 nm and the resonance wavelength of the laser structure was set at 828 nm. The simulated depth of the grating lines (160 nm) and the 70 nm thin buffer layer between bottom of the grating and waveguide core resulted in a coupling coefficient of 100 cm^{-1}.

In practice, we usually started with the layer structure and the emission wavelength of Fabry-Pérot lasers fabricated in the material. We then had to determine the transmissivity of the grating and the wavelength filter action of the Bragg reflector. Considering the penetration depth of the light into the Bragg reflector, we can define its effective length, L_{eff}, through $2\kappa L_{eff} = \tanh(\kappa L)$, where L is the total length of the Bragg reflector. The transmissivity was given by the product κL_{eff}, while the filtering action was set by the number of grating periods. Thus, a long weak grating acts as a good wavelength filter, but it increases the threshold current of the device. On the other hand, a short strong grating is a poor wavelength filter, but due to the short penetration of the light and the therefore short unpumped section, a low threshold current can be expected. Grating transmissivity, threshold current density, and wavelength filtering were the input parameters for the simulation program, which gave the above grating period with the required etch depth and the thickness of the buffer layer as results.

3.4 COUPLERS

For the presented work, we invested some effort in the simulation of directional couplers. While the behavior of a 2x2-coupler is relatively straightforward, predicting the splitting ratio of a 3x3-coupler is more difficult. This was the main reason for concentrating on this latter element. Basis for these calculations were again the coupled mode equations [40].

Let us consider in an example the coupling between three neighboring fibers, which are arranged in an isosceles triangle configuration. The angle between the two equal sides should be at least 60 °, as shown schematically in figure 3.11. The arrangement of three ridge waveguides, as shown in the right half of figure 3.11, can be understood as a special case of the triangle configuration with an angle of 180 ° between the equal sides.

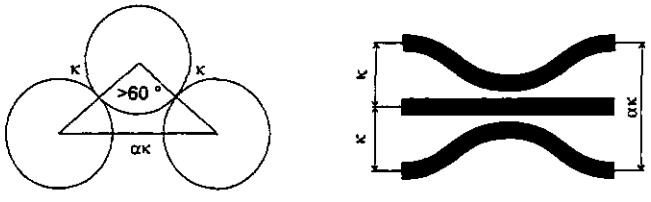

Fig. 3.11 - Arrangement of three fibers and three ridge waveguides into a 3x3-coupler structure

We thus have, in general, equally strong coupling κ between the central waveguide and the two outer ones, and weaker coupling $\alpha\kappa$ ($\alpha < 1$) between the outer waveguides. Setting the parameter α to any value between 0 and 1 allows the indirect determination of the geometric arrangement of the three fibers. The special case $\alpha = 1$ corresponds to the symmetric triangle configuration; for reasons of mathematical simplicity, we will assume this condition here. The relation

$$\frac{d}{dz}\begin{pmatrix} a_1 \\ a_2 \\ a_3 \end{pmatrix} = \begin{pmatrix} 0 & -i\kappa & -i\kappa \\ -i\kappa & 0 & -\alpha i\kappa \\ -i\kappa & -\alpha i\kappa & 0 \end{pmatrix} \cdot \begin{pmatrix} a_1 \\ a_2 \\ a_3 \end{pmatrix} \tag{3.12}$$

describes the amplitudes of the electric field, a_i, and their coupling behavior when propagating along the z-direction. The solution of this equation is explained in detail in the appendix, therefore we state here only the starting conditions and the solution. The starting conditions

$$\begin{pmatrix} a_1(0) \\ a_2(0) \\ a_3(0) \end{pmatrix} = \begin{pmatrix} A \\ 0 \\ 0 \end{pmatrix} \tag{3.13}$$

were chosen in a manner to have an input electric field amplitude A in the central waveguide (index 1), and initially no intensity in the two outer waveguides (indices 2 and 3).

We then obtained the following solution for one pass through the 3x3-coupler:

$$\begin{pmatrix} a_1(z) \\ a_2(z) \\ a_3(z) \end{pmatrix} = \begin{pmatrix} \frac{A}{3}\cdot e^{-2i\kappa z} + \frac{2A}{3}\cdot e^{i\kappa z} \\ \frac{A}{3}\cdot e^{-2i\kappa z} - \frac{A}{3}\cdot e^{i\kappa z} \\ \frac{A}{3}\cdot e^{-2i\kappa z} - \frac{A}{3}\cdot e^{i\kappa z} \end{pmatrix} \tag{3.14}$$

As shown in the right picture of figure 3.11, we fabricated a simplified double interferometer using such a 3x3-coupler. For the calculation of the three interference signals produced by this device, we had to solve the above system of differential equations twice: once for the first pass through the coupler and then, after being reflected at the chip facets and the external mirror, respectively, also for the second pass. The calculation of the interference signals produced by the interferometer structure mentioned above typically results in a picture like in figure 3.12. For this calculation, we assumed a strong coupling between the outer waveguides ($\alpha = 1$), the coupling coefficient κ was defined via $\kappa L = 0.45$, allowing the use of an

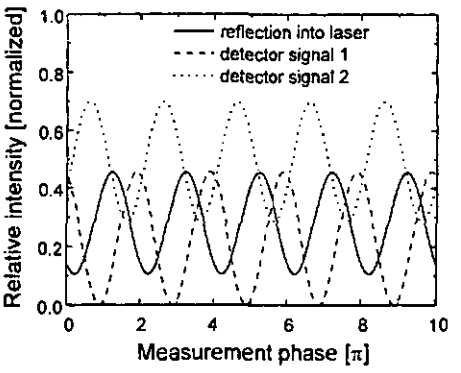

Fig. 3.12 - Calculated interference signals of a 3x3-coupler-based interferometer

arbitrary coupling length, and one of the outer waveguides was used as the sensing beam.

An interesting feature of this configuration was the inherent phase shift [41] between the three signals. Usually the phase shift between two independent signals of a double interferometer has to be adjusted with the help of phase shifters. By using a 3x3-coupler, the desired phase shift of 120 ° could be achieved in absence of any phase shifting component. Without using tedious mathematics, the mechanism of this inherent phase shift is not straight-forward to explain. But, obviously, the presence of an overnext-neighbor interaction ($\alpha > 0$) and the use of an outer waveguide as sensing beam are necessary requirements for producing this phase quadrature. In reality, however, we can of course not achieve equal strong coupling between the two outer waveguides and between neighboring waveguides. Assuming an $\alpha = 0.2$, a coupling strength of $\kappa L = 0.45$ and using one of the outer waveguides as sensing beam, an inherent phase shift of around 20 ° can be expected between the two interferometer signals. In a 3x3-coupler-based double interferometer, we therefore still need an active phase shifting component.

3.5 INTERFEROMETER

The signal generation in our monolithically integrated interferometer included one parasitic reflection in the sensing beam. This reflection was caused by the cleaved facet, which also served as mirror in the reference beam of our interferometer. In the sensing beam, however, the reflection at the same

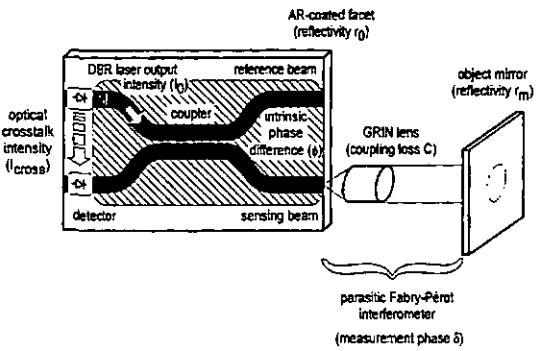

Fig. 3.13 - The single Michelson interferometer chip with external elements and simulated parameters

two interferometer arms, a one-pass coupling loss C at the external collimation lens, a constant offset signal I_{cross}, and the laser output intensity I_0 had to be considered in the simulation.

Figure 3.13 shows these quantities, which influenced the behavior of our interferometer. The constant offset is due to optical crosstalk between light emitter and photodetector. Considering the parasitic reflection at the AR-coated facet of the device, the very simple formula for dual beam interference turns in a rather complicated expression:

$$I(\delta) = I_{cross} + I_0 \left[r_0^2 + \frac{(r_0 - Cr)^2 + 4Cr_0 r \sin^2\left(\frac{\delta}{2}\right)}{(1 - Cr_0 r)^2 + 4Cr_0 r \sin^2\left(\frac{\delta}{2}\right)} + \ldots \right.$$
$$\left. + 2\frac{r_0^2(1 + r_0^2)\cos\phi - Cr_0 r\left(r_0^2 \cos(\delta + \phi) + \cos(\delta - \phi)\right)}{(1 - Cr_0 r)^2 + 4Cr_0 r \sin^2\left(\frac{\delta}{2}\right)} \right] \quad (3.15)$$

The following notation was used in this equation: $\delta = 4\pi dn/\lambda$ is the measurement phase, d the mirror distance, r the mirror reflectivity, r_0 the AR-coated facet reflectivity, n the refractive index of the surrounding medium, and λ the measurement wavelength. The calculations leading to equation (3.14) are explained in more detail in the appendix.

Figure 3.14 shows the calculated interference signals for four different external mirror reflectances. The intrinsic phase difference was set at ϕ = 3 rad, the measurement facet had a parasitic reflectance of 10 % (r_0 = 0.31); this resulted in an out-of-phase amplitude addition between the interference signals of the parasitic Fabry-Pérot interferometer generated by the cleaved facet and the external object mirror in the sensing beam, and of the regular Michelson interferometer. Furthermore, the interference signal of a Fabry-Pérot interferometer is cosine-shaped only for very small mirror reflectances. Larger reflectance of the mirrors, like in our case (r ≥ 30 %), results in a spike-like interferogram. These spikes do not result in a cosine-function when they are added to the interferogram of the regular Michelson interferometer. For phase differences of $\phi = \pi$ or ϕ

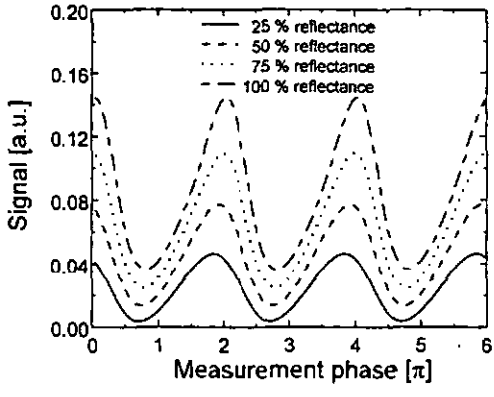

Fig. 3.14 - Calculated interference signals with 25, 50, 75 and 100 % external mirror reflectance

interferogram. These spikes do not result in a cosine-function when they are added to the interferogram of the regular Michelson interferometer. For phase differences of $\phi = \pi$ or $\phi = 0$, the total interference signal was not obviously distorted because of the in- or anti-phase addition of the two single interference curves. But all intermediate phase values caused an asymmetrically skewed shape of the total interference signal.

As we will see in section 6.5, the resolution of a displacement measurement suffers when using distorted instead of ideally sinusoidal signals. This is due to the non-ideal shape of the Lissajous-figure, which can be obtained by plotting the two interference signals as a function of each other. If this plot is a circle, a phase interpolation of 1 ° can be achieved; but the interpolation resolution decreases soon to less than 20 ° when using an ellipse or egg-shaped Lissajous-figure. A suppression of the parasitic reflection at the cleaved facet would therefore be helpful for high-resolution displacement measurements.

[32] H.P. Zappe, *"Introduction to semiconductor integrated optics"*, Artech House, Boston, 1995

[33] D.F.G. Gallagher, Program "WGScan" by *Photon Design*, Optoelectronic Consultancy, Oxford, England, 1994

[34] D.F.G. Gallagher, "Series solutions to the arbitrary profile 1-dimensional waveguide and quantum well problems", *IEEE J. Quantum Electron.*, vol. QE-28, no. 8, pp. 1785 - 1791, 1992

[35] U. Rogge and R. Pregla, "Method of lines for the analysis of stripe-loaded optical waveguides", *J. Opt. Soc. Am. B*, vol. 8, no. 2, pp. 459 - 463, 1991

[36] J.-S. Gu, P.-A. Besse and H. Melchior, "Method of lines for the analysis of the propagation characteristics of curved optical rib waveguides", *IEEE J. Quantum Electron.*, vol. QE-27, no. 3. pp. 531 - 537, 1991

[37] D.F.G. Gallagher, Program "Ridge" by *Photon Design*, Optoelectronic Consultancy, Oxford, England, 1994

[38] W. Streifer, D.R. Scifres, and R.D. Burnham, "Coupled wave analysis of DFB and DBR lasers", *J. Quantum Electron.*, vol. QE-13. no. 1, pp. 134 - 141, 1977

[39] D.F.G. Gallagher, Program "DBRcoef" by *Photon Design*, Optoelectronic Consultancy, Oxford, England, 1993

[40] A. Yariv, *"Optical Electronics"*, Saunders College Publishing, 4th edition, pp. 519 - 529, 1991

[41] R. Fuest, "Integrated optical Michelson-interferometer with quadrature phase modulation in glass for displacement measuring", reprint from *tm - Technisches Messen*, vol. 58, no. 4, pp. 152 - 157, 1991

4. VACANCY-ENHANCED DISORDERING

In this chapter, we will discuss how the selective partial intermixing of a single QW structure can be obtained. This process is used to reduce the absorption loss of the waveguides in our integrated circuit; the pumped laser sections remain in their as-grown state. Furthermore, a comparison of the most appropriate further bandgap engineering methods will be given.

4.1 PRINCIPLE AND COMPARISON TO OTHER METHODS

As discussed in section 2.3, the definition of transparent and absorbing areas on one and the same substrate is of fundamental importance for semiconductor integrated optics. There are several approaches to generate a III-V-semiconductor-based chip with transparent and absorbing areas. The most popular among them are selective area growth (SAG), growth on a nonplanar, patterned substrate, partial waveguide etch with subsequent regrowth, the combination of III-V-semiconductor-based and dielectric waveguides, evanescent- or taper-coupling of two in the vertical direction sandwiched waveguides, and, finally, the selective partial intermixing of the QW using vacancies or impurities.

4.1.1 *Growth methods*

SAG is a growth technique using SiO_2 stripe masks with windows between them. Between these stripes, the crystal growth rate decreases with increasing window width or increases with increasing mask width. This allows the *simultaneous* epitaxy of quantum well structures with different thicknesses, and therefore the growth of structures with different bandgap energies. Several groups have reported on photonic integrated circuits using SAG [42], [43], and have achieved good device behavior. Especially popular was the integration of a distributed feedback (DFB) laser with waveguides; output powers and quantum efficiencies exceeding 10 mW and 20 %, respectively, were reported. The coupling efficiency between laser and waveguide was 50 %.

In contrast to SAG, the growth on a nonplanar, patterned substrate allows the *subsequent* epitaxy of a passive waveguide and an active layer of, for example, a DFB laser. The light of the latter is then butt coupled into the passive waveguide. With this method, coupling efficiencies of 60 - 75 % were reported [44], [45]. The output at the waveguide facet of the device was up to 2 mW and limited only by the waveguide loss of more than 20 dB. By using this method, the fabrication of a photonic integrated circuit, consisting of laser passive waveguide and intensity modulator, could be realized [46].

The combination of a ridge waveguide laser with an oxide waveguide requires a high-quality mirror dry etch technique [47]. In this device, most

loss (estimated value 1.1 dB) was created at the interface between the etched laser mirror and the SiO_2-waveguide. Nevertheless, nearly balanced output power of 27 and 30 mW was seen from the glass waveguide and the cleaved facet output of the laser. The glass waveguide supported, due to its large dimensions (4 x 100 μm^2 cross-section), various optical modes, and is therefore not suitable for interferometric circuits.

Recently, a passive Mach-Zehnder-interferometer with both a III-V-based and a dielectric ridge waveguide was demonstrated in our laboratory. Refilling of etched holes in the nonplanar substrate with SiO_2/TiO_2-layers was performed before waveguide etching. The coupling loss at the interface III-V-semiconductor/dielectrics is considerably larger here than in the previous approach, but, on the other hand, the ridge waveguides used in this work are singlemode which is necessary for interferometric applications.

The approach using a tapered waveguide for the coupling of the laser light into the lower output waveguide requires relatively complicated processes for taper fabrication and an additional regrowth. With this coupling scheme, usually 10 - 15 % coupling efficiency and up to 10 mW output power can be achieved [48], [49].

4.1.2 Methods based on QW intermixing

The second class of methods to define different bandgaps on a QW substrate is selective, partial QW intermixing. We can distinguish between impurity-induced disordering (IID), using, for example, Si or protons [50], [51], [52], and vacancy-enhanced disordering (VED) [53], [54]. VED uses the property of group-III-vacancies to diffuse at elevated temperatures from the wafer surface towards the waveguide core and to promote there a disordering of the QW. Both IID and VED need a high temperature thermal annealing step at about 800 to 1000 °C. As a drawback, this annealing step can change the doping profile of the p-n-junction and also the optical properties of the crystal. We decided to use VED for our integrated circuits, because it required only the evaporation of two different surface dielectric layers and the use of a rapid thermal annealing (RTA) oven; this appeared to be realizable in a more straight-forward manner than the adoption of a SAG process. In the following, we will concentrate on the mechanisms and process details of the VED.

4.2 MECHANISM AND PROCESS

4.2.1 VED mechanism

Basis for the VED process is the generation of group III-vacancies using two different dielectric cap layers and an RTA step. Under an SrF_2-layer, only few vacancies are produced during RTA, while the SiO_2-layer creates many vacancies by out-diffusion of Ga from the GaAs cap into the SiO_2. During 40 s

RTA at 960 °C, these vacancies diffuse through the upper cladding into the QW region and promote an intermixing between Al of the adjacent core material ($Al_{0.3}Ga_{0.7}As$) and Ga of the initially pure GaAs QW. This process increases the Al-content of the QW material and therefore its bandgap energy; a larger bandgap energy corresponds to a blue-shifted PL spectrum, and a blue-shifted absorption edge. Since only few vacancies are produced under the SrF_2-layer, only little intermixing takes place.

4.2.2 Process details

VED required only a few and unsophisticated additional processing steps. The process started with the e-beam evaporation of a 200 nm thick SiO_2-layer. This evaporation was performed in a standard e-beam evaporation machine (Balzers BAK 550). The base pressure was $p_0 = 2x10^{-6}$ Torr, the deposition rate 3 Å/s and the pressure during evaporation around $p_{evap} = 5x10^{-5}$ Torr. The samples were mounted on a planetary drive; this resulted in a very homogeneous layer deposition and thickness. The final thickness of the SiO_2-layer could be determined by measuring the eigenfrequency change of an oscillating quartz crystal.

After deposition, the SiO_2-layer was patterned by standard photolithography and reactive ion etching (RIE). For RIE, we used 50 sccm of CF_4 at a pressure of 50 mTorr and an rf power of 100 W. The reverse voltage for these process parameters was -330 V. It was important to prevent over-etch in order not to damage the future contact region of the lasers. Without stripping the photoresist mask, we then thermally evaporated 300 nm SrF_2 (deposition rate 5 Å/s) from a tungsten crucible. The evaporation procedure started at a base pressure of $p_0 = 5x10^{-6}$ Torr; the deposition rate of 5 Å/s had to be controlled manually by adjusting the current density through the crucible. The pressure during deposition was $p_{evap} = 1x10^{-4}$ Torr. Due to the high melting point of SrF_2 (1450 °C at 1 bar, vapor pressure $1x10^{-4}$ Torr at 1000 °C [55]) and in order to achieve a homogeneous layer deposition, we had to use a baffled crucible; its labyrinth guaranteed the evaporation of the molten material and prevented direct sublimation of the powder. The final thickness of the SrF_2-layer was measured by the same method as above.

The SrF_2-layer was patterned in a self-aligned lift-off process by simply removing it from the photoresist on the lower SiO_2. Best results were achieved when using Microposit 1165 remover in combination with weak ultrasound. Since SrF_2 is a very brittle material, this lift-off technique worked very well even without special attention paid to an undercut mask profile. The result of this procedure was a nearly planar structure completely covered either with SrF_2 or SiO_2. Selective intermixing of the QW was accomplished by high temperature RTA (960 °C, 40 s). The samples used a proximity GaAs wafer to prevent surface damage by arsenic out-diffusion. After RTA, we removed the SiO_2 by the same RIE process as above and the SrF_2 by a subsequent dip in diluted HCl (HCl/H_2O 1 : 9, 10 s).

The method using a proximity wafer was performed in favor of the annealing under an actively generated arsenic overpressure; in earlier publications, this overpressure was usually generated by sealing the samples under an arsenic-rich atmosphere into a quartz ampoule. During the subsequent RTA, no surface damage was created. In our first experiments, the wafer surface after removal of the SrF_2-layer exhibited many round defects. Their average diameter was 5 µm and the distance between them around 20 µm; a typical depth of 2 µm was seen. Of course, this high defect density allowed no ridge waveguide-based device fabrication. Experience showed that it was important to keep the deposition rate of the dielectric layer low; this guaranteed a homogeneous growth of the layer. As opposed to other workers in this field, we evaporated our layers without the recommended powder mixture of SrF_2/AlF_3 [56], [57], [58]. About 8 % aluminum-fluoride was reported to be helpful for the deposition of layers with a small grain size [59], but in our experiments, the addition of AlF_3 resulted in a more difficult evaporation procedure and in a highly un-removable dielectric film.

4.3 PHOTOLUMINESCENCE RESULTS

The characterization of intermixed and non-intermixed QWs was performed using photoluminescence (PL) measurements. Our experimental setup consisted of an argon ion laser (λ = 488 nm, P = 10 mW) for the excitation, a grating spectrometer with 0.32 m focal distance, and a GaAs photodetector. All measurements were carried out at room temperature. Slit width of the spectrometer was 200 µm, and the grating had 1200 lines/mm.

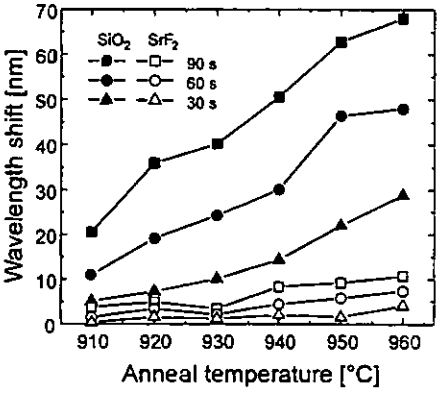

Fig. 4.1 - Photoluminescence wavelength shifts for different annealing conditions

Figure 4.1 summarizes the results of these PL measurements; all samples were cleaved from the same wafer, of which one half was coated with SiO_2, and the other with SrF_2. The layer structure was identical to that presented in figure 2.2. RTA at temperatures between 910 °C and 960 °C and for 30, 60 and 90 s duration was carried out. Under the SrF_2-layer, the blue-

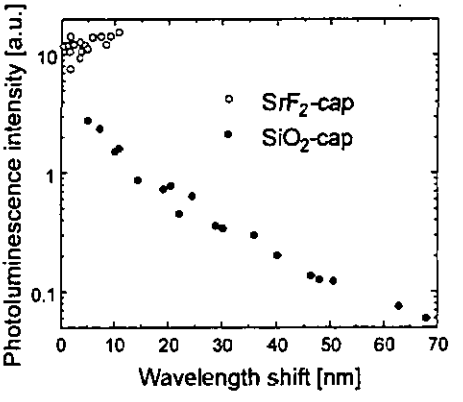

Fig. 4.2 - Photoluminescence intensity as a function of wavelength shift

shifts of the PL peak wavelength remained smaller than 11 nm, while under the SiO_2-layer, up to 68 nm wavelength shift was seen.

Figure 4.2 shows that the PL intensity decreased continually by two orders of magnitude when increasing the blue-shift of the PL spectrum from 5 to 68 nm. As we will see in the next section, this was not detrimental to device fabrication, because only passive optical components such as waveguides or couplers were fabricated in the intermixed QW areas.

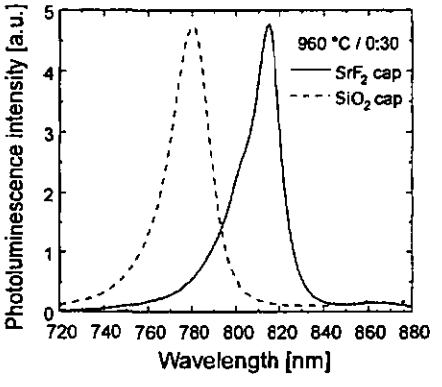

Fig. 4.3 - Shifted and unshifted PL spectrum after an RTA of 960 °C and 30 s

Figure 4.3 shows an as-grown and a blue-shifted PL spectrum. The peak wavelength of the intermixed PL spectrum is blue-shifted by 35 nm ; this corresponds to a bandgap increase of 68 meV. Using bandgap differences of that order of magnitude reduced the waveguide loss due to band-edge absorption considerably. When fabricating waveguides from unshifted and from shifted material, we could see a decrease in loss from 60 to around 30 dB/cm. Finally, we measured the transition between the shifted and the unshifted region by high-resolution PL and found a complete change of the bandgap energy within a distance of less than 30 μm and 60 % of the total change within 5 μm distance.

4.4 MULTIPLE WAVELENGTH FABRY-PEROT LASERS

In order to demonstrate the utility of the VED process for selective QW intermixing without degradation of the p-n-junction, we fabricated monolithically integrated Fabry-Pérot lasers with two different emission wavelengths [60]. The process started with the same layer structure as above and employed dry etching of 4 μm wide ridge waveguides. 250 nm Si_3N_4 served as passivation and electrical isolation layer on the sidewalls of the ridges. The length of the cleaved lasers was 500 μm, and the different laser types were separated by 250 μm. For comparison purposes, we fabricated lasers with exactly the same design from as-grown material.

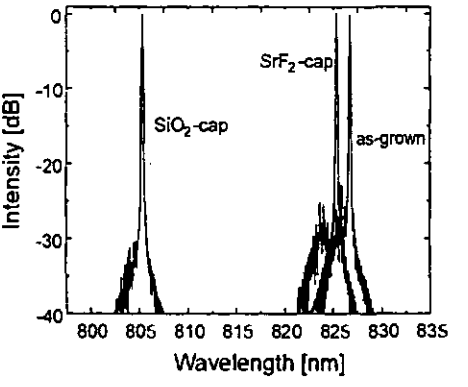

Fig. 4.4 - Optical spectra of SiO_2-capped, SrF_2-capped and as-grown material Fabry-Pérot lasers

Figure 4.4 shows the optical emission spectra of the three laser types. The peak wavelengths of the annealed lasers were 825 nm (SrF_2-capped) and 805 nm (SiO_2-capped); as-grown material lasers emitted at 827 nm. The devices showed comparable threshold current densities (as-grown: 600 A/cm², SiO_2-capped: 500 A/cm², SrF_2-capped: 700 A/cm²) and slope efficiencies (as-grown: 0.52 W/A, SiO_2-capped: 0.42 W/A, SrF_2-capped: 0.36 W/A). The threshold voltages, defined by $V_{th} = V(I_{th})$, showed a considerably increased series resistance of the SrF_2-capped devices (as-grown: 2.1 V, SiO_2-capped: 2.15 V, SrF_2-capped: 3.3 V). This was understood partly as a CF_4-RIE-induced damage of the contact region [61], but also through a slightly misplaced p-n-junction due to dopant migration during RTA.

In later processing runs, we changed the order of the removal steps for SiO_2 and SrF_2; this allowed protection of the laser contact region from RIE plasma damage by the still existent SrF_2-layer. Replacing SiO_2 plasma removal by a chemical wet etch step using HF is not recommended because of small holes in the GaAs cap layer caused by RTA. Starting at these holes, an undesired cladding etch by HF is possible. Since the holes in the cap appear only after RTA, the *patterning* of the SiO_2-layer should be possible by wet etching. This would reduce the number of plasma exposures from three to one; the only remaining plasma process would then be the contact hole etch on top of the ridges.

[42] D. Trommer, "Photonic integration on InP", *Proc. ECIO'95 (Delft, The Netherlands)*, pp. 93 - 98, 1995

[43] R.M. Lammert, T.M. Cockerill, D.V. Forbes, and J.J. Coleman, "Dual-channel strained-layer InGaAs/GaAs/AlGaAs WDM source with integrated coupler by selective-area MOCVD", *IEEE Photonics. Technol. Lett.*, vol. 6, no. 10, pp. 1167 - 1169, 1994

[44] D. Remiens, B. Rose, M. Carre, and V. Hornung, "GaInAsP/InP integrated ridge laser with a butt-joined transparent optical waveguide fabricated by single-step metalorganic vapor-phase epitaxy", *J. Appl. Phys.*, vol. 68, no. 5, pp. 2450 - 2453, 1990

[45] V. Hornung, D. Remiens, D. Robein, A. Gloukhian, and M Carre, "Simple approach for monolithic integration of DFB laser and passive waveguide", *Electron. Lett.*, vol. 27, no. 18, pp. 1683 - 1685

[46] L.R. Brovelli, R. Germann, J.P. Reithmaier, H. Jäckel, H.P. Meier, and H. Melchior, "Transform-limited picosecond optical pulses from a mode-locked InGaAs/AlGaAs QW laser with integrated passive waveguide cavity and QW modulator", *IEEE Photonics Technol. Lett.*, vol. 5, no. 8, pp. 896 - 899, 1993

[47] M.C. Wu and Y.J. Chen, "GaAs/AlGaAs quantum well lase with monolithically integrated extended glass waveguide cavity", *Electron. Lett.*, vol. 27, no. 21, pp. 1954 - 1956, 1991

[48] T.L. Koch, U. Koren, G. Eisenstein, M.G. Young, M. Oron, C.R. Giles, and B.I. Miller, "Tapered waveguide InGaAs/InGaAsP multiple-quantum-well lasers", *IEEE Photonics Technol. Lett.*, vol. 2, no. 2, pp. 88 - 90, 1990

[49] M. Chien, U. Koren, T.L. Koch, B.J. Miller, M. Oron, M.G. Young, and J.L. Demiguel, "Short-cavity distributed Bragg reflector laser with an integrated tapered output waveguide", *IEEE Photonics Technol. Lett.*, vol. 3, no. 5, pp. 418 - 420, 1991

[50] R.L. Thornton, R.D. Burnham, T.L. Paoli, N. Holonyak, Jr., and D.G. Deppe, "Low threshold planar heterostructure lasers fabricated by impurity-induced disordering", *Appl. Phys. Lett.*, vol. 47, no. 12, pp. 1239 - 1241, 1985

[51] T. Hirata, M. Maeda, and H. Hosomatsu, "A novel GRIN-SCH-SQW laser diode monolithically integrated with low-loss passive waveguides", *Jpn. J. Appl. Phys.*, vol. 28, no. 8, pp. 1429 - 1432, 1989

[52] T. Hirata, M. Maeda, M. Suehiro, and H. Hosomatsu, "Fabrication and characteristics of GaAs-AlGaAs tunable laser diodes with DBR and phase-control sections integrated by compositional disordering of a quantum well", *IEEE J. Quantum Electron.*, vol. QE-27, no. 6, pp. 1609 - 1615, 1991

[53] L.J. Guido, N. Holonyak, Jr., K.C. Hsieh, R.W. Kaliski, R.D. Burnham, R.L. Thornton, J.E. Epler, and T.L. Paoli, "Effects of dielectric encapsulation and As overpressure on Al-Ga interdiffusion in $Al_xGa_{1-x}As$ quantum-well heterostructures", *J. Appl. Phys.*, vol. 61, no. 4, pp. 1372 - 1379, 1987

[54] I. Gontijo, Y. Krauss, J.H. Marsh, and R.M. de la Rue, "Postgrowth control of GaAs/AlGaAs quantum well shapes by impurity-free vacancy diffusion", *IEEE J. Quantum Electron.*, vol. QE-30, no. 5, pp. 1189 - 1195, 1994

[55] Balzers AG, "Aufdampf- und Zerstäubungsmaterialien, Verdampfungs-quellen", *Product overview evaporation materials*, pp. 12 - 24, 1989, (in German)

[56] J. Beauvais, J.H. Marsh, A.H. Kean, A.C. Bryce, and C. Button, "Suppression of bandgap shifts in GaAs/AlGaAs quantum wells using strontium fluoride caps", *Electron. Lett.*, vol. 28, no. 17, pp. 1670 - 1672, 1992

[57] J.H. Marsh, S.I. Hansen, A.C. Bryce, and R.M. de la Rue, "Applications of neutral impurity disordering in fabricating low-loss optical waveguides and integrated waveguide devices", *Opt. & Quantum Electron.*, vol. 23, pp. S941 - S957, 1991

[58] S.G. Ayling, A.C. Bryce, I. Gontijo, J.H. Marsh, and J.S. Roberts, "A comparison of carbon and zinc doping in GaAs/AlGaAs lasers bandgap-tuned by impurity-free vacancy disordering", *Semicond. Sci. Technol.*, vol. 9, pp. 2149 - 2151, 1994

[59] A. Scherer, B.P. van der Gaag, E.D. Beebe, and P.S.D. Lin, "Fluoride etch masks for high-resolution pattern transfer", *J. Vac. Sci. Technol. B*, vol. 8, no. 1, pp. 28 - 32, 1990

[60] D. Hofstetter, H.P. Zappe, J.E. Epler, and P. Riel, "Multiple wavelength Fabry-Pérot lasers fabricated by vacancy-enhanced quantum well disordering", *Appl. Phys. Lett.*, vol. 67, no. 14, pp. 1978 -1980, 1995

[61] S.W. Pang, "Radiation damage in dry etching", *Microelectronic Eng.*, vol. 5, pp. 351 - 361, 1986

5. DBR LASERS

In the following chapter, a description of the fabrication and characterization of our single-growth-step DBR lasers will be given. In the last section of the chapter, we will present a prototype of an integrated optical circuit. This device consists of a DBR laser with a transparent waveguide and a monitoring photodetector, and its fabrication procedure was a combination of the VED and the DBR laser process.

5.1 PRINCIPLE OF OPERATION AND FEATURES

The main difference between a III-V-based Fabry-Pérot (FP) laser and a DBR laser is the type of mirrors employed. While in a FP laser both mirrors are cleaved facets, the DBR laser uses at least one wavelength-selective, unpumped Bragg mirror. The length of this DBR section allows it to be used not only as a laser mirror, but also as an optical connection, of variable transmissivity, between laser and photonic integrated circuit (PIC). This function is very important because of the high feedback sensitivity of semiconductor lasers. The choice of a DBR laser as light source in a PIC is therefore no accident, since the Bragg reflector acts simultaneously as laser mirror, wavelength filter, and also as optical connection between laser cavity and PIC.

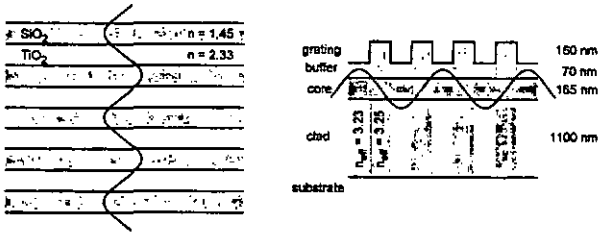

Fig. 5.1 - Analogy between a dielectric λ/4 layer stack and a 1st order Bragg mirror (cross-section).

The working principle of such a Bragg grating mirror can be easily explained if we realize the analogy between dielectric mirrors and Bragg mirrors. Both of them use stacks of $\lambda/4$ layers with two different refractive indices, as shown schematically in the cross-sections of figure 5.1. As opposed to dielectric mirrors, which may use twenty pairs of SiO_2/TiO_2-layers with a large difference of the refractive indices (SiO_2: 1.45 and TiO_2: 2.33), we have to deal with very small differences of the effective refractive index in a Bragg mirror. Typical effective index values for 230 nm and 70 nm residual clad thickness, which correspond to the thicknesses on the top and the bottom of the grating lines, are n_{eff} = 3.25 and n_{eff} = 3.23. This small index difference requires many more $\lambda/4$ layers or grating periods to achieve a certain reflectivity.

As drawn on the right half of figure 5.1, these $\lambda/4$ layers are, in the case of a first order grating, 65 nm long waveguide sections, which are defined by the surface corrugation of the grating. A typical value of 500 grating periods can be proposed to achieve a mirror reflectance of around 90 %. Since the grating period of such a first order grating is only 130 nm, for edge emitting lasers usually a third order grating will be fabricated (Λ = 390 nm). Gratings with this period may be defined much easier than first order gratings by holographic means (see section 5.2). The simulation of the grating period has already been discussed in section 3.3.

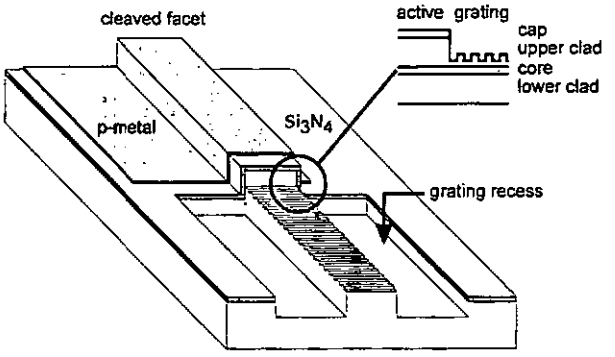

Fig. 5.2 - Schematic picture of a single-growth-step DBR laser with a holographically-defined, recessed grating

Figure 5.2 shows the two-section-DBR laser used for this work; the device consisted of a pumped laser section and an unpumped Bragg mirror section. These features allowed a rather simple fabrication procedure without epitaxial regrowth and, thanks the use of a so-called grating recess, without a deep grating etch [62]. The grating recess is a lowered part of the waveguide cladding in the grating section; its depth defined a residual clad thickness of 230 nm. The subsequent grating etch was shallow (d = 160 nm) and therefore relatively easy to control. Varying the thickness of the buffer layer between bottom of the grating and waveguide core allowed customization of the coupling coefficient.

On the other hand, this type of grating mirror can produce, especially with even thinner buffer layers, a very strong coupling coefficient (up to κ = 400 cm^{-1}) compared to epitaxially overgrown structures. This is because of the large index step between $Al_{0.3}Ga_{0.7}As$ and air. In previously published DBR laser work, typical coupling coefficients of κ < 100 cm^{-1} were reported [63], [64].

The short penetration depth of the light into a grating with a strong coupling coefficient (L_{eff} < 100 µm) reduces the threshold current density of

the device mainly because of reduced absorption loss in the unpumped grating section. The linewidth, however, can be reduced by using a longer, weaker grating; for more periods make the Bragg reflection curve (figure 3.10) narrower and allow a better wavelength filtering. The presently fabricated lasers have effective grating lengths of 200 μm and a reflectance of 90 %. This results in twice the threshold current density of FP lasers with equal pumped length.

There was one more reason to use DBR lasers in our interferometric circuits: the temperature tuning can be modehop-free over a temperature range of 10 K, while the FP lasers have modehops every 3 - 5 K. These modehops can change their position on the temperature-scale during aging of the laser, a property which makes FP lasers not very attractive for wavelength stabilization.

5.2 GRATING FABRICATION

The holographic definition of gratings for DBR lasers has a long tradition. Although the first DBR laser devices operated with photolithographically-exposed gratings [65], [66], the first holographically-defined grating for a GaAs/AlGaAs DBR laser was developed soon thereafter [67]. The setup for our holographic exposure consisted of a HeCd-laser (λ = 441.6 nm, P = 100 mW), whose light was split into two orthogonal beams of

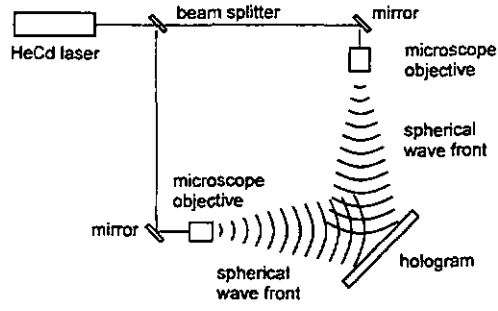

Fig. 5.3 - Schematic picture of the holographic setup used for grating exposure

equal intensity. As shown in figure 5.3, these two laser beams were then converted into spherical waves by focusing them with microscope objectives (magnification 40x, NA = 0.65) onto 5 μm pinholes. The latter served as spatial filters and acted as point-like light sources. The required angle Θ_{Bragg} between the interfering laser beams was determined by the desired grating period according to

$$\Lambda = \frac{\lambda}{2n_0 \sin \Theta_{Bragg}} \tag{5.1}$$

Here Λ is the grating period, n_0 the refractive index of the atmosphere, λ the laser wavelength, and Θ_{Bragg} the Bragg angle. A larger exposure distance (distance between pinhole and sample) resulted in a longer grating period. Due to the interference between two laser beams with spherical wavefronts, the generated interference pattern did not produce straight grating lines but rather hyperbolae, even at an exposure distance of 65 cm. A further undesired property of holographic grating exposure using spherical wavefronts was the chirp of the grating period. With our setup, we minimized the chirp to within $\Delta\Lambda = 0.5$ nm by using a rather large exposure distance (in an area of 2x2 cm^2). After a measurement of the grating period, the latter could be corrected to a certain amount by moving the sample holder.

For the fabrication of DBR gratings, we started with dry etching of the grating recess to a depth of 230 nm above the core. This process was a magnetic field enhanced reactive ion etch (MERIE) using 2 sccm $SiCl_4$, 200 W rf power, -110 V dc bias, and 0.2 mTorr pressure. Then we spun a thin photoresist layer (diluted Shipley S1805/EC solvent 1:1) on the sample; the preferred thickness on top of the recessed waveguide was one half of the grating period, hence 200 nm. After holographic exposure (5 min), we developed the grating mask for 30 s (Shipley developer/H_2O 1:1). In order to protect the top of the grating profile from the subsequent O_2-RIE, we evaporated 4 nm Cr under an angle of 13 ° to the substrate plane on to both sides of the grating profile. A 10 min anisotropic O_2-plasma etch (80 W, 5 mTorr) resulted in a clean grating mask. The transfer of this photoresist grating into the semiconductor material was performed again by MERIE (6 sccm, 200 W, -110 V, 1 mTorr) and produced a rectangular-shaped grating. Finally, we removed the photoresist mask through a 30 min O_2 plasma ash.

In the course of this work, we used no etch stop layers to define recess depth or grating depth. For a more accurate determination of these depths, it would be very advantageous to run the process with a selective dry or wet etch process. In the GaAs/AlGaAs material system, the use of GaInP etch stop layers appears to be one of the most promising approaches.

5.3 DEVICE BEHAVIOR

5.3.1 *Electrical and spectral properties*

Except for the preliminary aging tests, all characterization was performed on devices in bar form. We contacted the devices with probe needles which were mounted in probers (The Micromanipulator Co.). The characterization setup consisted of a Peltier temperature-stabilized Al-mount (Temperature controller ILX LDT-5910B), an optical multimeter (ILX OMM-6810) with a combined wavelength-power-measurement head, and an HP 4155A semiconductor parameter analyzer. For near-field measurements, we

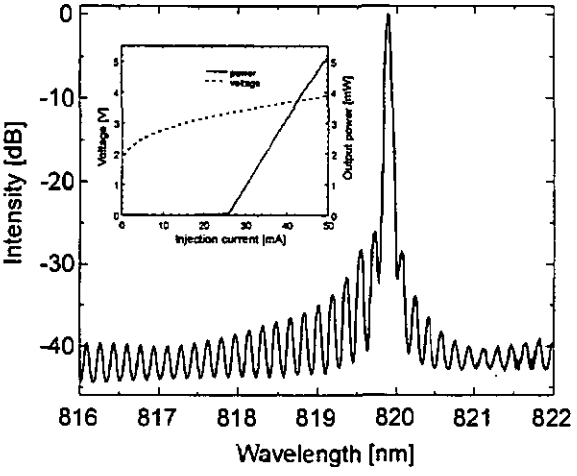

Fig. 5.4 - Optical spectrum of a DBR laser driven at 2.3 x I_{th}. The inset shows the I-V- and the P-I-curve.

used a microscope objective (magnification 40x) and a CCD camera (SONY CCB-M25/CE) with pixel clock. The latter allowed the pixel by pixel read out of the intensity information by a frame grabber system. For testing the material quality, we usually fabricated broad area laser devices (see appendix). These were driven pulsed at room temperature with a pulsed current source (Precision pulsed current source ILX LDP-3811). Preliminary spectral measurements were carried out using a fiber-coupled grating spectrometer (ANDO AQ-6312B); the spectrum of figure 5.4, however, was measured with a high-resolution grating spectrometer (JOBIN-YVON 640, 0.64 m focal distance, 600 lines/mm, 0.025 nm resolution).

We initially fabricated DBR lasers of various designs with pumped section lengths of 480, 730 and 880 µm, DBR section lengths of 1000, 500 and 200 µm, and ridge widths of 3 and 5 µm. As shown in the inset of figure 5.4, our DBR lasers had a maximal output power of 5 mW; the required injection current to achieve this power was 50 mA. A typical threshold current of

25 mA was seen for 500 μm long and 3 μm wide devices; this corresponds to a threshold current density of 1.6 kA/cm^2.

The temperature dependence of the threshold current can be described by

$$I_{th}(T) = I_0 \cdot e^{T/T_0} \tag{5.2}$$

This T-dependence was rather strong; we observed a $T_0 = 100$ K. The threshold voltage, defined by $V_{th} = V(J_{th})$, was $V_{th} = 3.3$ V, caused by a relatively high series contact resistance of the device. FP lasers with the same pumped section length had typical threshold currents of 12 mA, a threshold current density of 0.8 kA/cm^2, and a $T_0 = 220$ K. The optical spectrum (figure 5.3) shows a main peak at 820 nm with a sidemode suppression ratio of 27 dB. The longitudinal mode separation of 0.173 nm results in an effective grating length of around 80 μm, this can be calculated by using

$$\Delta\lambda_{Fabry-Perot} = \frac{\lambda^2}{2n_{eff}(L + L_{eff})} \tag{5.3}$$

A measurement of the stopband-width, $\Delta\lambda_{Bragg}$, from the subthreshold spectrum allowed determination of the coupling coefficient of the grating. The equation used for this calculation was [68]

$$\Delta\lambda_{Bragg} = \frac{\kappa\lambda^2}{\pi n_{eff}} \tag{5.4}$$

For the device data presented in figure 5.3, we estimated a value of κ = 350 cm^{-1}, in agreement with the simulated value of κ = 390 cm^{-1}, when using no buffer layer between bottom of the grating and core. In a later stage of this work, we inserted a 70 nm buffer; this measure reduced the coupling coefficient to about κ = 100 cm^{-1}.

The linewidth of these DBR lasers was determined by a scanning FP spectrum analyzer; the result of such a measurement was equipment-limited, $\Delta\nu < 20$ MHz. A more accurate measurement using a self-heterodyne technique resulted in a linewidth of $\Delta\nu = 500$ kHz. The far-field was measured with a pivot-mounted silicon-photodetector and showed a 13 x 40 ° angular distribution (FWHM) for the horizontal and vertical directions, respectively. These values agree well with those reported in the literature for devices with similar ridge dimensions [69], [70].

5.3.2 *Temperature tuning*

As mentioned already in section 5.2, one of the most important features with respect to wavelength stabilization of a DBR laser is its temperature tuning behavior. Because of the wide modehop-free tuning range of DBR lasers, they are very suitable for frequency or wavelength stabilization. DBR lasers tune with temperature almost exclusively due to the temperature-induced change of the material refractive index. On the other hand, the temperature tuning of a FP laser is mainly governed by the temperature-controlled change of the material gain peak. This explains the large difference of the T-tuning coefficients, $d\lambda/dT$, of these two laser types. In figure 5.5, we measured $d\lambda/dT = 0.078$ nm/K for the DBR devices, while for the FP lasers, a $d\lambda/dT = 0.26$ nm/K was seen. The T-tuning of DBR lasers showed no large modehops over 20 K; the FP lasers fabricated from the same substrate showed mode-hopping ($\Delta\lambda \approx 1$ nm) every 3 - 5 K. At room temperature (T = 298 K), there was an emission wavelength difference between DBR and FP lasers of 3 nm. This discrepancy was caused by a small (≈ 1 nm) mismatch between simulated and actual grating period.

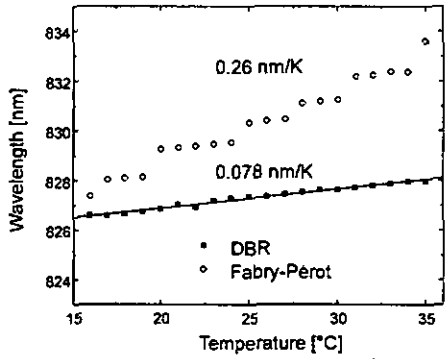

Fig. 5.5 - Temperature tuning of DBR laser and FP laser

On our DBR lasers, we usually could see very small modehops from one lasing mode to the next. These wavelength jumps were only around 0.2 nm in wavelength as seen in figure 5.6 (left); they correspond to the longitudinal mode separation of a 600 µm long DBR-cavity. For the explanation of this phenomenon, it is important to know that our DBR lasers can be considered as FP-lasers with one wavelength-selective mirror. As shown in figure 5.6, the longitudinal mode separation of 0.2 nm indicates that more than just one FP-mode occurs within the 1 - 2 nm wide Bragg peak.

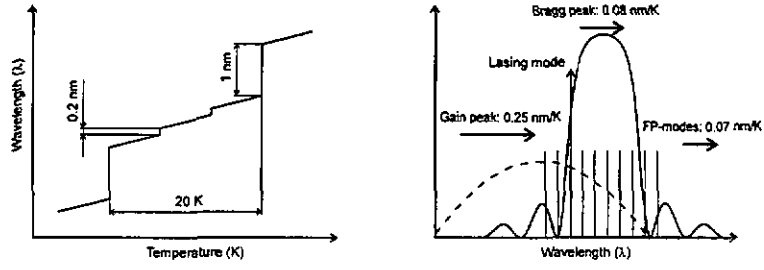

Fig. 5.6 - Schematic picture of the modehop-behavior (left) and the different T-dependencies of gain and Bragg peaks (right)

If the gain peak is shifted to the short wavelength side of the Bragg peak at room temperature (see figure 5.6 right), the shortest-wavelength FP-mode within the Bragg peak will always lase. According to

$$\frac{d\lambda_{FP}}{dT} = \lambda_{FP} \frac{\ell \cdot \left(\frac{\partial \bar{n}_{eff}}{\partial T} + \Gamma \frac{\partial \bar{n}_{active}}{\partial N} \cdot \frac{dN_{th}}{dT} \right) + L_{eff} \cdot \frac{\partial n_{eff}}{\partial T}}{\ell \cdot \bar{n}_{eff}(\lambda) + L_{eff} \cdot n_{eff}(\lambda)} < \frac{d\lambda_{Bragg}}{dT} \qquad (5.5)$$

and

$$\frac{d\lambda_{Bragg}}{dT} = \frac{\lambda_{Bragg}}{n_{eff}(\lambda)} \cdot \frac{\partial n_{eff}}{\partial T} \qquad (5.6)$$

and in agreement with the schematic representation of the tuning coefficients in figure 5.6, the FP-modes tune more slowly with increasing temperature than the Bragg peak. In the previous equations, λ_{FP} and λ_{Bragg} are the wavelength of the lasing FP-mode and the Bragg wavelength, respectively; $n_{eff}(\lambda)$ and $\bar{n}_{eff}(\lambda)$ the wavelength-dependent refractive indices of pumped and Bragg section; n_{eff} and $\bar{n}_{eff}$ the effective refractive indices of pumped and Bragg section for the Bragg wavelength; n_{active} the refractive index of the active layer; N and N_{th} the carrier density and the threshold carrier density; ℓ and L_{eff} the pumped section and the effective grating length; $\Gamma = 0.41$ the confinement factor of the core and T the temperature.

Due to the different T-tuning coefficients of Bragg peak and FP-modes, the progressively longer-wavelength modes will start to lase successively, corresponding to the 0.2 nm jumps in the left picture of figure 5.6. The larger, up to 1 nm wide, wavelength jumps occur if the Bragg peak is essentially broader than the separation between two neighboring FP-modes. If the gain peak of such a device shifts into the center of the Bragg peak by temperature, all modes within the Bragg peak have almost the same reflectivity, and the DBR laser will exhibit a T-tuning behavior similar to a FP laser in this T-range.

The wavelength-dependent effective index, $n_{eff}(\lambda)$, and the effective index at λ_{Bragg}, n_{eff}, of both pumped and Bragg section correspond to the phase and the group velocities of the traveling wave, respectively, and depend on each other as follows:

$$n_{eff}(\lambda) = n_{eff} - \lambda \frac{\partial n_{eff}}{\partial \lambda} \qquad (5.7)$$

The value of the dispersion term in equation (5.7) can be calculated using a table with wavelength-dependent refractive indices [71]; we estimated $\partial n_{eff} / \partial \lambda = -2.5 \times 10^5\ m^{-1}$. Since this dispersion term is small, we can set n_{eff} and $n_{eff}(\lambda)$ equal, $n_{eff} = n_{eff}(\lambda) = 3.24$. In the Bragg section, $\bar{n}_{eff}(\lambda)$ and $\bar{n}_{eff}$ are set equal at 3.16.

A quantitative analysis of the T-tuning coefficients of Bragg peak and lasing FP-mode of the DBR laser exhibited theoretical values of $d\lambda_{FP}/dT = 0.062$ nm/K and $d\lambda_{Bragg}/dT = 0.078$ nm/K, when assuming a T-dependence of the effective refractive index of $\partial n_{eff}/\partial T = 3x10^{-4}$ K^{-1} (calculated using equation (5.6)), a carrier-induced refractive index change of $\partial n_{active}/\partial N = -0.6x10^{-20}$ cm^3 (according to references [72], [73] and [74]), and a T-dependence of the threshold carrier density of $dN_{th}/dT = 3x10^{16}$ cm^{-3} K^{-1} (see reference [64]).

According to Suematsu [64] and in agreement with our experimental data, this results in 0.2 nm-mode-hopping every 10 - 15 K, when operating the laser in a mode which is on the blue end of the Bragg peak. The modehop-free T-range can vary from device to device, corresponding to the different T-dependencies of Bragg peak and FP-modes. Due to the different temperature tuning coefficients of gain- and Bragg peak of a DBR laser, we can always reach the T-range, at which the gain peak matches exactly the position of the Bragg peak by heating. Although this is the desired regime of maximal grating reflectivity, a strong grating with $\kappa >> 100$ cm^{-1} and a wide Bragg peak ($\Delta\lambda_{Bragg} >> 1$ nm) can cause an undesired FP-laser-like T-tuning behavior. In conclusion, small DBR laser mode-hops can be seen whenever we have a mismatch between gain peak and Bragg peak at room temperature. For strong gratings and an exact match between gain and Bragg peak, 1 nm modehops are expected.

5.4 INTEGRATION

As a prototype integrated circuit, we fabricated a DBR laser with a non-absorbing grating section, a transparent waveguide and an absorbing photodetector [75], [76]. The absorbing and transparent areas of this device were defined by VED, thereby demonstrating the ability of a combined VED/DBR laser process to fabricate PICs of increasing complexity [77]. A schematic picture of the device is shown in figure 5.7.

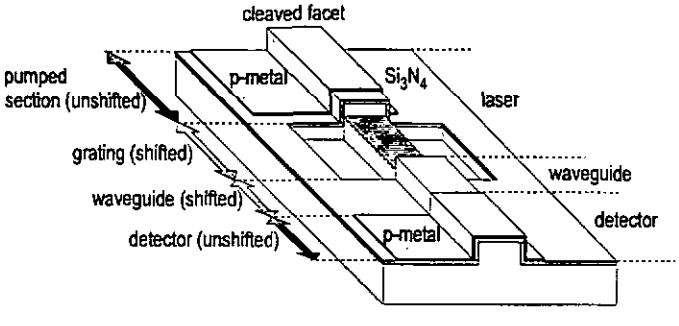

Fig. 5.7 - Schematic picture of an integrated circuit with DBR laser, transparent waveguide and photodetector

The pumped laser section and waveguide photodetector were each 500 μm long. The length of the grating section was 130 μm and that of the transparent waveguide 570 μm; a ridge width of 3 μm was employed. The use of a 70 nm buffer layer between waveguide core and bottom of the grating, and the short grating section, were responsible for the large amount of light transmitted by the grating section. We calculated a grating reflectance of 50 %, in fair agreement with the measured value (30 - 40 %) obtained through a subsequent cleave and anti-reflective coating of the facets behind the photodetector and the transparent waveguide section. The grating period was 380 nm, giving raise to laser emission at 814 nm with a sidemode suppression ratio of 25 dB. This peak could be temperature-tuned with a tuning coefficient of $d\lambda/dT = 0.06$ nm/K, compared to $d\lambda/dT = 0.25$ nm/K at FP lasers of the same processing run. The blue-shift between PL spectra of shifted and unshifted areas was only 17 nm and achieved by a 25 s RTA at 960 °C. This procedure resulted in 30 dB/cm absorption loss in the waveguides.

Based on the detector responsivity of 0.6 A/W, the waveguide length of 570 μm, the waveguide loss of 30 dB/cm, and the results shown in figure 5.8, we could determine the output power on both sides of the laser. We achieved nearly balanced output power emerging from both cleaved facet and grating mirror. External quantum efficiencies of $\eta = 0.21$ W/A from the cleaved facet and $\eta = 0.13$ W/A from the grating side facet were observed. The differential quantum efficiency was thus 20 %. Small ripples in the P-I-curve of these DBR lasers were noticeable; they indicate that the laser has to optimize its internal stored energy under changing phase conditions due to carrier- and temperature-induced refractive index changes. Such ripples are unique features of a laser with a wavelength-selective (DBR) and a nonwavelength-selective mirror (cleaved facet). A typical threshold current of 22 mA was measured on these devices.

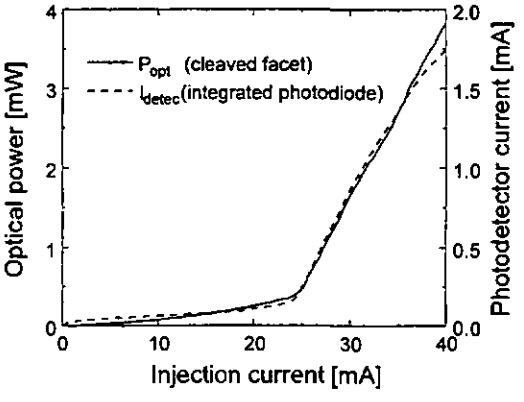

Fig. 5.8 - Optical power and photodetector current versus laser injection current

As mentioned above, the photodetector showed a high responsivity of 0.6 A/W, implying 90 % quantum efficiency. At injection currents above 35 mA, the photodetector seemed to saturate. Because of the poor electrical isolation between laser and photo-detector, we biased the detector with a voltage of 0 V during these measurements. Main reason for the saturation mentioned above was probably this missing reverse voltage on the photodiode. Under reverse voltage, an ohmic leakage current was seen,

indicating a resistance of only 5 kΩ between the two active devices. Nevertheless, the successful combination of a single-growth-step light emitter and a postgrowth bandgap-engineering technique has been shown.

In future processing runs, we could suppress this electrical crosstalk by inserting two additional process steps. These process steps were the proton implantation of all non-waveguiding areas and the removal of the highly p-doped cap layer outside all contact areas. A narrow 2 μm wide implanted stripe across the waveguide and the missing cap layer guaranteed the electrical isolation between adjacent active devices and also between active devices and waveguides.

[62] D. Hofstetter, H.P. Zappe, J.E. Epler, and J. Söchtig, "Single-growth-step GaAs/AlGaAs distributed Bragg reflector lasers with holographically-defined recessed gratings", *Electron. Lett.*, vol. 30, no. 22, pp. 1858 -1859, 1994

[63] K. Kojima, S. Noda, K. Mitsunaga, K. Kyuma, and K. Hamanaka, "Continuous wave operation of a surface-emitting AlGaAs/GaAs multiquantum well distributed Bragg reflector laser", *Appl. Phys. Lett.*, vol. 50, no. 24, pp. 1705 - 1707, 1987

[64] Y. Suematsu, S. Arai, and K. Kishino, "Dynamic single-mode semiconductor lasers with a distributed Reflector", *J. Lightwave Technol.*, vol. LT-1, no.1, pp. 161 - 176, 1983

[65] W.-T. Tsang and S. Wang, "GaAs-$Ga_{1-x}Al_xAs$ double-heterostructure injection lasers with distributed Bragg reflectors", *Appl. Phys. Lett.*, vol. 28, no. 10, pp. 596 - 598, 1976

[66] W. Ng, H.W. Yen, A. Katzir, I. Samid, and A. Yariv, "Room-temperature operation of GaAs Bragg-mirror lasers", *Appl. Phys. Lett.*, vol. 29, no. 10, pp. 684 - 686, 1976

[67] H. Kawanishi, Y. Suematsu, and K. Kishino, "GaAs-$Al_xGa_{1-x}As$ integrated twin-guide lasers with distributed Bragg reflectors", *IEEE J. Quantum Electron.*, vol. QE-12, no. 2, pp. 64 - 65, 1977

[68] T.L. Koch and U. Koren, "Semiconductor lasers for coherent optical fiber communications", *J. Lightwave Technol.*, vol. LT-8, no. 3, pp. 274 - 293, 1990

[69] J.S. Major, Jr., S. O'Brien, V. Gulgazov, D.F. Welch, and R.J. Lang, "High-power singlemode AlGaAs distributed Bragg reflector laser diodes operating at 856 nm", *Electron. Lett.*, vol. 30, no. 6, pp. 496 - 497, 1994

[70] T. Hayakawa, K. Matsumoto, M. Morishima, M. Nagai, H. Horie, Y. Ishigame, A. Isoyama, and Y. Niwata, "High power AlGaAs quantum well laser diodes prepared by molecular beam epitaxy", *Appl. Phys. Lett.*, vol. 63, no. 13, pp. 1718 - 1720, 1993

[71] J.P. Weber, "Propagation of light in periodic structures: application of the surface-emitting laser-diode", *Dissertation UC Berkeley*, 1990

[72] N.K. Dutta, N.A. Olsson, and W.T. Tsang, "Carrier induced refractive index change in AlGaAs quantum well lasers", *Appl. Phys. Lett.*, vol. 45, no. 8, pp. 836 - 837, 1984

[73] M. Ito and T. Kimura, "Carrier density dependence of refractive index in AlGaAs semiconductor lasers", *IEEE J. Quantum Electronics*, vol. QE-16, no. 9, pp. 910 - 911, 1980

[74] J. Manning, R. Olshansky, and C.B. Su, "The carrier-induced index change in AlGaAs and 1.3 μm InGaAsP diode lasers", *J. Quantum Electron.*, vol. QE-19, no. 10, pp. 1525 - 1530, 1983

[75] D. Hofstetter, H.P. Zappe, and J.E. Epler, "Ridge waveguide DBR laser with nonabsorbing grating and transparent integrated waveguide", *Electron. Lett.*, vol. 31, no. 12, p. 980 - 982, 1995

[76] D. Hofstetter, H.P. Zappe, J.E. Epler, and P. Riel, "Monolithically integrated DBR laser, detector, and transparent waveguide fabricated in a single growth step", *IEEE Photonics Technol. Lett.*, vol. 7, no. 9, pp. 1022 - 1024, 1995

[77] S.G. Ayling, J. Beauvais, and J.H. Marsh, "A DBR laser using dielectric cap disordering and strontium fluoride masking", *Proc. ECIO'93 Neuchâtel (Switzerland)*, pp. 7-10 - 7-11, 1993

6. MONOLITHICALLY INTEGRATED OPTICAL DISPLACEMENT MEASUREMENT CHIP

In this section, we describe the fabrication procedure, the characterization, and the measurement results of our displacement sensors. We discuss first the single Michelson interferometer, and a second part contains the double Michelson interferometer work. Details of the fabrication will be presented in the appendix.

6.1 PROCESS RECAPITULATION

The full interferometer process will be described step by step in the appendix, therefore we will give here just an overview of all processing steps, without going into too much detail. For the fabrication of the monolithically integrated interferometer as presented in section 2.2.6, we used one epitaxial growth step, 8 photolithography steps and one holographic exposure. Since we usually worked with quarters of 2 inch GaAs wafers, our masks covered an area of 20 x 20 mm^2. Smallest dimensions on the masks were 1 μm; this allowed fabrication by laser writing instead of e-beam writing.

6.1.1 *Layer structure*

The layer structure used for these monolithically integrated interferometers was grown by metal-organic vapor phase epitaxy on a GaAs substrate (n-doped 1.2x10^{18} cm^{-3} Si) in a single growth step. It included an undoped 165 nm thick $Al_{0.3}Ga_{0.7}As$ waveguide core containing a single GaAs quantum well (7 nm). This higher refractive, waveguiding layer was

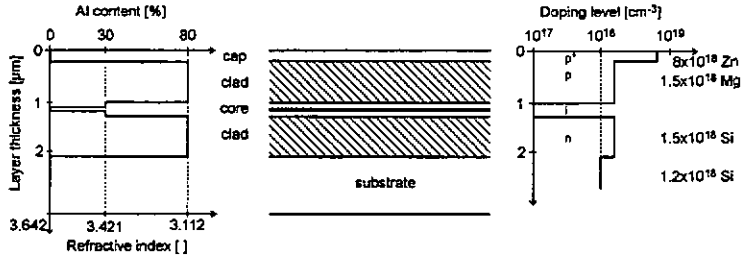

Fig. 6.1 - Layer thicknesses and doping levels of our separate confinement double-heterostructure

sandwiched between a 1.1 μm thick $Al_{0.8}Ga_{0.2}As$ lower cladding layer (n-doped 1.5x10^{18} cm^{-3} Si) and an 0.85 μm thick $Al_{0.8}Ga_{0.2}As$ upper cladding layer (p-doped 1.5x10^{18} cm^{-3} Mg). A 160 nm thick highly p-doped (8x10^{18} cm^{-3} Zn) GaAs contact layer completed the structure, as depicted in figure 6.1. The characterization of the quantum well structure was performed by measuring the PL spectrum (see also section 4.3). The doping levels were measured by

repeated etching of the surface and a subsequent determination of the conductivity (Polaron); the lattice constant was determined by X-ray diffraction. The substrate thickness of 400 µm allowed a minimal cleaved laser bar length of 1 mm. For FP laser fabrication, it was often necessary to cleave shorter pieces. This required wafer thinning to a minimal thickness of around 100 µm by grinding and subsequent polishing. The polishing is not compulsory, but the surface roughness causes some strain in the material; on thin wafers this can result in bending. For the elimination of this strain, the wafer surface can also be wet etched in a citric acid/hydrogen-peroxide solution. The minimal material thickness to be etched is twice the grain size of the grind.

6.1.2 *Interferometer process*

As shown in figure 6.2, processing started with the e-beam evaporation of 200 nm SiO_2. This layer was patterned in a first photolithography step and RIE. Without stripping the photoresist, we then evaporated 300 nm of SrF_2 in

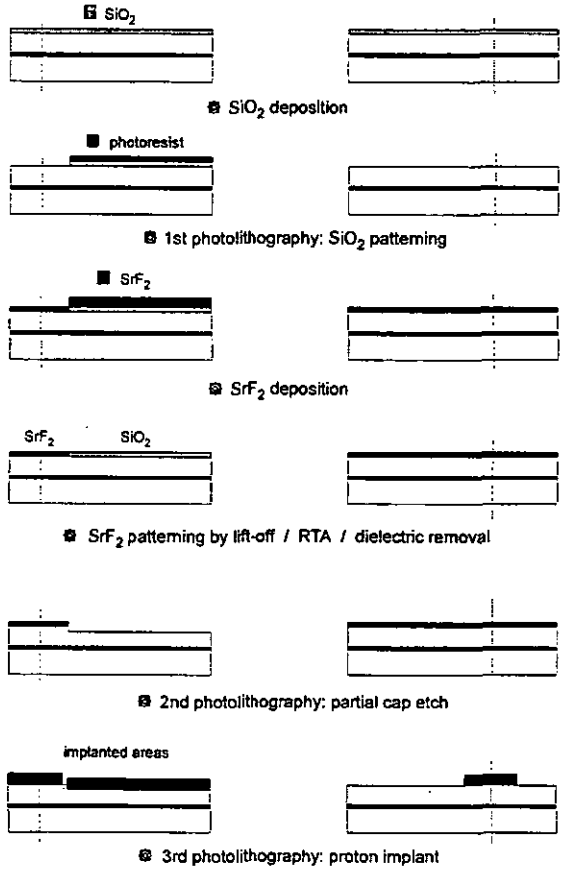

Fig. 6.2 - Process steps 1 - 6 for interferometer fabrication

a self-aligned process. The patterning of this layer was performed by a lift-off process in Microposit remover 1165. Selective intermixing of the QW under the SiO_2 layer was then accomplished by a 40 s RTA at 960 °C. The two dielectric layers were then removed by RIE (SiO_2) and a subsequent dip in diluted HCl (SrF_2). In a second photolithography step, we prepared the chip for cap etch, which was done using a citric acid-based wet etchant. The GaAs cap layer was removed everywhere except in the contact region; this reduced the electrical crosstalk.

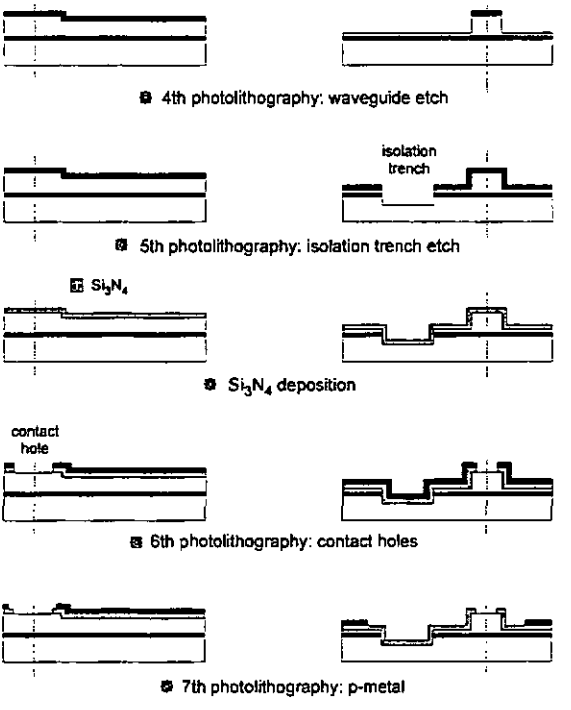

Fig. 6.3 - Process steps 7 - 11 for interferometer fabrication

The third photolithography step used a 2.8 μm thick photoresist mask in order to protect the waveguiding regions from being proton-implanted. Proton implantation was performed at three different energies (40/70/100 keV) and a dose of 4×10^{15} cm^{-2}. After a 30 min O_2 plasma ash to remove the resist mask, we exposed the fourth photolithographic mask for dry etching the ridge waveguides (see figure 6.3). The etch depth of this MERIE step was defined to result in a residual clad thickness of 100 nm above the core. Using the same etch conditions, we dry etched the optical isolation trench between laser and photodetector ridge after the fifth photolithography step.

The sample was then covered with a 250 nm thick PECVD Si_3N_4-layer in order to passivate and electrically isolate the sidewalls of the ridges. After the

sixth photolithography step, which was used for the definition of the contact holes on top of the ridge waveguides, we dry etched the Si_3N_4-layer by RIE using CF_4. The next, hence seventh, photolithography step was carried out with Hoechst AZ 5214 image reversal photoresist, resulting in an undercut mask profile; this was necessary for patterning the p-metalization. After evaporation of the p-metal layers (Ti/Pt/Au), we patterned these by a lift-off process using acetone (figure 6.4). Following the optional thinning of the substrate, we evaporated the n-metal layers (Ge/Au/Ni/Au) and annealed both p- and n-contacts in the RTA oven at 435 °C.

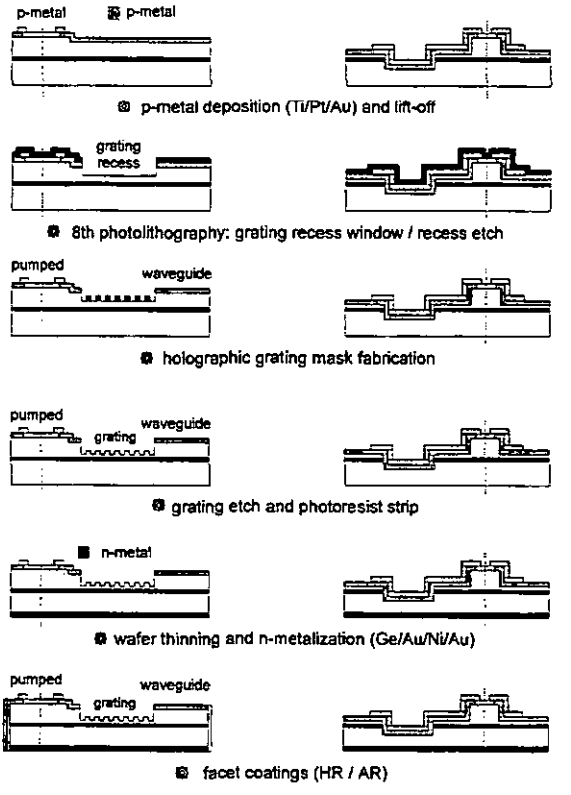

Fig. 6.4 - Process steps 12 - 17 for interferometer fabrication

The eighth and therefore last photolithography step defined the grating recesses; these were again etched by CF_4-RIE and MERIE to a depth of 230 nm above the core. Spinning of a very thin photoresist layer prepared the sample for holographic grating exposure using a HeCd-laser. Following development (Microposit developer/H_2O, 1:1) and a double-sided 4 nm thin Cr-evaporation on top of the photoresist grating profile, we carried out an anisotropic O_2-RIE. This process resulted in a clean grating mask, which was transferred into the remaining upper clad of the recessed waveguide again by MERIE. After the removal of this grating mask, we cleaved the wafer into

bars of 1.95 and 2.6 mm in length. Finally, an AR-coating on the measurement facet and an HR-coating on the laser facet was evaporated. These facet coatings should be understood rather as facet passivation layers and not as essential for CW laser operation and good signal contrast.

6.2 CHIP DESCRIPTION

In the following, we describe two different devices: the first is a single Michelson interferometer (SMI) such as shown schematically in figure 3.13; the second are configured as double Michelson interferometers (DMIs) and their schematic pictures are shown in figures 2.3 and 2.4. The SMI consisted of a DBR laser, a directional coupler, and a photodetector, while the more complicated DMI employed a DBR laser, two Y-couplers, two directional couplers, two photodetectors and two phase shifters. As already mentioned in section 2.2.6, we also fabricated DMIs without any directional couplers, but with four Y-couplers (figure 2.4). This measure resulted in a shorter total device length of only 1.95 mm. The length of the DMI with two directional couplers was 2.6 mm; the SMI was again 1.95 mm long. An individual SMI had therefore a size of 1.95 x 0.25 mm^2, while DMIs were 2.6 x 0.35 mm^2 in size.

The pumped laser section and the waveguide photodetector were both 500 μm long; ridge width was 3 μm for all waveguides. The phase shifters in the two reference arms had a length of 340 μm, which was somewhat too short (see section 2.2.5). For the fabrication of the first generation SMIs, we employed three different coupler lengths of 100, 275 and 450 μm. The variation of the grating length was 150 and 200 μm. In the course of the experiments, the 450 μm coupler length and the 200 μm grating section length gave best results with respect to splitting ratio of the coupler and threshold current density of the laser. Therefore we decided to use these lengths in the second generation SMIs and DMIs consequently.

Since curves with a too small radius can change the modal behavior of an originally monomode waveguide, we tried to work with a larger curve radius of 5 mm instead of the previously fabricated 500 μm. This reduced the width of the chip from 0.35 mm to 0.25 mm, and the total chip size of a DMI to about 2.6 x 0.25 mm^2. Due to the small distance between laser and photodetector (only 40 μm) of these R = 5 mm-interferometers, we expected them to have a *slightly* higher optical crosstalk than the R = 500 μm-devices with 125 μm distance between laser and photodetector. Unfortunately, the isolation trench was too shallow, resulting in a *much* higher optical crosstalk of these R = 5 mm-devices. Therefore, no successful operation of them was demonstrated.

As a further alternative, we fabricated DMIs using a 3x3-coupler structure. Such devices have been reported to result in an automatic phase quadrature, when using one of the outer waveguides as measurement arm

[78], [79]. Since our experiments showed a wide distribution of the phase between the two interference signals, we were not able to distinguish between processing-induced and design-inherent phase difference variations. Nevertheless, the 3x3-coupler structure has its advantages: Y-couplers were often responsible for mode conversion in the measurement arm, and an elimination of Y-coupler-based beam splitters could improve the quality of the mode behavior. For an improvement of the phase behavior, it will be very important to use monomode waveguides and an improved Y-coupler design with a tapered section.

As shown in the process recapitulation (section 6.1), we used facet coatings in the first SMI fabrication run. The HR-coating of the laser facet consisted of an e-beam evaporated, $\lambda/4$ SiO_2-layer (141 nm, n = 1.45, resulting in a total phase change per pass of $\pi/2$), and a $\lambda/4$ Al-mirror (75 nm, n = 2.745, resulting in a additional reflection-induced phase shift of π). This HR-coating improved the facet reflectance from 30 % to about 92 %; the threshold current was reduced from 60 mA to around 35 mA [80]. On the measurement facet, we evaporated a one layer AR-coating consisting of a $\lambda/4$ Balzers PASO III-layer (108 nm, n = 1.9, total phase shift π). This AR-layer reduced the reference signal by a factor of 15, due to a residual reflectance of 2 %. The measurement signal increased by a factor of 2, due to the smaller facet reflection. This adaptation of the relative signal amplitudes of reference and measurement beam improved the contrast of the total interference signal. But the considerable reduction of the reference beam intensity resulted in a net reduction of the signal amplitude. In the second fabrication run, we therefore eliminated the facet coatings in favor of improved laser and directional coupler performance.

6.3 MEASUREMENT SETUP

A test bench for the characterization of optical Michelson interferometers was set up in the course of this work. All optical components

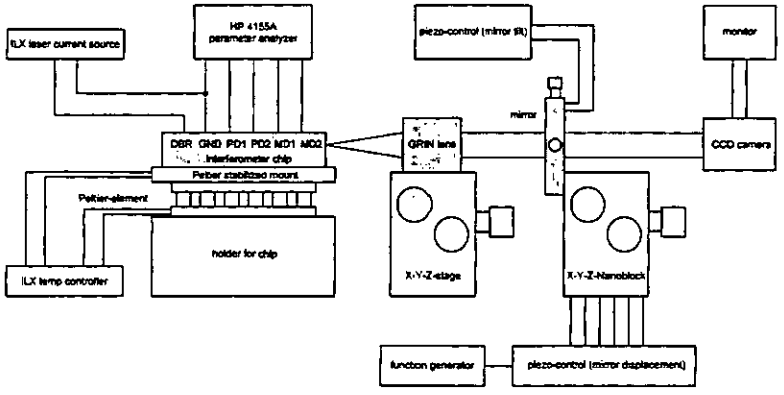

Fig. 6.5 - The schematic picture of the measurement setup for interferometer characterization

were mounted on an Al-rail which allowed a fast exchange or movement of the single components. As shown in figure 6.5, these components were the temperature-stabilized mount for the interferometer chip, the micromanipulator holding the external gradient index (GRIN) lens, the movable, semi-transparent object mirror and the CCD camera with its ancillary lens.

For the temperature-stabilization, we used a 15 x 15 mm^2 Peltier-element (thermo-electric heat pump) with a thermo-resistor, and an ILX temperature controller (ILX LDT-5910B). This equipment allowed temperature stabilization to within ± 50 mK. The temperature-stable mount itself was a 24 x 40 mm^2 Al block, on which we placed and contacted the interferometer chips in bar form. For contacting the active devices, we used the same probers as for laser testing (The Micromanipulator Co.). The detector current measurements and the control of the modulator voltages were realized by an HP 4155A semiconductor parameter analyzer. Because of the relatively slow sampling rate of only 3 Hz, we were restricted in the displacement speed. The DBR laser was powered by a separate laser diode current source (ILX LDP-3811) which allowed pulsed or continuous wave operation of the laser. Thanks to the monolithic integration of all necessary optical functions, we needed only one additional external optical element; this element was the GRIN lens for measurement beam collimation. Its pitch of 0.23 required 0.5 mm distance from the measurement facet; this reduced the risk of scratching the interferometer facet. In a more advanced system, however, the GRIN lens would be fixed onto the chip, requiring a quarter pitch GRIN lens.

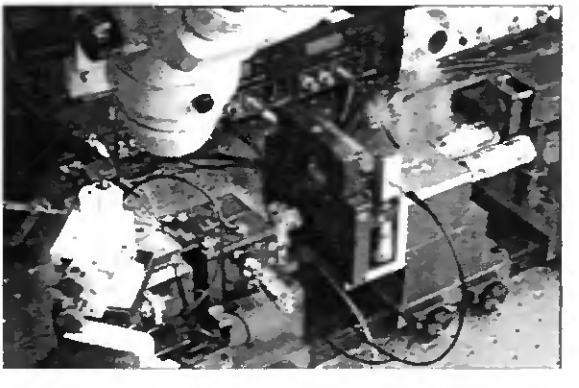

Fig. 6.6 - Photograph of the measurement setup for interferometer characterization

Figure 6.6 shows a photograph of the measurement setup. The white object at the left is one of the probers; right behind it, the mount for the chip can be seen. The block with the three small micrometer screws holds the GRIN lens, and the larger block with the electrical connection bears the gimbal-mounted mirror. On the right side of the picture is the CCD camera

with the lens. The background of the picture is filled with the piezo-control units, and on the top one can see the microscope for optical inspection of the probers on the chip.

The movable object for these measurements was a semi-transparent mirror, which could be moved and tilted in two axes by piezo-actuators. The linear displacement was performed by a Photon Control X-Y-Z-stage (Nanoblock) and controlled by a piezo-control unit (Melles Griot 17PCZ003) with feedback loop. Maximum drive voltage of the piezo-actuators was 75 V. A 5 nm positioning accuracy with a repeatability of 5 nm was guaranteed by the manufacturer.

For testing of the SMIs, we controlled the mirror movement by an external voltage ramp. A continuous displacement of 20 μm in one direction was achieved. The characterization of the DMIs required periodic changes of the movement direction; therefore, we used a symmetric sawtooth voltage from a function generator to drive the piezo-control. The magnitude of this voltage was adjusted to change the direction after each 2 μm and its frequency of 0.0167 Hz induced such changes every 1 min. These conditions gave best results in combination with the sampling rate of the detector current measurement.

The use of a semi-transparent object mirror and the CCD camera facilitated the rough alignment of the measurement beam into autocollimation. Fine adjustment was carried out during the measurement by optimizing the detector signal. For this alignment, we used a gimbal mirror mount with two piezo-actuators, the latter resulting in a tilt accuracy of 0.33 μrad/V in the horizontal and of 0.67 μrad/V in the vertical direction. The piezo-control unit for the tilt control (Physics Instruments P 263-20) supplied the piezo-actuators with a voltage of maximally -1000 V.

6.4 MEASUREMENT RESULTS

The SMIs fabricated in the first fabrication run were tested at room temperature when driving the DBR laser with an injection current of 50 mA CW. The laser threshold current was I_{th} = 35 mA, resulting in a threshold current density of 2.2 kA/cm². Emission wavelength was 820 nm, and the sidemode suppression ratio was determined to 25 dB. During the measurements, the photodetector was reverse biased at -5 V; the leakage dark current at this voltage was 500 pA. Between adjacent laser- and photodiodes, a resistance of 10 GΩ was seen; thus the resistance increased by a factor of 10^6 due to the proton implantation and the cap etch. Typical responsivity of these photodetectors was 0.5 A/W. Figure 6.7 shows part of a measured interferogram for a mirror distance of 3 cm and a mirror reflectance of 95 %. The maximal resolution of this measurement was one quarter of a fringe, thus

100 nm. The maximal measurement distance was, limited by the enhanced laser linewidth, 45 cm.

Interference measurements at constant mirror distance but using different mirror reflectances allowed the determination of the optical crosstalk between laser and photodetector. For the interferogram in figure 6.7, we estimated the optical crosstalk to be 15.8 nA; subtracting this value led to a signal contrast of V = 0.8 [81]. The experimental determination of the crosstalk signal current required the following procedure: the interference signals for 13 cm mirror distance and five different mirror reflectances (r = 0, 5, 54, 67 and 95 %) were measured. Then the resulting averaged detector signals and the signal amplitudes served as input numbers for the subsequent calculation. This calculation used the equations (3.15), (6.1) and (6.2) five times each, and finally, a least squares fit was used to determine the five unknowns. These were: crosstalk signal (I_{cross}), DBR laser output (I_0), intrinsic phase difference (ϕ), parasitic facet reflectivity (r_0), and GRIN lens coupling loss (C). The averaged detector signal, $I_{average}$, is defined by

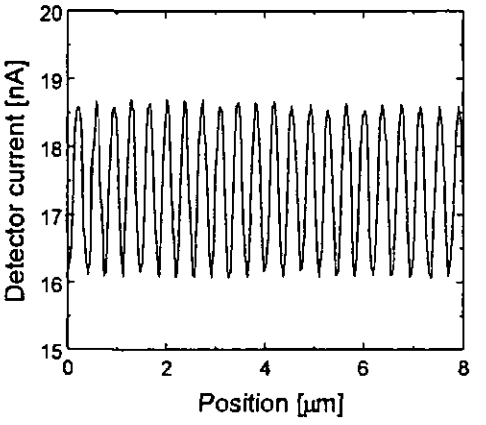

Fig. 6.7 - Interferogram for 3 cm mirror distance as measured by integrated photodetector

$$I_{average} = \frac{1}{2}(I_{max} + I_{min}) \tag{6.1}$$

where I_{min} and I_{max} are the minimal and maximal detector signals, respectively. The symbol A in

$$A = \frac{1}{2}(I_{max} - I_{min}) \tag{6.2}$$

stands for the amplitude of the interference. With the help of (3.15), (6.1) and (6.2), we were able to calculate the averaged detector signals as well as the signal amplitudes as a function of the five unknowns. Since we measured with five different mirror reflectances, we obtained five equations for averaged signal and another five for the signal amplitude. Finally, the least squares fit solved the over-determined system of equations (10 equations for 5 unknown numbers). As already mentioned, we obtained a value of 15.8 nA for the crosstalk; the total coupling loss in both directions through GRIN lens and AR-coated facet was on the order of 15 dB. The calculated values for the

five unknowns were thus: I_{cross} = 15.8 nA, I_0 = 7.1 nA, r_0 = 3 %, C = 40 %, and ϕ = 3 rad.

Concerning the optical crosstalk, we decided to insert an optical isolation trench between the active devices. This feature can reduce the crosstalk considerably. To improve its action, we refilled the trench with the p-metal layers; this should hinder the light from going directly into the photodetector. The limited etch depth of this trench resulted in no considerable crosstalk reduction.

In order to determine the maximal object distance, we measured the signal contrast or visibility, defined by

$$V = \frac{I_{max} - I_{min}}{I_{max} + I_{min} - 2I_{cross}} \tag{6.3}$$

as a function of mirror distance, z [82].

The Fourier-transform of this so-called auto-correlation function, V(z), is the lineshape of the light source; the maximal mirror distance at which interference can be seen is one half of the laser's coherence length. For our SMIs we observed, as indicated in figure 6.8, a fairly rapid decrease of the visibility with increasing mirror distance. For constant mirror reflectance (r = 67 %) and 3 cm distance, a contrast of 0.58 was measured, but at a distance of 45 cm, the visibility dropped to 0.03. The coherence length, $L_c = c/\Delta\nu$, of the integrated DBR laser is therefore 1 m; the linewidth $\Delta\nu$ = 500 MHz. A control measurement of this value using a scanning FP spectrum analyzer resulted in a similar linewidth; however, the spectrum looked rather noisy. The reason for this enhanced linewidth was probably the disturbance of the laser activity through too much feedback caused by facet reflections. Without using optical isolation, it might be difficult to improve the laser properties.

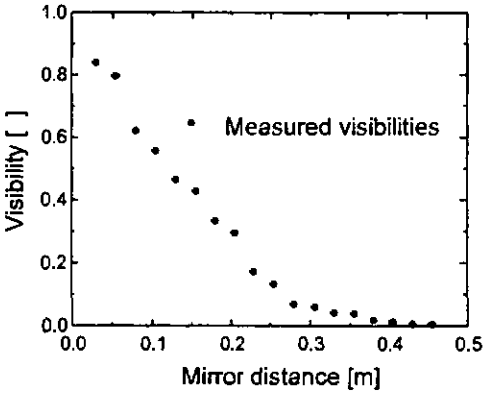

Fig. 6.8 - Measured signal contrast versus mirror distance (67 % reflectance)

6.5 DIRECTION DETERMINATION

In order to recognize a change in movement direction, and also for resolution improvement, we fabricated DMIs in a second processing run. As described in section 6.2, the realization of these devices required the

monolithic integration of many more optical components. The photograph of figure 6.9 gives an idea of the complexity of such structures.

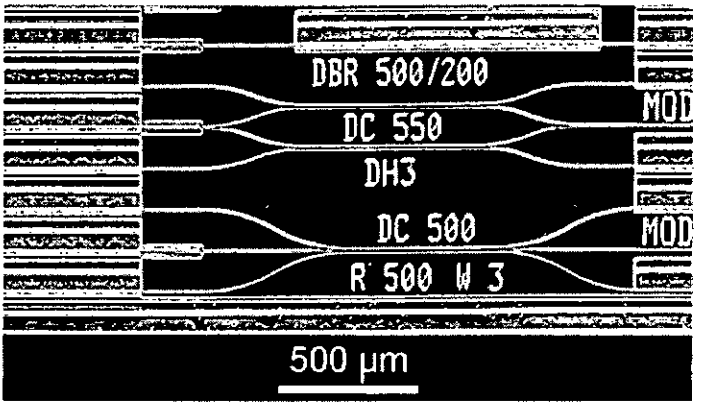

Fig. 6.9 - Photograph of a monolithically integrated displacement measurement chip with direction determination

The picture shows two complete DMIs, the upper one with two directional and two Y-couplers, the lower one with one 3x3-coupler. The 500 µm long rectangles on the left side are contact pads of DBR lasers and photodetectors. The small 200 µm long boxes next to them are the grating recesses, and the 340 µm long contact pads on the right side are phase shifters. The characterization of these interferometers was performed with exactly the same setup as before. The only differences concerned the control voltage for the piezo-actuated mirror displacement, and the acquisition of two detector signals instead of one.

We carried out these measurements by using a reverse voltage of -12 V on the detectors in order to guarantee as large signals as possible. The electrical crosstalk was very small, in the range of 100 pA, corresponding to a resistance between neighboring diodes of 10 GΩ. The optical crosstalk of these devices could be measured by suppressing all parasitic facet reflections before cleaving the measurement facet. To improve optical isolation, we etched (in favor of the p-metal-filled, not sufficiently deep isolation trench) trenches between the metal pads of lasers and photodetectors; these were not filled with metal layers. The result was an asymmetric and still relatively high crosstalk into the two photodetectors, asymmetric because of the different distances of the laser ridge to the trench on the right and the left sides of the laser. Typical crosstalks of 35 nA and 16 nA were seen.

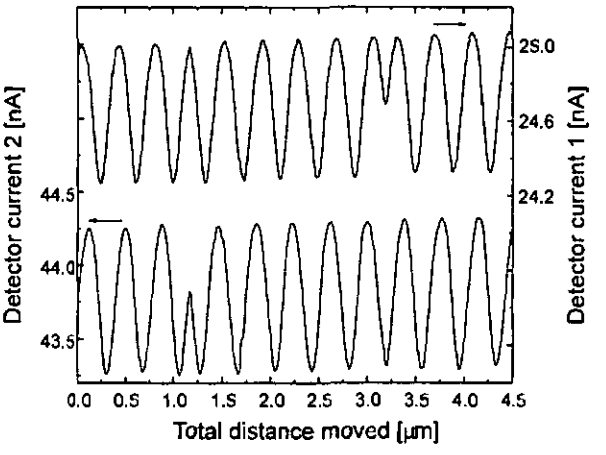

Fig. 6.10 - The two detector currents of the DMI for 3.5 cm mirror distance and 67 % mirror reflectance

Figure 6.10 shows the two detector signals as a function of the total distance moved. The signal amplitudes were 0.5 nA and 0.4 nA. At 1.2 and 3.2 µm, there are changes of movement direction, indicated by the discontinuities in the lower and the upper interference signals, respectively. The slightly skewed shape of the interferograms corresponds to that predicted in section 3.5.

The measurement presented here was carried out with no phase shifter voltage; we thus see that the accidental phase shift due to length differences of the two reference arms can produce nearly the desired phase shift of 90 °. Through a measurement with -12 V reverse voltage on one of the phase shifters, we achieved a maximal phase change of 20 °. For the needed value of 90 °, either a longer phase shifter or more QWs would be necessary.

A change of the relative phase between the two signals could also be achieved passively by changing the feedback conditions of the measurement beam. The presence of different higher order modes in the measurement arm is responsible for the possibility to change the relative phase between the two signals. As already mentioned in section 6.3, we used an external CCD camera for monitoring the position of the reflected sensing beam. In the ideal case, we could see a circular light spot (originating from the emerging sensing beam) and a second, weaker spot (originating from the reflected sensing beam). Changing the feedback conditions means in this context changing the relative position of the spot generated by the reflected measurement beam with respect to the spot produced by the measurement beam emerging from the cleaved facet. This position change leads to the exciting of a different order mode with a slightly different wavelength, and this effect changes the intrinsic phase between each reference arm and the measurement arm. The result is therefore a changed relative phase difference between the two

interference signals. As presumed in section 6.2, the use of Y-couplers for the beam splitting and joining caused some mode conversions, and was not helpful for the waveguides to support exclusively the TE_{00} mode [83].

The maximal measurement distance with the DMI was restricted to 25 cm, corresponding to a coherence length of 0.5 m and a linewidth of 1 GHz. All measurements were carried out using a 67 % reflecting object mirror. In order to improve the resolution of the displacement measurement, we can plot the two detector signals as a function of each other as presented in figure 6.11. This plot is often referred to as Lissajous-figure. The ratio between the two ellipse main-axes indicates that we achieved a phase difference of 70 ° between the interferometer signals. In the ideal case of 90 ° phase difference and equal signal amplitudes, a circle would result. Deviations from this ideal shape were also caused by the distorted sine and cosine-signals due the parasitic reflection at the measurement facet. Nevertheless, the displacement measurement using this representation improved the resolution by an order of magnitude. If we assume a maximal phase interpolation of $\phi/20$, we expect a resolution on the order 20 nm.

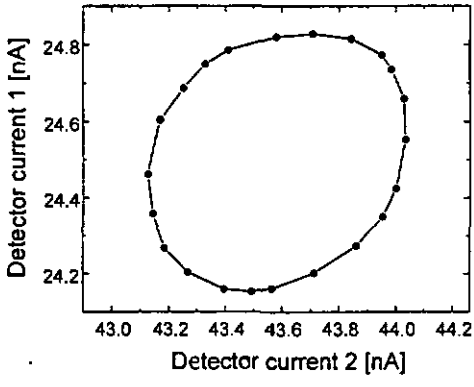

Fig. 6.11 - Plot of the two interferometer signals as a function of each other

For all measurements, we observed a fair vibration sensitivity of the whole interferometer, a high sensitivity to mirror misalignment, and an extreme sensitivity for walking people influencing the very small currents in the measurements cables. The probe needles, with a short unshielded connection to the BNC cables, seemed to act as antennas. Finally, measurement of the interferometer signal without external mirror was used to determine the temperature stability of the device. The standard deviations of the measured noise signals were less than one tenth of the interferometer signals in both directions. A rough estimation of the influence of this noise on the maximal resolution showed a slight degradation of the phase interpolation to within $\phi/15$.

[78] S.K. Sheem, "Fiber-optic gyroscope with [3x3] directional coupler", *Appl. Phys. Lett.*, vol. 37, no. 10, pp. 859 - 861, 1980

[79] H. Gruebel, "Fasergekoppelte Einbaulaserinterferometer mit integriert optischem Sensorkopf', *Technica*, no. 21, pp. 33 - 37, 1992, (in German)

[80] C. Heine, calculation using a AR/HR-layer design program

[81] D. Hofstetter, H.P. Zappe and R. Dändliker, "Monolithically integrated optical displacement sensor in GaAs/AlGaAs", *Electron. Lett.*, vol. 31, no. 24, pp. 2121 - 2122, 1995

[82] D. Hofstetter and H.P. Zappe, "Monolithically integrated interferometer for optical displacement measurement", *Proc. SPIE*, vol 2695, pp. 380 - 391, 1996

[83] D. Hofstetter, H.P. Zappe, and R. Dändliker, "A monolithically integrated double Michelson interferometer for optical displacement measurement with direction determination", to appear in *IEEE Photonics Technol. Lett.*, vol. 8, no. 10, 1996

7. CONCLUSIONS

In this work, we presented the design, fabrication and testing of SMIs and DMIs useful for optical displacement measurement. The fabrication procedure was based on a VED process for bandgap-engineering and the use of a single-growth-step DBR laser as light source of the interferometers. An SMI united a DBR laser, one directional coupler, and a photodetector on a single GaAs-based chip; the DMI contained a DBR laser, two Y-couplers, two directional couplers, two phase shifters, and two photodetectors on the same chip. Both interferometer circuits needed only an external GRIN lens for measurement beam collimation. The minimal resolution of the SMIs was 100 nm, while with the DMIs a resolution of 20 nm could be reached, due to improved phase interpolation. The enhanced laser linewidth of about 500 MHz allowed the measurement at a maximal distance of 45 cm with the SMI and 25 cm with the DMI. With the SMI, we could measure unidirectional movement of an object mirror, and with the DMI, direction changes could be recognized. A direction change was manifested in a discontinuity in one of the two independent interferometer signals. The amplitudes of the two interferometer signals were 0.5 nA and 0.4 nA, a constant offset signal due to optical crosstalk of 35 nA and 16 nA was seen. Although we used a relatively simple processing, various active and passive optical components and functions could be monolithically integrated.

7.1 POSSIBLE APPLICATIONS

Because of the small physical size of the interferometers presented in this work, we propose them for applications in small systems. These include especially micro-electro-mechanical systems (MEMS). Displacement measurements in such systems require high resolution (1 nm), but the measurement distances are rather small, up to a few millimeters. Although our interferometer reached a high degree of monolithic integration, several further developments are required for possible MEMS applications. One is the integration of the beam-shaping element, which might be combined with a means to achieve surface-emission of the sensing beam. For this purpose, a focusing, surface-emitting grating coupler would be a useful structure. The fabrication of such a chirped focusing grating might require an additional electron-beam writing step. A further necessary improvement is the increase of the interferometer resolution. The use of the device to measure the displacement of an AFM-tip or the movement of a membrane requires sub-10 nm-resolution.

A further possible field of application for these interferometers is exact displacement measurement in mechanical workshop-oriented problems. There is considerable interest in replacing the glass rule-based displacement sensing on moving parts of CNC machine tools, or in height gauges, by interferometric methods. For such systems, the use of a monolithically

integrated optical approach would be an important step towards miniaturization and, thanks to the DBR laser as light source, also towards frequency stabilization. The frequency stabilization of a semiconductor laser suffers from the presence of modehops. These can shift the wavelength during operation, and if a hop happens to occur exactly on the wavelength to be locked on, no stabilization is possible. DBR lasers show only few modehops within a wide temperature range, therefore, they are very promising candidates for possible frequency stabilization.

Since our system is considerably smaller than bulk optical interferometers, even when using an external GRIN lens, the presented degree of integration could be sufficient for these applications. Concerning the performance, however, an improvement of the signal contrast, especially at larger distances, is required. For mechanical applications, a resolution on the order of 10^{-6} and a measurement distance of 1 m appear to be standard values. In order to achieve this resolution, a temperature stabilization of the whole chip to within ±10 mK would be necessary. An improvement of the coherence length by a factor of 10 or 20 would help to make the presented system useful for such applications. Due to the adverse operating conditions (changes of temperature, refractive index) in a mechanical workshop, our interferometric displacement measurement system would have to be operated in a well-defined atmosphere when being used in a machine tool.

7.2 IMPROVEMENTS

As already mentioned in section 7.1, some improvements are required when using such interferometers in different applications. In order to improve the signal contrast, a more deeply etched isolation trench is required. This measure will enable operation of the R = 5 mm devices; the latter are expected to guarantee monomode behavior of the waveguides and no mode conversion in the curves.

The size of the measurement signals depends strongly on the absorption loss in the waveguides. A controlled reduction of this loss through a longer RTA step, without affecting laser performance, would therefore be desirable. Also, one of the free parameters for the signal optimization is the laser output power. Although the signal size is only linearly dependent on the laser output, an increase of the latter by a factor of 10, for example by a reduction of the contact resistance, would be helpful for interferometer performance. The output power does not depend on interferometer parameters, and therefore such an increase would not require further design compromises. As a last point, the coupling ratio of the directional- and the Y-couplers should be further optimized towards 50:50 % splitting ratio. This quantity has no influence on the signal contrast, but improves the signal magnitude.

One disadvantage of the monolithic integration of lasers and optical circuits is the large heat dissipation of the light emitter. The produced heat

warms the whole interferometer up and has thus to be dissipated efficiently, in order to enable good temperature stabilization. A measurement resolution of 10^{-6}, often required in mechanical systems, requires a comparable or better laser frequency stability and therefore a temperature stability within ± 10 mK. Locking the laser frequency on a gas absorption line (for example Cs at 852 nm or Rb at 780 nm) can be accomplished by a fast feedback loop and a temperature-tuned control of the laser frequency. This would then include good heat-sinking of the interferometer chip.

Finally, it will be important to guarantee a long lifetime of our DBR lasers. As already mentioned, this can be achieved by a reduction of the p-contact resistance or a by preventing any dopant diffusion during the VED process.

APPENDIX A

A.1 CALCULATIONS

A.1.1 3x3-coupler solved by coupled mode theory

This calculation is based on the theory of coupled modes using perturbation theory and follows the illustration of chapter 13 in the book of A. Yariv [84]. The electric field amplitudes in the three waveguides are represented by the vector components a_i. As shown in figure 3.11, we consider three fibers in an isosceles triangle configuration. The angle between the legs with equal length should be at least 60 °. We thus have a central and two outer waveguides. The number κ governs the coupling strength between central and outer waveguides. The value of $\alpha\kappa$ ($\alpha < 1$ or $\alpha = 1$) is the coupling coefficient between the two outer waveguides.

The matrix equation to be solved is

$$\frac{d}{dz}\begin{pmatrix} a_1 \\ a_2 \\ a_3 \end{pmatrix} = \begin{pmatrix} 0 & -i\kappa & -i\kappa \\ -i\kappa & 0 & -\alpha i\kappa \\ -i\kappa & -\alpha i\kappa & 0 \end{pmatrix} \cdot \begin{pmatrix} a_1 \\ a_2 \\ a_3 \end{pmatrix} \tag{A.1}$$

This equation can also be written in the following abbreviation

$$\frac{d}{dz}\vec{a} = A \cdot \vec{a} \text{ where } \vec{a} = \vec{a}(z) \tag{A.2}$$

If we diagonalize the A, we get matrix

$$J = \begin{pmatrix} \lambda_1 & 0 & 0 \\ 0 & \lambda_2 & 0 \\ 0 & 0 & \lambda_3 \end{pmatrix} = \begin{pmatrix} \frac{i\kappa}{2}\left(-\alpha + \sqrt{8+\alpha^2}\right) & 0 & 0 \\ 0 & \frac{i\kappa}{2}\left(-\alpha - \sqrt{8+\alpha^2}\right) & 0 \\ 0 & 0 & \alpha i\kappa \end{pmatrix} \tag{A.3}$$

with the three eigenvalues, λ_i, of A as diagonal elements. The corresponding basis transformation is defined by

$$J = S^{-1} \cdot A \cdot S \tag{A.4}$$

using

$$S=\left(\sqrt{\frac{2}{8+\alpha^2+\alpha\sqrt{8+\alpha^2}}}\cdot\begin{bmatrix}\frac{-4}{-\alpha+\sqrt{8+\alpha^2}}\\1\\1\end{bmatrix},\sqrt{\frac{2}{8+\alpha^2-\alpha\sqrt{8+\alpha^2}}}\cdot\begin{bmatrix}\frac{-4}{-\alpha-\sqrt{8+\alpha^2}}\\1\\1\end{bmatrix},\begin{bmatrix}0\\-\frac{1}{\sqrt{2}}\\\frac{1}{\sqrt{2}}\end{bmatrix}\right) \tag{A.5}$$

which is an orthogonal matrix. We then solve the diagonalized matrix equation

$$\frac{d}{dz}\vec{b}=J\cdot\vec{b} \tag{A.6}$$

This results in

$$\vec{b}=\begin{pmatrix}b_1(z)\\b_2(z)\\b_3(z)\end{pmatrix}=\begin{pmatrix}b_1^0\cdot e^{\lambda_1 z}\\b_2^0\cdot e^{\lambda_2 z}\\b_3^0\cdot e^{\lambda_3 z}\end{pmatrix} \tag{A.7}$$

The solution vector $\vec{a}$ can be calculated from $\vec{b}$ using $\vec{a}=S\cdot\vec{b}$ and $J=S^{-1}\cdot A\cdot S$. The result is

$$\frac{d}{dz}S\cdot\vec{b}=A\cdot S\cdot\vec{b} \tag{A.8}$$

which is equivalent to the first equation. Finally, we have to determine the free constants by inserting the starting conditions

$$a_i^0=a_i(z=0) \tag{A.9}$$

For the special simple case $\alpha = 1$, the final result is given in equations (3.12), (3.13) and (3.14). For the calculation of the intensities out of the amplitudes, we have to consider the squares of the complex amplitude components a_i.

A.1.2 Interferometer with parasitic reflection in sensing arm

If we have no parasitic reflection at the AR-coated facet of the device, we can calculate the dual beam interference between the electric fields

$$E_1=E_0r_0\cdot e^{i\delta}\ \text{and}\ E_2=E_0r\cdot e^{i\phi} \tag{A.10}$$

simply by adding the field amplitudes and taking the square of the absolute value; this is done in the equation

$$I(\delta)=I_{cross}+|E_1+E_2|^2 \tag{A.11}$$

and results in

$$I(\delta) = I_{cross} + I_0\left[r_0^2 + r^2 + \frac{2r_0 r}{r_0^2 + r^2}\cdot\cos(\delta - \phi)\right] \qquad (A.12)$$

I_{cross} is the crosstalk intensity, r_0 the reference mirror reflectivity and r the object mirror reflectivity. Considering the parasitic FP-cavity, formula (A.12) turns in a rather complicated expression.

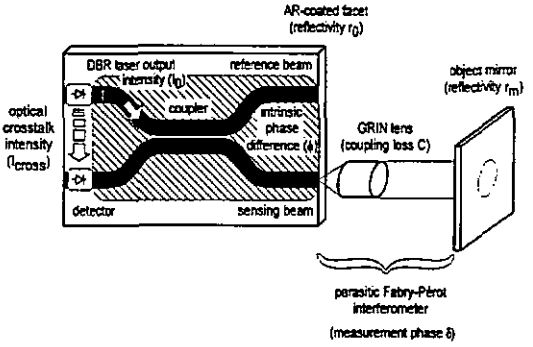

Fig. A.1 - Single Michelson interferometer chip with all external elements and simulated parameters

The following notations and equations have been used in (A.10) to (A.12): $\delta = 4\pi dn/\lambda$ is the measurement phase, C the GRIN lens coupling loss per pass, ϕ the intrinsic phase difference, I_{cross} the crosstalk intensity and I_0 the DBR laser output. For the calculation of the more complicated case with a parasitic FP-interferometer in the sensing arm, we start with the electric field in the FP-cavity. Here the reflection on an interface semiconductor-air causes an additional phase shift of π; therefore the reflectivity r_0 has an additional factor (-1). If we insert the electric fields

$$E_2 = -E_0 r\cdot e^{i\phi} \text{ and } E_2 = E_0\cdot\frac{-r_0 + r\cdot e^{i\delta}}{1 - r_0 r\cdot e^{i\delta}} \qquad (A.13)$$

into equation (A.11), we can calculate the total interference signal of an interferometer with parasitic FP-cavity:

$$I(\delta) = I_{cross} + I_0\left[\begin{array}{l} r_0^2 + \dfrac{(r_0 - Cr)^2 + 4Cr_0 r\sin^2\left(\frac{\delta}{2}\right)}{(1 - Cr_0 r)^2 + 4Cr_0 r\sin^2\left(\frac{\delta}{2}\right)} + \ldots \\ \ldots + 2\dfrac{r_0^2(1 + r_0^2)\cos\phi - Cr_0 r\left(r_0^2\cos(\delta + \phi) + \cos(\delta - \phi)\right)}{(1 - Cr_0 r)^2 + 4Cr_0 r\sin^2\left(\frac{\delta}{2}\right)} \end{array}\right] \qquad (A.14)$$

In figure 3.13, we already presented the calculated interference signals for four different mirror reflectances r^2.

A.2 SPECIAL PROCESS STEPS

A.2.1 Waveguide dry etching

All waveguides used for these interferometers were fabricated with the same dry etch process. Processing started with the spinning of a 1.3 µm thick photoresist layer (Shipley S1813, 4000 min^{-1}). The photolithography step using the waveguide mask produced then 3 µm wide photoresist stripes. These structures were postbaked in a convection oven at 130 °C in order to allow a reflow of the photoresist and to achieve very smooth sidewalls [85]. The dry etching was performed by magnetic field-enhanced reactive ion etching (MERIE) using 2 sccm $SiCl_4$ at 0.2 mTorr pressure, 200 W rf power, and -110 V dc bias [86]. These conditions gave best results in terms of waveguide scattering loss and steepness of the sidewalls. For our weakly index-guided structures, we etched the waveguides to a depth of 100 nm above the waveguide core (see figure 2.2).

A.2.2 Metals

The patterning of the p-metal layers was carried out by a lift-off process using Hoechst AZ 5214 image reversal photoresist. This resist required a process which started with spinning at 4000 min^{-1} and following postbake at 120 °C for 1 min. After 7 s exposure of the clear field p-metal mask, we had to make a hardbake at 120 °C for 2 min in order to stabilize the resist in the exposed areas. The following 14 s flood exposure un-crosslinked the unexposed areas, and the subsequent development (Shipley MF-319) removed the un-crosslinked photoresist; the generated undercut profile with an overhang of 0.5 nm was ideal for p-metal lift-off. We measured this overhang approximately in the SEM.

A.3 FULL PROCESS DESCRIPTIONS

In this last section, we give the detailed process sheets for the broad area lasers, the Fabry-Pérot lasers, the DBR lasers, and the whole interferometers.

A.3.1 Broad area laser process

MASKS	
Layer identification	Description
SL	Slit-mask with 50 μm slits for p-metal evaporation

STEP 1 - STANDARD SOLVENT CLEAN		
Step	Process	Parameters
1.1	Trichloroethylene Acetone Isopropanol	2:00, 25 °C / 1:00 ultrasound 2:00, 25 °C / 1:00 ultrasound 2:00, 25 °C / 1:00 ultrasound
1.2	DI rinse	1:00; N_2 dry
1.3	Inspection	Random dirt, filth and rubbish

STEP 2 - P-METALIZATION		
2.1	Dehydration	180 °C, 30:00, oven
2.2	Mounting into vacuum holder	Each piece covers at least one hole
2.3	Deposition	Ti/Pt/Au 80/120/100 nm
2.4	Inspection	Random dirt, filth and rubbish

STEP 3 - WAFER THINNING		
3.1	Wafer fix	Wax on hot glass substrate
3.2	Thinning	Thickness: 100 μm, grit size 5 μm
3.3	Release wafer	Trichloroethylene 10:00, 50 °C
3.4	DI rinse	1:00; N_2 dry
3.5	Inspection	PR remnants, alignment

STEP 4 - STANDARD SOLVENT CLEAN		
4.1	Trichloroethylene Acetone Isopropanol	2:00, 25 °C / 1:00 ultrasound 2:00, 25 °C / 1:00 ultrasound 2:00, 25 °C / 1:00 ultrasound
4.2	DI rinse	1:00; N_2 dry
4.3	Inspection	Random dirt, filth and rubbish

STEP 5 - ETCH WITH PHOSPHORIC ACID		
5.1	Stress removal	H_3PO_4/HCl 3:1, 1:30, soft soaking
5.2	Inspection	Random dirt, filth and rubbish

STEP 6 - N-METAL DEPOSITION AND ANNEAL		
6.1	Deposition	Ge/Au/Ni/Au 30/47/30/100 nm
6.2	Anneal	RTA oven, 435 °C, 1:00 (Cantilever T-sensor)
6.3	Inspection	Surface morphology

STEP 7 - CAP ETCH		
7.1	Cap etch	$C_6H_8O_7/H_2O_2$ 6:1, 2:00
7.2	Inspection	Random dirt, filth and rubbish

STEP 8 - SCRATCH AND CLEAVE		
8.1	Scratches	Diamond scratcher, d = 500 μm
8.2	Cleaving	Cleave machine
8.3	Inspection	Surface of cleaved facets

A.3.2 Fabry-Pérot laser process

MASKS	
Layer identification	**Description**
EBR	Edge bead removal
WG	Waveguide
CON	Contact hole
PM	P-metal

STEP 1 - STANDARD SOLVENT CLEAN		
Step	**Process**	**Parameters**
1.1	Trichloroethylene Acetone Isopropanol	2:00, 25 °C / 1:00 ultrasound 2:00, 25 °C / 1:00 ultrasound 2:00, 25 °C / 1:00 ultrasound
1.2	DI rinse	1:00; N_2 dry
1.3	Inspection	Random dirt, filth and rubbish

STEP 2 - PHOTOLITHOGRAPHY (WAVEGUIDES)		
2.1	Dehydration	180 °C, 30:00, oven
2.2	Photoresist	Microposit S 1800-13, spin: 4000 rpm, 0:30
2.3	Softbake	115 °C, 0:45, hotplate
2.4	Edge bead removal	Exposure: EBR mask, 0:50 Development: Microposit MF-319, 1:20
2.5	Exposure	WG mask (clear field), 0:06
2.6	Development	Microposit MF-319, 0:40
2.7	De-scum	O_2 plasma, 300 mTorr, 50 W, 2:00
2.8	Inspection	PR remnants, alignment

STEP 3 - WAVEGUIDE RIDGE ETCH		
3.1	Hardbake	130 °C, 30:00, oven
3.2	Etch	Magnetron RIE: 2 sccm $SiCl_4$ 0.2 mTorr, 200 W, 110 V, 10 °C Etch rate: 45 nm/min Depth: 900 nm, Time: 20:00
3.3	Inspection	Surface debris, redeposition
3.4	Characterization	Etch depth (Dektak), profile (SEM)

STEP 4 - PHOTORESIST STRIP		
4.1	Plasma soften	O_2, 700 mTorr, 300 W, 15:00
4.2	Microposit remover 1165 (2 beakers)	Beaker 1: 80 °C, 10:00 ultrasound Beaker 2: 80 °C, 10:00 ultrasound
4.3	Isopropanol rinse	2:00, 25 °C / 1:00 ultrasound
4.4	*DI rinse*	1:00; N_2 dry
4.5	Plasma clean	O_2, 700 mTorr, 300 W, 15:00
4.6	Inspection	PR remnants, random filth

STEP 5 - SI_3N_4 DEPOSITION		
5.1	Deposition	PECVD: 250 sccm N_2 3 sccm NH_3 93 sccm SiH_4 600 mTorr, 10 W, 300 °C, thickness: 250 nm
5.2	Inspection	Uniformity
5.3	Characterization	Ellipsometer: thickness, refractive index

STEP 6 - PHOTOLITHOGRAPHY (CONTACT HOLE)		
6.1	Photoresist	Microposit S 1800-13, spin: 4000 rpm, 0:30
6.2	Softbake	115 °C, 0:45, hotplate
6.3	Edge bead removal	Exposure: EBR mask, 0:50 Development: Microposit MF-319, 1:20
6.4	Exposure	CON mask (dark field), 0:06
6.5	Development	Microposit MF-319, 0:40
6.6	De-scum	O_2 plasma, 300 mTorr, 50 W, 2:00
6.7	Inspection	PR remnants, alignment

STEP 7 - CONTACT HOLE (SI_3N_4) ETCH		
7.1	Inspection	Contact hole
7.2	Etch	RIE: 50 sccm CF_4, 50 mTorr, 100 W, 300 V, 5:00
7.3	Damage remove	b-HF, 25 °C, 0:05

STEP 8 - PHOTORESIST STRIP		
8.1	Plasma soften	O_2, 700 mTorr, 300 W, 15:00
8.2	Microposit remover 1165 (2 beakers)	Beaker 1: 80 °C, 10:00 ultrasound Beaker 2: 80 °C, 10:00 ultrasound
8.3	Isopropanol rinse	2:00, 25 °C / 1:00 ultrasound
8.4	DI rinse	1:00; N_2 dry
8.5	Plasma clean	O_2, 700 mTorr, 300 W, 15:00
8.6	Inspection	PR remnants, random filth

STEP 9 - PHOTOLITHOGRAPHY (P-METALIZATION)		
9.1	Dehydration	180 °C, 30:00, oven
9.2	Photoresist	Hoechst AZ 5214, spin: 4000 rpm, 0:30
9.3	Postbake	Hotplate: 120 °C, 1:00
9.4	Edge bead removal	Exposure: EBR mask 1:00 Development: Microposit MF-319, 1:00
9.5	Exposure	PM mask (clear field), 0:07
9.6	Hardbake	120 °C, 2:00
9.7	Flood exposure	Without mask: 0:14
9.8	Development	Microposit MF-319 (without soaking), 2:00
9.9	De-scum	O_2 plasma, 300 mTorr, 50 W, 2:00
9.10	Inspection	PR remnants, alignment

STEP 10 - P-METAL DEPOSITION AND LIFTOFF		
10.1	Contact wash	HCl/H_20 1:5, 9 °C, 1:00
10.2	Deposition	Ti/Pt/Au 80/120/200 nm
10.3	Liftoff	Acetone, 15:00, 25 °C / 0:30 ultrasound
10.4	Inspection	Surface morphology

STEP 11 - STANDARD SOLVENT CLEAN		
11.1	Trichloroethylene Acetone Isopropanol	2:00, 25 °C / 1:00 ultrasound 2:00, 25 °C / 1:00 ultrasound 2:00, 25 °C / 1:00 ultrasound
11.2	DI rinse	1:00; N_2 dry
11.3	Inspection	Random dirt, filth and rubbish

STEP 12 - WAFER THINNING		
12.1	Wafer fix	Wax on hot glass substrate
12.2	Thinning	Thickness: 100 µm, grit size 3 µm
12.3	Polish	Al_2O_3 slurry (fine)
12.4	Release wafer	Trichloroethylene 10:00, 50 °C
12.5	DI rinse	1:00; N_2 dry
12.6	Inspection	Random dirt, filth and rubbish

STEP 13 - N-METAL DEPOSITION AND ANNEAL		
13.1	Deposition	Ge/Au/Ni/Au (30/47/30/100 nm)
13.2	Anneal	RTA oven, 435 °C, 1:00 (cantilever T-sensor)
13.3	Inspection	Surface morphology

STEP 14 - SCRATCH AND CLEAVE		
14.1	Scratches	Diamond scratcher, d = 500 µm
14.2	Cleaving	Cleave machine
14.3	Inspection	Surface of cleaved facets

A.3.3 DBR laser process

MASKS	
Layer identification	**Description**
EBR	Edge bead removal
WG	Waveguide
CON	Contact hole
PM	P-metal
GRA	Grating recess

STEP 1 - STANDARD SOLVENT CLEAN		
Step	**Process**	**Parameters**
1.1	Trichloroethylene Acetone Isopropanol	2:00, 25 °C / 1:00 ultrasound 2:00, 25 °C / 1:00 ultrasound 2:00, 25 °C / 1:00 ultrasound
1.2	DI rinse	1:00; N_2 dry
1.3	Inspection	Random dirt, filth and rubbish

STEP 2 - PHOTOLITHOGRAPHY (WAVEGUIDES)		
2.1	Dehydration	180 °C, 30:00, oven
2.2	Photoresist	Microposit S 1800-13, spin: 4000 rpm, 0:30
2.3	Softbake	115 °C, 0:45, hotplate
2.4	Edge bead removal	Exposure: EBR mask, 0:50 Development: Microposit MF-319, 1:20
2.5	Exposure	WG mask (clear field), 0:06
2.6	Development	Microposit MF-319, 0:40
2.7	De-scum	O_2 plasma, 300 mTorr, 50 W, 2:00
2.8	Inspection	PR remnants, alignment

STEP 3 - WAVEGUIDE RIDGE ETCH		
3.1	Hardbake	130 °C, 30:00, oven
3.2	Etch	Magnetron RIE: 2 sccm $SiCl_4$ 0.2 mTorr, 200 W, 110 V, 10 °C Etch rate: 45 nm/min Depth: 900 nm, Time: 20:00
3.3	Inspection	Surface debris, redeposition
3.4	Characterization	Etch depth (Dektak), profile (SEM)

STEP 4 - PHOTORESIST STRIP		
4.1	Plasma soften	O_2, 700 mTorr, 300 W, 15:00
4.2	Microposit remover 1165 (2 beakers)	Beaker 1: 80 °C, 10:00 ultrasound Beaker 2: 80 °C, 10:00 ultrasound
4.3	Isopropanol rinse	2:00, 25 °C / 1:00 ultrasound
4.4	DI rinse	1:00; N_2 dry
4.5	Plasma clean	O_2, 700 mTorr, 300 W, 15:00
4.6	Inspection	PR remnants, random filth

STEP 5 - SI_3N_4 DEPOSITION		
5.1	Deposition	PECVD: 250 sccm N_2 3 sccm NH_3 93 sccm SiH_4 600 mTorr, 10 W, 300 °C, thickness: 250 nm
5.2	Inspection	Uniformity
5.3	Characterization	Ellipsometer: thickness, refractive index

STEP 6 - PHOTOLITHOGRAPHY (CONTACT HOLE)		
6.1	Photoresist	Microposit S 1800-13, spin: 4000 rpm, 0:30
6.2	Softbake	115 °C, 0:45, hotplate
6.3	Edge bead removal	Exposure: EBR mask, 0:50 Development: Microposit MF-319, 1:20
6.4	Exposure	CON mask (dark field), 0:06
6.5	Development	Microposit MF-319, 0:40
6.6	De-scum	O_2 plasma, 300 mTorr, 50 W, 2:00
6.7	Inspection	PR remnants, alignment

STEP 7 - CONTACT HOLE (SI_3N_4) ETCH		
7.1	Inspection	Contact hole
7.2	Etch	RIE: 50 sccm CF_4, 50 mTorr, 100 W, 300 V, 5:00
7.3	Damage remove	b-HF, 25 °C, 0:05

STEP 8 - PHOTORESIST STRIP		
8.1	Plasma soften	O_2, 700 mTorr, 300 W, 15:00
8.2	Microposit remover 1165 (2 beakers)	Beaker 1: 80 °C, 10:00 ultrasound Beaker 2: 80 °C, 10:00 ultrasound
8.3	Isopropanol rinse	2:00, 25 °C / 1:00 ultrasound
8.4	DI rinse	1:00; N_2 dry
8.5	Plasma clean	O_2, 700 mTorr, 300 W, 15:00
8.6	Inspection	PR remnants, random filth

STEP 9 - PHOTOLITHOGRAPHY (P-METALIZATION)		
9.1	Dehydration	180 °C, 30:00, oven
9.2	Photoresist	Hoechst AZ 5214, spin: 4000 rpm, 0:30
9.3	Postbake	Hotplate: 120 °C, 1:00
9.4	Edge bead removal	Exposure: EBR mask 1:00 Development: Microposit MF-319, 1:00
9.5	Exposure	PM mask (clear field), 0:07
9.6	Hardbake	120 °C, 2:00
9.7	Flood exposure	Without mask: 0:14
9.8	Development	Microposit MF-319 (without soaking), 2:00
9.9	De-scum	O_2 plasma, 300 mTorr, 50 W, 2:00
9.10	Inspection	PR remnants, alignment

STEP 10 - P-METAL DEPOSITION AND LIFTOFF		
10.1	Contact wash	HCl/H_20 1:5, 9 °C, 1:00
10.2	Deposition	Ti/Pt/Au 80/120/200 nm
10.3	Liftoff	Acetone, 15:00, 25 °C / 0:30 ultrasound
10.4	Inspection	Surface morphology

STEP 11 - STANDARD SOLVENT CLEAN		
11.1	Trichloroethylene Acetone Isopropanol	2:00, 25 °C / 1:00 ultrasound 2:00, 25 °C / 1:00 ultrasound 2:00, 25 °C / 1:00 ultrasound
11.2	DI rinse	1:00; N_2 dry
11.3	Inspection	Random dirt, filth and rubbish

STEP 12 - PHOTOLITHOGRAPHY (GRATING RECESS)		
12.1	Photoresist	Microposit S 1800-13, spin: 4000 rpm, 0:30
12.2	Softbake	115 °C, 0:45, hotplate
12.3	Edge bead removal	Exposure: EBR mask, 0:50 Development: Microposit MF-319, 1:20
12.4	Exposure	GRA mask (dark field), 0:06
12.5	Development	Microposit MF-319, 0:40
12.6	De-scum	O_2 plasma, 300 mTorr, 50 W, 2:00
12.7	Inspection	PR remnants, alignment

STEP 13 - GRATING RECESS ETCH		
13.1	Inspection	Grating recess window
13.2	Si_3N_4-etch	RIE: 50 sccm CF_4, 50 mTorr, 100 W, 300 V, 5:00
13.3	Etch	Magnetron RIE: 2 sccm $SiCl_4$ 0.2 mTorr, 200 W, 110 V, 10 °C Etch rate: 45 nm/min Depth: 770 nm, Time: 17:00

STEP 14 - PHOTORESIST STRIP		
14.1	Plasma soften	O_2, 700 mTorr, 300 W, 15:00
14.2	Microposit remover 1165 (2 beakers)	Beaker 1: 80 °C, 10:00 ultrasound Beaker 2: 80 °C, 10:00 ultrasound
14.3	Isopropanol rinse	2:00, 25 °C / 1:00 ultrasound
14.4	DI rinse	1:00; N_2 dry
14.5	Plasma clean	O_2, 700 mTorr, 300 W, 15:00
14.6	Inspection	PR remnants, random filth

STEP 15 - GRATING MASK FABRICATION		
15.1	Photoresist	Microposit S 1800-01.5, spin: 4000 rpm, 0:30
15.2	Softbake	115 °C, 0:45, hotplate
15.3	Inspection	Surface morphology, thickness uniformity
15.4	Holographic setup	Grating period: Λ = 380 nm
15.5	Exposure	HeCd-laser (λ = 441.6 nm), 5:00 (integrated)
15.6	Development	Microposit developer/H_2O 1:1, 0:30
15.7	Cr-evaporation	4 nm each side, 13 ° tilted to substrate plane
15.8	O_2-etch	RIE: 10 sccm O_2, 3 mTorr, 80 W, 490 V, 10:00
15.9	Inspection	Profile and depth (SEM)

STEP 16 - GRATING ETCH		
16.1	Etch	Magnetron RIE: 6 sccm $SiCl_4$ 1 mTorr, 200 W, 110 V, 10 °C Etch rate: 60 nm/min Depth: 160 nm, Time: 2:40
16.2	Plasma clean	O_2, 700 mTorr, 300 W, 30:00
16.3	Inspection	Profile, depth (SEM) and length (microscope)

STEP 17 - WAFER THINNING		
17.1	Wafer fix	Wax on hot glass substrate
17.2	Thinning	Thickness: 100 µm, grit size 3 µm
17.3	Polish	Al_2O_3 slurry (fine)
17.4	Release wafer	Trichloroethylene 10:00, 50 °C
17.5	DI rinse	1:00; N_2 dry
17.6	Inspection	Random dirt, filth and rubbish

STEP 18 - N-METAL DEPOSITION AND ANNEAL		
18.1	Deposition	Ge/Au/Ni/Au (30/47/30/100 nm)
18.2	Anneal	RTA oven, 435 °C, 1:00 (cantilever T-sensor)
18.3	Inspection	Surface morphology

STEP 19 - SCRATCH AND CLEAVE		
19.1	Scratches	Diamond scratcher, d = 500 μm
19.2	Cleaving	Cleave machine
19.3	Inspection	Surface of cleaved facets

A.3.4 Interferometer process

MASKS	
Layer identification	Description
EBR	Edge bead removal
DCA	Dielectric cap anneal
CAP	Cap etch
II	Ion implant
WG	Waveguide
TRE	Isolation trench
CON	Contact hole
PM	P-metal
GRA	Grating recess

STEP 1 - STANDARD SOLVENT CLEAN		
Step	Process	Parameters
1.1	Trichloroethylene Acetone Isopropanol	2:00, 25 °C / 1:00 ultrasound 2:00, 25 °C / 1:00 ultrasound 2:00, 25 °C / 1:00 ultrasound
1.2	DI rinse	1:00; N_2 dry
1.3	Inspection	Random dirt, filth and rubbish

STEP 2 - PHOTOLITHOGRAPHY (DIELECTRIC CAP ANNEAL)		
2.1	Dehydration	180 °C, 30:00, oven
2.2	SiO_2-evaporation	Thickness: 200 nm, r = 3 Å/s, $p_0 = 2x10^{-6}$ Torr
2.3	Photoresist	Microposit S 1800-13, spin: 4000 rpm, 0:30
2.4	Softbake	115 °C, 0:45, hotplate
2.5	Edge bead removal	Exposure: EBR mask, 0:50 Development: Microposit MF-319, 1:20
2.6	Exposure	DCA mask (dark field), 0:06
2.7	Development	Microposit MF-319, 0:40
2.8	De-scum	O_2 plasma, 300 mTorr, 50 W, 2:00
2.9	Inspection	PR remnants, alignment
2.10	Etch	RIE, 50 sccm, 50 mTorr, 100 W, 300 V, 5:00

STEP 3 - SRF_2-DEPOSITION AND LIFTOFF		
3.1	SrF_2-evaporation	Thickness: 300 nm, r = 5 Å/s, $p_0 = 5x10^{-6}$ Torr
3.2	Liftoff	Microposit remover 1165 2:00, 80 °C / 1:00 ultrasound
3.3	Isopropanol rinse	2:00, 25 °C / 1:00 ultrasound
3.4	Inspection	PR remnants, alignment

STEP 4 - DIELECTRIC CAP ANNEAL AND DIELECTRIC STRIP		
4.1	Rapid thermal anneal	960 °C, 40 secs, on GaAs proximity wafer (T-shaped temperature sensor)
4.2	SiO_2-etch	RIE, 50 sccm, 50 mTorr, 100 W, 300 V, 5:00
4.3	SrF_2-removal	HCl/H_2O 1:9, 0:20
4.4	Inspection	Surface damage, SiO_2/SrF_2-interface

STEP 5 - STANDARD SOLVENT CLEAN		
5.1	Trichloroethylene Acetone Isopropanol	2:00, 25 °C / 1:00 ultrasound 2:00, 25 °C / 1:00 ultrasound 2:00, 25 °C / 1:00 ultrasound
5.2	DI rinse	1:00; N_2 dry
5.3	Inspection	Random dirt, filth and rubbish

STEP 6 - PHOTOLITHOGRAPHY (CAP ETCH)		
6.1	Dehydration	180 °C, 30:00, oven
6.2	Photoresist	Microposit S 1800-13, spin: 4000 rpm, 0:30
6.3	Softbake	115 °C, 0:45, hotplate
6.4	Edge bead removal	Exposure: EBR mask, 0:50 Development: Microposit MF-319, 1:20
6.5	Exposure	CAP mask (clear field), 0:06
6.6	Development	Microposit MF-319, 0:40
6.7	Cap etch	$C_6H_8O_7/H_2O_2$ 6:1, 2:00
6.8	Inspection	Random dirt, filth and rubbish

STEP 7 - PHOTORESIST STRIP		
7.1	Plasma soften	O_2, 700 mTorr, 300 W, 15:00
7.2	Microposit remover 1165 (2 beakers)	Beaker 1: 80 °C, 10:00 ultrasound Beaker 2: 80 °C, 10:00 ultrasound
7.3	Isopropanol rinse	2:00, 25 °C / 1:00 ultrasound
7.4	DI rinse	1:00; N_2 dry
7.5	Plasma clean	O_2, 700 mTorr, 300 W, 15:00
7.6	Inspection	PR remnants, random filth

STEP 8 - PHOTOLITHOGRAPHY (ION IMPLANT)		
8.1	Dehydration	180 °C, 30:00, oven
8.2	Photoresist	Microposit S 1800-28, spin: 4000 rpm, 0:30
8.3	Softbake	115 °C, 0:45, hotplate
8.4	Edge bead removal	Exposure: EBR mask, 1:10 Development: Microposit MF-319, 1:30
8.5	Exposure	II mask (clear field), 0:10
8.6	Development	Microposit MF-319, 1:00
8.7	Hardbake	130 °C, 5:00, hotplate
8.8	Inspection	PR remnants, alignment, reflow

STEP 9 - ION IMPLANT AND PHOTORESIST STRIP		
9.1	Ship to NTB	Pack into black wafer boxes
9.2	Ion implant	H^+, 40 keV, $4x10^{15}$ cm^{-2}
9.3	Ion implant	H^+, 70 keV, $4x10^{15}$ cm^{-2}
9.4	Ion implant	H^+, 100 keV, $4x10^{15}$ cm^{-2}
9.5	Plasma clean	O_2, 700 mTorr, 300 W, 45:00
9.6	Inspection	PR remnants, random filth

STEP 10 - PHOTOLITHOGRAPHY (WAVEGUIDES)		
10.1	Dehydration	180 °C, 30:00, oven
10.2	Photoresist	Microposit S 1800-13, spin: 4000 rpm, 0:30
10.3	Softbake	115 °C, 0:45, hotplate
10.4	Edge bead removal	Exposure: EBR mask, 0:50 Development: Microposit MF-319, 1:20
10.5	Exposure	WG mask (clear field), 0:06
10.6	Development	Microposit MF-319, 0:40
10.7	De-scum	O_2 plasma, 300 mTorr, 50 W, 2:00
10.8	Inspection	PR remnants, alignment

STEP 11 - WAVEGUIDE RIDGE ETCH		
11.1	Hardbake	130 °C, 30:00, oven
11.2	Etch	Magnetron RIE: 2 sccm $SiCl_4$ 0.2 mTorr, 200 W, 110 V, 10 °C Etch rate: 45 nm/min Depth: 750 nm, Time: 16:40
11.3	Inspection	Surface debris, redeposition
11.4	Characterization	Etch depth (Dektak), profile (SEM)

STEP 12 - PHOTORESIST STRIP		
12.1	Plasma soften	O_2, 700 mTorr, 300 W, 15:00
12.2	Microposit Stripper 1165 (2 beakers)	Beaker 1: 80 °C, 10:00 ultrasound Beaker 2: 80 °C, 10:00 ultrasound
12.3	Isopropanol rinse	2:00, 25 °C / 1:00 ultrasound
12.4	DI rinse	1:00; N_2 dry
12.5	Plasma clean	O_2, 700 mTorr, 300 W, 15:00
12.6	Inspection	PR remnants, random filth

STEP 13 - PHOTOLITHOGRAPHY (TRENCH)		
13.1	Dehydration	180 °C, 30:00, oven
13.2	Photoresist	Microposit S 1800-13, spin: 4000 rpm, 0:30
13.3	Softbake	115 °C, 0:45, hotplate
13.4	Edge bead removal	Exposure: EBR mask, 0:50 Development: Microposit MF-319, 1:20
13.5	Exposure	TRE mask (dark field), 0:06
13.6	Development	Microposit MF-319, 0:40
13.7	De-scum	O_2 plasma, 300 mTorr, 50 W, 2:00
13.8	Inspection	PR remnants, alignment

STEP 14 - TRENCH ETCH		
14.1	Etch	Magnetron RIE: 2 sccm $SiCl_4$ 0.2 mTorr, 200 W, 110 V, 10 °C Etch rate: 45 nm/min Depth: 650 nm, Time: 14:30
14.2	Inspection	Surface debris, redeposition
14.3	Characterization	Etch depth (Dektak), profile (SEM)

STEP 15 - PHOTORESIST STRIP		
15.1	Plasma soften	O_2, 700 mTorr, 300 W, 15:00
15.2	Microposit remover 1165 (2 beakers)	Beaker 1: 80 °C, 10:00 ultrasound Beaker 2: 80 °C, 10:00 ultrasound
15.3	Isopropanol rinse	2:00, 25 °C / 1:00 ultrasound
15.4	DI rinse	1:00; N_2 dry
15.5	Plasma clean	O_2, 700 mTorr, 300 W, 15:00
15.6	Inspection	PR remnants, random filth

STEP 16 - SI_3N_4 DEPOSITION		
16.1	Deposition	PECVD: 250 sccm N_2 3 sccm NH_3 93 sccm SiH_4 600 mTorr, 10 W, 300 °C, thickness: 250 nm
16.2	Inspection	Uniformity
16.3	Characterization	Ellipsometer: thickness, refractive index

STEP 17 - PHOTOLITHOGRAPHY (CONTACT HOLE)		
17.1	Photoresist	Microposit S 1800-13, spin: 4000 rpm, 0:30
17.2	Softbake	115 °C, 0:45, hotplate
17.3	Edge bead removal	Exposure: EBR mask, 0:50 Development: Microposit MF-319, 1:20
17.4	Exposure	CON mask (dark field), 0:06
17.5	Development	Microposit MF-319, 0:40
17.6	De-scum	O_2 plasma, 300 mTorr, 50 W, 2:00
17.7	Inspection	PR remnants, alignment

STEP 18 - CONTACT HOLE (SI_3N_4) ETCH		
18.1	Inspection	Contact hole
18.2	Etch	RIE: 50 sccm CF_4, 50 mTorr, 100 W, 300 V, 5:00
18.3	Damage remove	b-HF, 25 °C, 0:05

STEP 19 - PHOTORESIST STRIP		
19.1	Plasma soften	O_2, 700 mTorr, 300 W, 15:00
19.2	Microposit remover 1165 (2 beakers)	Beaker 1: 80 °C, 10:00 ultrasound Beaker 2: 80 °C, 10:00 ultrasound
19.3	Isopropanol rinse	2:00, 25 °C / 1:00 ultrasound
19.4	DI rinse	1:00; N_2 dry
19.5	Plasma clean	O_2, 700 mTorr, 300 W, 15:00
19.6	Inspection	PR remnants, random filth

STEP 20 - PHOTOLITHOGRAPHY (P-METALIZATION)		
20.1	Dehydration	180 °C, 30:00, oven
20.2	Photoresist	Hoechst AZ 5214, spin: 4000 rpm, 0:30
20.3	Postbake	Hotplate: 120 °C, 1:00
20.4	Edge bead removal	Exposure: EBR mask 1:00 Development: Microposit MF-319, 1:00
20.5	Exposure	PM mask (clear field), 0:07
20.6	Hardbake	120 °C, 2:00
20.7	Flood exposure	Without mask: 0:14
20.8	Development	Microposit MF-319 (without soaking), 2:00
20.9	De-scum	O_2 plasma, 300 mTorr, 50 W, 2:00
20.10	Inspection	PR remnants, alignment

STEP 21 - P-METAL DEPOSITION AND LIFTOFF		
21.1	Contact wash	HCl/H_20 1:5, 9 °C, 1:00
21.2	Deposition	Ti/Pt/Au 80/120/200 nm
21.3	Liftoff	Acetone, 15:00, 25 °C / 0:30 ultrasound
21.4	Inspection	Surface morphology

STEP 22 - STANDARD SOLVENT CLEAN		
22.1	Trichloroethylene Acetone Isopropanol	2:00, 25 °C / 1:00 ultrasound 2:00, 25 °C / 1:00 ultrasound 2:00, 25 °C / 1:00 ultrasound
22.2	DI rinse	1:00; N_2 dry
22.3	Inspection	Random dirt, filth and rubbish

STEP 23 - PHOTOLITHOGRAPHY (GRATING RECESS)		
23.1	Photoresist	Microposit S 1800-13, spin: 4000 rpm, 0:30
23.2	Softbake	115 °C, 0:45, hotplate
23.3	Edge bead removal	Exposure: EBR mask, 0:50 Development: Microposit MF-319, 1:20
23.4	Exposure	GRA mask (dark field), 0:06
23.5	Development	Microposit MF-319, 0:40
23.6	De-scum	O_2 plasma, 300 mTorr, 50 W, 2:00
23.7	Inspection	PR remnants, alignment

STEP 24 - GRATING RECESS ETCH		
24.1	Inspection	Grating recess window
24.2	Si_3N_4-etch	RIE: 50 sccm CF_4, 50 mTorr, 100 W, 300 V, 5:00
24.3	Etch	Magnetron RIE: 2 sccm $SiCl_4$ 0.2 mTorr, 200 W, 110 V, 10 °C Etch rate: 45 nm/min Depth: 620 nm, Time: 14:00
24.4	Inspection	Ridge sidewalls in recess, redeposition

STEP 25 - PHOTORESIST STRIP		
25.1	Plasma soften	O_2, 700 mTorr, 300 W, 15:00
25.2	Microposit remover 1165 (2 beakers)	Beaker 1: 80 °C, 10:00 ultrasound Beaker 2: 80 °C, 10:00 ultrasound
25.3	Isopropanol rinse	2:00, 25 °C / 1:00 ultrasound
25.4	DI rinse	1:00; N_2 dry
25.5	Plasma clean	O_2, 700 mTorr, 300 W, 15:00
25.6	Inspection	PR remnants, random filth

STEP 26 - GRATING MASK FABRICATION		
26.1	Photoresist	Microposit S 1800-01.5, spin: 4000 rpm, 0:30
26.2	Softbake	115 °C, 0:45, hotplate
26.3	Inspection	Surface morphology, thickness uniformity
26.4	Holographic setup	Grating period: Λ = 380 nm
26.5	Exposure	HeCd-laser (λ = 441.6 nm), 5:00 (integrated)
26.6	Development	Microposit developer/H_2O 1:1, 0:30
26.7	Cr-evaporation	4 nm each side, 13 ° tilted to substrate plane
26.8	O_2-etch	RIE: 10 sccm O_2, 3 mTorr, 80 W, 490 V, 10:00
26.9	Inspection	Profile and depth (SEM)

STEP 27 - GRATING ETCH		
27.1	Etch	Magnetron RIE: 6 sccm $SiCl_4$ 1 mTorr, 200 W, 110 V, 10 °C Etch rate: 60 nm/min Depth: 160 nm, Time: 2:40
27.2	Plasma clean	O_2, 700 mTorr, 300 W, 30:00
27.3	Inspection	Profile, depth (SEM) and length (microscope)

STEP 28 - WAFER THINNING		
28.1	Wafer fix	Wax on hot glass substrate
28.2	Thinning	Thickness: 100 µm, grit size 3 µm
28.3	Polish	Al_2O_3 slurry (fine)
28.4	Release wafer	Trichloroethylene 10:00, 50 °C
28.5	DI rinse	1:00; N_2 dry
28.6	Inspection	Random dirt, filth and rubbish

STEP 29 - N-METAL DEPOSITION AND ANNEAL		
29.1	Deposition	Ge/Au/Ni/Au (30/47/30/100 nm)
29.2	Anneal	RTA oven, 435 °C, 1:00 (cantilever T-sensor)
29.3	Inspection	Surface morphology

STEP 30 - SCRATCH AND CLEAVE		
30.1	Scratches	Diamond scratcher, d = 500 µm
30.2	Cleaving	Cleave machine
30.3	Inspection	Surface of cleaved facets

STEP 31 - AR/HR-COATINGS		
31.1	Mount into holder	HR-coating side
31.2	SiO_2-evaporation	Thickness: 141 nm, r = 3 Å/s, $p_0 = 2x10^{-6}$ Torr
31.3	Al-evaporation	Thickness: 75 nm, r = 10 nm/s, $p_0 = 5x10^{-6}$ Torr
31.4	Mount into holder	AR-coating side
31.5	PASO III-evaporation	Thickness: 108 nm, r = 5 Å/s, $p_0 = 2x10^{-6}$ Torr
31.6	Inspection	Surface of coated facets

[84] A. Yariv, "Optical Electronics", Saunders College Publishing, 4th edition, pp. 519 - 529, 1991

[85] H.E.G. Arnot, H.P. Zappe, J.E. Epler, B. Graf, R. Widmer, and H.W. Lehmann, "Extremely smooth sidewalls for GaAs/AlGaAs ridge waveguides", *Electron. Lett.*, vol. 29, no. 12, pp. 496 - 497, 1993

[86] M. Meyyappan, G.F. McLane, H.S. Lee, D. Eckart, M. Namaroff, and J. Sasserath, "Magnetron reactive ion etching of GaAs in $SiCl_4$", *J. Vac. Sci. Technol.*, vol. B4, no. 3, pp. 1215 - 1217, 1992

APPENDIX B

B.1 ABSTRACTS OF PUBLICATIONS I - VII

Paper I

D. Hofstetter, H.P. Zappe, J.E. Epler, and J. Söchtig

Single-growth-step GaAs/AlGaAs distributed Bragg reflector lasers with holographically-defined recessed gratings

Electron. Lett., vol. 30, no. 22, pp. 1858 - 1859, 1994

A ridge waveguide GaAs/AlGaAs quantum well DBR laser, fabricated with a simplified grating recess-technology and a 3rd order grating is described. The reflector is fabricated on top of a recessed waveguide using holographic exposure followed by reactive ion etching. The laser operates on a single longitudinal and lateral mode with threshold current as low as 20 mA, output power 5 mW per facet and is intended for monolithically integrated interferometer applications.

Paper II

D. Hofstetter, H.P. Zappe, and J.E. Epler

Ridge waveguide DBR lasers with non-absorbing grating and transparent integrated waveguide

Electron. Lett., vol. 31, no. 12, pp. 980 - 982, 1995

A ridge waveguide GaAs/AlGaAs DBR laser with a non-absorbing grating section and a monolithically integrated transparent waveguide has been fabricated by the use of vacancy-enhanced quantum well disordering (VED). This technique allows the definition of absorbing and transparent regions, while requiring only a single growth step. No VED-enhanced degradation of laser quality was noted: optical output power was 5 mW from both the cleaved facet and grating reflector, threshold currents were 25 mA and slope efficiencies 0.2 W/A.

Paper III

D. Hofstetter, H.P. Zappe, J.E. Epler, and P. Riel

Monolithically integrated DBR laser, detector and transparent waveguide fabricated in a single growth step

IEEE Photon. Technol. Lett., vol. 7, no. 9, pp. 1022 - 1024, 1995

The monolithic integration of a GaAs/AlGaAs distributed Bragg reflector laser with a non-absorbing grating section, a transparent waveguide and an absorbing photodetector is reported. Transparent and absorbing segments were defined after growth by vacancy-enhanced quantum well disordering (VED). Laser output power was 4 mW with a threshold current of 22 mA. Detector current was linearly dependent on the laser output power and the emission from the grating side of the laser could be directly coupled into the detector. The conversion efficiency, defined as ratio between detector current and laser output power, was 0.47 A/W. Comparing as-grown, SiO_2-capped and SrF_2-capped devices, both lasers and detectors were not seen to be adversely affected by the anneal required for the VED.

Paper IV

D. Hofstetter, H.P. Zappe, J.E. Epler, and P.Riel

Multiple wavelength Fabry-Pérot lasers fabricated by vacancy-enhanced quantum well disordering

Appl. Phys. Lett., vol. 67, no. 14, pp. 1978 - 1980, 1995

Wavelength-shifted GaAs/AlGaAs Fabry-Pérot ridge waveguide lasers were fabricated by vacancy-enhanced quantum well disordering using dielectric cap annealing. 500 μm long and 4 μm wide Fabry-Pérot lasers with emission wavelengths selectively shifted by 20 nm were integrated with unshifted lasers on the same chip, characterized and further compared with lasers fabricated from as-grown material. These investigations showed that the absorption edge of a single-quantum well double-heterostructure can be selectively blue-shifted after epitaxial growth without compromising diode laser performance.

Paper V

D. Hofstetter, H.P. Zappe, and R. Dändliker

A monolithically integrated optical displacement sensor in GaAs/AlGaAs

Electron. Lett., vol. 31, no. 24, pp. 2121 - 2122, 1995

A monolithically integrated displacement sensor has been fabricated in the GaAs/AlGaAs material system. The device is configured as a Michelson interferometer and consists of a DBR laser, a directional coupler, transparent waveguides and a photodetector. Interference fringes could be seen at a measurement distance of up to 45 cm, requiring only the alignment of an external GRIN lens for beam collimation.

Paper VI

D. Hofstetter, H.P. Zappe, and R. Dändliker

A monolithically integrated double Michelson interferometer for optical displacement measurement with direction determination

IEEE Photon. Technol. Lett., vol. 8, no. 10, 1996

A monolithically integrated optical displacement sensor fabricated in the GaAs/AlGaAs material system is reported. The single-chip device consists of a distributed Bragg reflector laser, two photodetectors, two phase modulators, two Y-couplers, and two directional couplers. It is configured as a double Michelson interferometer and allows the determination of both magnitude and direction of a displacement. The detection of two 90° phase-shifted interferometer signals also resulted in an improved phase interpolation of $\phi/20$. Despite the relatively simple fabrication process, the integration of rather complex optical functions could be realized.

APPENDIX B

Paper VII

D. Hofstetter, H.P. Zappe, and R. Dändliker

Optical displacement measurement with GaAs/AlGaAs-based monolithically integrated Michelson interferometers

Submitted to *IEEE J. Lightwave Technol.*, August 22, 1996

Two monolithically integrated optical displacement sensors fabricated in the GaAs/AlGaAs material system are reported. These single chip microsystems are configured as Michelson interferometers and comprise a distributed Bragg reflector laser, photodetectors, phase shifters and waveguide couplers. While the use of a single Michelson interferometer allows measurement of displacement magnitude only, a double Michelson interferometer with two interferometer signals in phase quadrature also permits determination of movement direction. In addition, through the use of two 90° phase-shifted interferometer signals in the latter device, a phase interpolation of $\phi/20$ is possible, leading to a displacement resolution of 20 nm. The integration of these complex optical functions could be realized with a relatively simple fabrication process.

Paper I

Single-growth-step GaAs/AlGaAs distributed Bragg reflector lasers with holographically-defined recessed gratings

D. Hofstetter, H.P. Zappe, J.E. Epler and J. Söchtig

Indexing terms: Distributed Bragg reflector lasers, Holographic gratings

A ridge waveguide GaAs/AlGaAs quantum well DBR laser fabricated with a simplified grating recess-technology and a third order grating is described. The reflector is fabricated on top of a recessed waveguide using holographic exposure followed by reactive ion etching. The laser operates on a single longitudinal and lateral mode with threshold current as low as 20mA, output power 5mW per facet and is intended for monolithically integrated interferometer applications.

Introduction: Distributed Bragg reflector (DBR) lasers are attractive light sources due to their narrow linewidth, good frequency stability and large sidemode suppression [1]. In addition, they are suitable for monolithically integrated optical circuits, because at least one cleaved facet can be replaced by a waveguide grating. Fabrication of DBR lasers is typically rather involved: where electron-beam direct write is used for grating definition, throughput is limited by the serial nature of this process [2, 3]; if regrowth after grating etch is required, for the formation of an upper cladding or for contact purposes, demands on material growth are significant [3, 4]; finally, for non-regrown waveguides with a thick upper cladding, a deep grating etch is needed in order to achieve sufficient coupling. Recently, single growth step DBR lasers with an e-beam defined grating requiring a deep (1 μm) grating etch were reported [2].

We present in this Letter a single-growth-step DBR laser with a holographically defined grating fabricated in a recess etched into the upper cladding of the waveguide. This grating recess combines the advantages of a high coupling coefficient κ, resulting from the small buffer layer between waveguide core and grating, with a simplified grating etch process due to the small required etch depth. This relatively simple DBR laser fabrication procedure is fully compatible with a previously developed integrated optical interferometer process [5], making use of only two additional photolithography steps (dielectric patterning) and one additional etch step (grating etch).

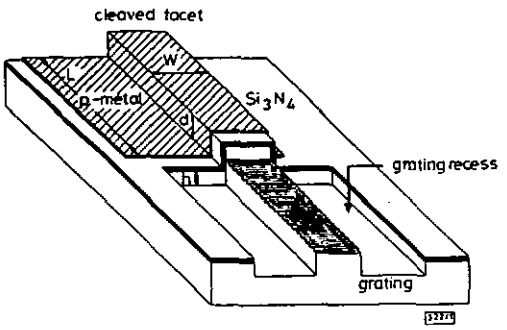

Fig. 1 *Schematic diagram of ridge waveguide DBR laser with grating recess*

Device fabrication: The laser layer structure was grown by MOCVD on an *n*-type, Si-doped ($10^{18}cm^{-3}$) GaAs wafer and consisted of an 1100nm *n*-doped ($1.5 \times 10^{18}cm^{-3}$ Si) $Al_{0.3}Ga_{0.7}As$ lower cladding, an undoped 180nm thick $Al_{0.3}Ga_{0.7}As$ waveguide core with one 8nm GaAs quantum well, a 780nm *p*-doped ($10^{18}cm^{-3}$ Be) $Al_{0.8}Ga_{0.2}As$ upper cladding and a highly *p*-doped ($8 \times 10^{18}cm^{-3}$ Zn) 160nm GaAs cap layer. Magnetic field enhanced reactive ion etching (MERIE) in an $SiCl_4$ plasma was used to dry etch a ridge waveguide to a depth of d = 800nm (see Fig. 1). A 300nm layer of plasma-enhanced chemical vapour deposited (PECVD) Si_3N_4 for electrical isolation of the surface allowed us to selectively contact the top of the ridge and also served as an etch mask for the subsequent grating recess etch. Nitride was removed from the contact hole and recess opening by dry etching using a CF_4 plasma.

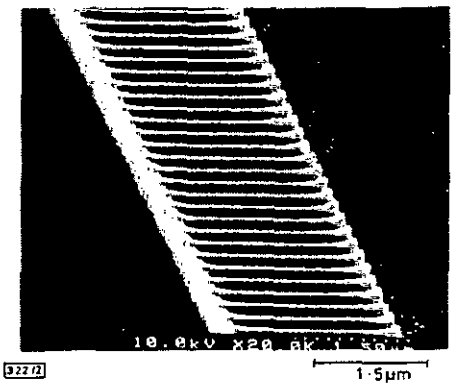

Fig. 2 *SEM photograph of portion of DBR (Λ = 385nm) on top of a 3μm waveguide*

Following *p*-metal evaporation (Ti/Pt/Au), the grating recess was etched into the upper cladding of the reflector section to a depth of h = 800nm by $SiCl_4$ MERIE, stopping 140nm above the $Al_{0.3}Ga_{0.7}As$ waveguide core. The device was then coated with a thin photoresist layer, leaving a thickness of 300nm on top of the recessed waveguide. Holographic exposure using an HeCd laser at 441.6nm, subsequent development and a soft-bake for resist sidewall smoothness improvement [6] yielded a suitable dry etch mask for the grating etch by MERIE. The rectangular third order grating with a unity line:space ratio was 140nm deep and had a period of 385nm (see Fig. 2). Wafer thinning to 200μm, *n*-metal contact (Ge/Au/Ni/Au) evaporation and cleaving to 1500μm length completed the process.

DBR lasers with mask ridge widths W = 3 and 5μm and with L = 480, 730 and 880μm long gain sections were fabricated. The unpumped Bragg reflector lengths were 1000, 500 and 200μm. For measurement comparisons, 1500μm long Fabry-Pérot lasers were also made on the same chip.

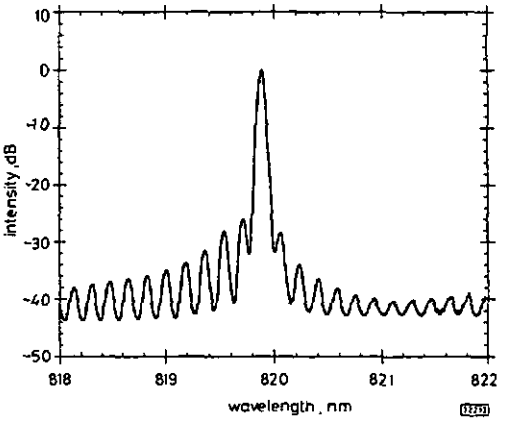

Fig. 3 *Optical spectrum of DBR laser at 2.3 I_{th}*

Results: Typical threshold currents of these simplified DBR lasers were I_{th} = 20mA, yielding J_{th} = 600A/cm² at an emission wavelength of 820nm; slope efficiency was 0.166W/A for emission from the cleaved facet. We compare this with Fabry-Pérot lasers which had I_{th} = 15mA, J_{th} = 450A/cm² at 833nm and an efficiency of

0.205W/A. A typical emission spectrum, measured with a high resolution grating spectrometer (0.64 m focal distance, 600 line per mm grating, 0.05nm resolution), at $I = 2.3\ I_{th}$ for the DBR lasers, driven CW at 300K, is shown in Fig. 3. The sidemode suppression ratio (SMSR) was 27dB and the main peak had a linewidth < 15MHz; measurement of the latter was equipment limited (scaning Fabry-Pérot Etalon, free spectral range = 2GHz, finesse = 150). The DBR devices had a temperature tuning coefficient of 0.7Å/K and operated in the same fundamental mode over a temperature range of more than 20K. The Fabry-Pérot lasers, on the other hand, had a temperature tuning coefficient of 2.5Å/K with mode hops every 3 to 5K.

The value of the SMSR is given by the coupling coefficient, $\kappa = 346cm^{-1}$, and the longitudinal mode spacing of 0.1732nm. We determined κ experimentally from the FWHM of the grating filter curve which could be determined approximately by measuring the laser spectrum at $0.96\ I_{th}$ [7]. Numerical modelling for this grating structure gave $\kappa = 392cm^{-1}$, calculated for a zero buffer layer thickness. This buffer layer is the remaining cladding layer between the top of the core and the bottom of the grating, and has been shown by simulation to strongly affect κ. Because this thickness is accurately controlled by the grating recess etch, we have a sensitive method for customising κ in this process.

The process compatibility with integrated optical sensor circuits permits this laser to act as a light source for interferometer circuits. The reduced demands on dry etching allow sensitive control of κ through variation of the recess etch depth thereby permitting easy optimisation of light intensity coupled into a following waveguide circuit.

Conclusions: Single growth step quantum well DBR lasers with a recessed grating mirror have been described. The third order grating, fabricated by holographic exposure and dry etching, appeared only on top of the recessed waveguide. A threshold current of 20mA, and a sidemode suppression ratio of 27dB were achieved when operated monomode at 820nm. The grating recess process allows easy customisation of κ, important for subsequent integration with optical integrated circuits.

Acknowledgments: The authors would like to thank H.P. Schweizer for crystal growth, H. Birbaumer and H. Schütz for tips on grating fabrication.

© IEE 1994
17 August 1994

Electronics Letters Online No: 19941262

D. Hofstetter, H.P. Zappe, J. E. Epler and J. Söchtig (*Paul Scherrer Institut Zürich; Badenerstrasse 569; CH-8048 Zürich, Switzerland*)

References

1 KOJIMA, K., and KYUMA, K.: 'Multi-quantum well distributed feedback and distributed Bragg reflector lasers', *Semicond. Sci. Technol.*, 1990, 5, pp. 481–493

2 MAJOR, J.S., O'BRIEN, S., GULGAZOV, V., WELCH, D.F., and LANG, R.J.: 'High-power singlemode AlGaAs distributed Bragg reflector laser diodes operating at 8.56nm', *Electron. Lett.*, 1994, 30, pp. 496–497

3 STOLTZ, B., DASLER, M., and SAHLEN, O.: 'Low threshold-current, wide tuning-range, butt-joint DBR laser grown with four MOVPE steps', *Electron. Lett.*, 1993, 29, pp. 700–702

4 SMITH, G.M., HUGHES, J.S., OSOWSKI, M.L., FORBES, D.V., and COLEMAN, J.J.: 'Ridge waveguide distributed Bragg reflector InGaAs/GaAs quantum well lasers', *Electron. Lett.*, 1994, 30, pp. 651–653

5 ZAPPE, H.P., ARNOT, H.E.G., and KUNZ, R.E.: 'Technology and devices for hybrid and monolithic integrated optical sensors', *Sensors and Actuators A*, 1994, 41, pp. 141–144

6 ARNOT, H.E.G., ZAPPE, H.P., EPLER, J.E., GRAF, B., WIDMER, R., and LEHMAN, H.W.: 'Extremely short sidewalls for GaAs/AlGaAs ridge waveguides', *Electron. Lett.*, 1993, 29, pp. 1131–1133

7 KOCH, T.L., and KOREN, U.: 'Semiconductor lasers for coherent optical fiber communications', *J. Lightwave Technol.*, 1990, LT-8, pp. 274–293

Paper II

Ridge waveguide DBR laser with nonabsorbing grating and transparent integrated waveguide

D. Hofstetter, H.P. Zappe and J.E. Epler

Indexing terms: Distributed Bragg reflector lasers, Semiconductor quantum wells

A ridge waveguide GaAs/AlGaAs DBR laser with a nonabsorbing grating section and a monolithically integrated transparent waveguide has been fabricated by the use of vacancy-enhanced quantum well disordering (VED). This technique allows the definition of absorbing and transparent regions, and requires only a single growth step. No VED-enhanced degradation of the laser quality was noted. The optical output power was 5 mW from both the cleaved facet and the grating reflector, threshold currents were 25 mA and the slope efficiencies were 0.2 W/A.

Introduction: Monolithic photonic integrated circuits (PICs) often require coherent light sources without cleaved laser facets. Distributed Bragg reflector (DBR) lasers are ideally suited to this application. Furthermore, a method is needed to produce absorbing and nonabsorbing regions on the same substrate without degrading laser performance. Pumped laser sections and photodetectors need to absorb at the operating wavelength, whereas the waveguides and the grating section of the DBR laser must be transparent. DBR lasers with a transparent grating section fabricated by vacancy-enhanced disordering (VED) [1] and DBR lasers evanescently coupled with a transparent waveguide [2] have been reported. The first of these approaches demonstrated that the VED process can shift the energy bandgap, albeit at the cost of a very high laser threshold current, whereas the latter required extended regrowth technology.

In this Letter, we demonstrate the use of the VED process to fabricate a low threshold DBR laser with a nonabsorbing grating section, monolithically integrated with a 700μm long transparent waveguide. The device demonstrates the utility of postgrowth processing for achieving spatially-defined transparency in a PIC. VED selectively alters the shape of the quantum well (QW) in the active region, using lift-off patterned SrF_2 and SiO_2 surface dielectrics to define the transparent and absorbing regions and a high temperature rapid thermal anneal to accomplish disordering [3].

Device fabrication: An MOVPE layer structure grown on an *n*-type, Si-doped, ($10^{18}cm^{-3}$) GaAs substrate was used to fabricate the device. An undoped 165nm thick $Al_{0.3}Ga_{0.7}As$ core containing a single 7nm wide GaAs quantum well was grown between a 1.1μm thick $Al_{0.3}Ga_{0.7}As$ lower cladding layer (*n*-doped $1.5 \times 10^{18}cm^{-3}$ Si) and a 0.8μm thick $Al_{0.3}Ga_{0.7}As$ upper cladding layer (*p*-doped $10^{18}cm^{-3}$ Mg). The upper cladding was covered with a 100 nm thick highly *p*-doped ($8 \times 10^{18}cm^{-3}$Zn) GaAs cap layer. The VED process started with a 200 nm thick e-beam evaporated SiO_2 layer, patterned by standard pbotolithography and reactive ion etching (RIE) in a CF_4 plasma. Using a selfaligned process, a 250nm thick SrF_2 layer was subsequently evaporated, and removed from the underlying SiO_2 by liftoff. The final wafer surface was nearly planar and completely covered with either SiO_2 or SrF_2. The selective bandgap-shift was then accomplished using a rapid thermal anneal in an N_2 ambient at 960°C for 24s.

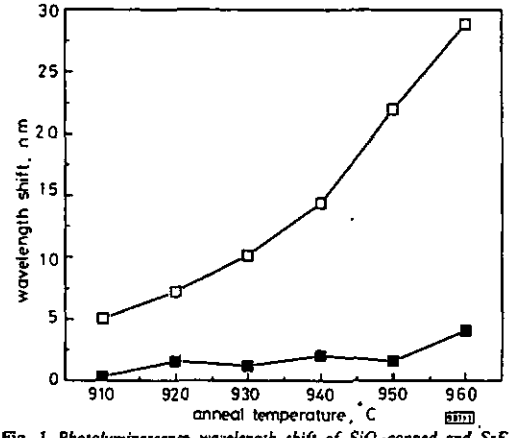

Fig. 1 *Photoluminescence wavelength shift of SiO_2-capped and SrF_2 capped material after 30s rapid thermal anneal at various temperatures*

During thermal annealing, the group-III vacancies generated under the SiO_2-capped regions diffuse through the upper cladding into the waveguide core. These vacancies promote intermixing of the Ga in the GaAs QW and the Al of the adjacent $Al_{0.3}Ga_{0.7}As$ waveguide core, increasing the effective Al content of the QW. The resulting larger bandgap blue-shifts the photoluminescence (PL) spectrum and thus the lasing wavelength. SrF_2, on the other hand, suppresses the generation of these group-III vacancies and no blue shift occurs during thermal annealing. As seen in Fig. 1, the amount of blue shift under the SiO_2 cap can be varied between 5 and 28nm with the annal temperature, while on the same wafer under the same anneal conditions, the blue shift under the SrF_2 cap is only 1 – 5nm. The anneal time is held constant at 30s in both cases. During RTA, a GaAs proximity cap prevents surface damage of the sample due to As outdiffusion [4].

After RTA, SrF_2 and SiO_2 were removed with diluted HCl (HCl/H_2O 1:9, 20s) and by RIE in CF_4, respectively. Lasers were then fabricated by dry etching ridge waveguides, deposition of 250nm Si_3N_4 as an electrical isolation layer and Ti/Pt/Au *p*-contact metallisation. The holographically-defined third-order grating (Λ = 380nm) was fabricated in a grating recess as described in [5]. DBR lasers with ridge widths of 2,3 and 4μm, a constant pumped length of 500μm and six different grating section lengths (50 to 150μm) were made and comparatively characterised. The lasers and gratings were integrated with a 700μm long transparent waveguide.

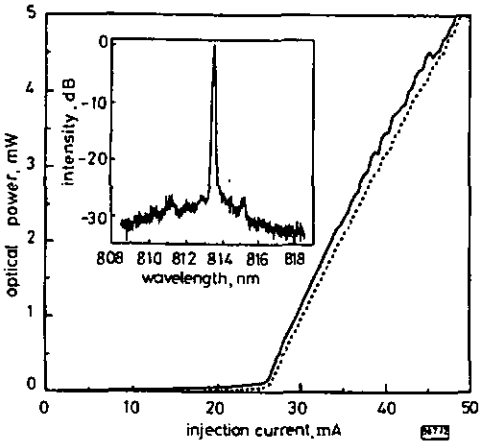

Fig. 2 *L-I curves of emission from the cleaved facet and the grating plus the transparent waveguide*

——— P_{opt} (cleaved facet)
- - - - P_{opt} (grating side facet)
Inset: optical spectrum

Results: As seen in Fig. 2, DBR laser threshold currents were typically 25mA on devices witha 4μm stripe width and a 500μm pumped length, corresponding to a threshold current density of 1.25kA/cm². The ripples in the L-I curve for optical output from the cleaved facet are reproducible and without hysteresis when increasing and decreasing the injection current. They indicate that the laser has to optimise its internal stored energy under changing phase conditions due to carrier and temperature induced refractive index changes. The ripples in the L-I curve were less pronounced for emission from the grating side of the laser than from the cleaved facet. We believe that this results from a trade-off between the grating transmission and the internal laser stored energy. A decrease in grating reflectivity induces a simultaneous decrease of the internal power and since the output power is the product of internal power and mirror transmission, nearly constant laser output power is expected.

The optical output power was 5mW from both the cleaved facet and the grating side of the DBR laser at $I = 2I_{th}$ and the slope efficiencies were 0.21W/A at the cleaved facet and 0.19W/A at the grating. This balance is due to the low grating reflectivity (< 30%) and the transparency of the waveguide. The optical emission spectrum, shown in the inset of Fig. 2, shows a primary emission peak at λ = 814nm and an SMSR of 25dB. No mode hops were seen as the temperature was varied from 7 to 25°C; the temperature tuning coefficient was 0.05nm/°C.

A comparison of Fabry-Perot lasers fabricated from the annealed but unshifted (SrF_2 capped) and as-grown (unannealed) material provided a further demonstration that high-quality lasers can be fabricated using VED. The former devices operated with a threshold current of 14mA (J_{th} = 700A/cm²), slope efficiency of 0.36W/A per facet at an emission wavelength of λ = 825nm with *SMSR* = 20dB. In as-grown material, the same laser structures yielded a threshold current of 12mA (J_{th} = 600A/cm²) and a slope efficiency of 0.52W/A per facet at an emission wavelength of λ = 827nm with *SMSR* = 20dB, demonstrating that devices produced in high temperature annealed material are of comparable quality to those produced in as-grown material. In contrast to results published in [6], we could not see any dopant diffusion or a drift of the *pn*-junction by inspecting the stained facet in the scanning electron microscope. These data also helped to explain the somewhat high threshold current density of the DBR lasers, owing to the mismatch between the Bragg peak of the grating (814nm) and the laser gain peak (825nm).

Conclusions: Low threshold DBR lasers monolithically integrated with a transparent waveguide have been fabricated using selective vacancy-enhanced disordering. The performance of the laser was not adversely affected by the high temperature anneal required for VED, demonstrating the utility of this process for PIC fabrication.

Acknowledgments: The authors are grateful to M. Moser and H.P. Schweizer for crystal growth, P. Riel, A. Vonlanthen and D. Jeggle for processing assistance, J. Söchtig for helpful discussions and H.W. Lehmann, M.T. Gale and R. Dändliker (IMT, University of Neuchâtel) for their generous support.

© IEE 1995
18 April 1995
Electronics Letters Online No: 19950643

D. Hofstetter, H.P. Zappe and J.E. Epler (*Paul Scherrer Institut Zürich, Badenerstrasse 569, CH-8048 Zürich, Switzerland*)

References

1 AYLING, S.G., BEAUVAIS, J., and MARSH, J.H.: 'A DBR laser using dielectric cap disordering and strontium fluoride masking', *Proc. ECIO*, 1993, 1993, pp. 7-10–7-11

2 DERI, R.J., DOLDISSEN, W., HAWKINS, R.J., BHAT, R., SOOLE, J.B.D., SCHIAVONE, L.M., SETO, M., ANDREADAKIS, N., SILBERBERG, Y., and KOZA, M.A.: 'Efficient vertical coupling of photodiodes to InGaAsP rib waveguides', *Appl. Phys. Lett.*, 1991, 71, pp. 2749–2751

3 BEAUVAIS, J., MARSH, J.H., KEAN, A.H., BRYCE, A.C., and BUTTON, C.: 'Suppression of bandgap shifts in GaAs/AlGaAs quantum wells using strontium fluoride caps', *Electron. Lett.*, 1992, 28, pp. 1670–1672

4 GUIDO, L.J., HOLONYAK, N., HSIEH, K.C., KALISKI, R.W., PLANO, W.E., BURNHAM, R.D., THORNTON, R.L., EPLER, J.E., and PAOLI, T.L.: 'Effects of dielectric encapsulation and As overpressure on Al-Ga interdiffusion in $Al_xGa_{1-x}As$/GaAs quantum well heterostructures', *J. Appl. Phys.*, 1987, 61, pp. 1372–1379

5 HOFSTETTER, D., ZAPPE, H.P., EPLER, J.E., and SÖCHTIG, J.: 'Single-growth-step GaAs/AlGaAs distributed Bragg-reflector lasers with holographically-defined recessed gratings', *Electron. Lett.*, 1994, 30, pp. 1858–1859

6 AYLING, S.G., BRYCE, A.C., GONTIJO, I., MARSH, J.H., and ROBERTS, J.S.: 'A comparison of carbon and zinc doping in GaAs/AlGaAs lasers band-gap tuned by impurity-free vacancy disordering', *Semicond. Sci. Technol.*, 1994, 9, pp. 2149–2151

Paper III

Monolithically Integrated DBR Laser, Detector, and Transparent Waveguide Fabricated in a Single Growth Step

D. Hofstetter, H. P. Zappe, J. E. Epler, *Member, IEEE*, and P. Riel

Abstract—**The monolithic integration of a GaAs–AlGaAs distributed Bragg reflector (DBR) laser with a nonabsorbing grating section, a transparent waveguide, and an absorbing photodetector is reported. Transparent and absorbing segments were defined after growth by vacancy-enhanced quantum-well disordering (VED). Laser output power was 5 mW with a threshold current of 22 mA. Detector current was linearly dependent on the laser output power and the emission from the grating side of the laser could be directly coupled into the detector. The conversion efficiency, defined as the ratio between detector current and laser output power, was 0.47 A/W. Using a comparison with as-grown, SiO_2-capped and SrF_2-capped devices, both lasers and detectors were not seen to be adversely affected by the anneal required for the VED.**

I. Introduction

SEMICONDUCTOR integrated optics offers the potential for small optical systems that may be mass produced. Monolithic integration of the laser into a photonic integrated circuit (PIC) reduces coupling losses and enhances robustness. However, a key problem in achieving integration is the definition of absorbing (lasers, detectors) and transparent (waveguides) regions. Numerous approaches, including evanescent coupling between waveguides and absorbing regions (requiring an additional impedance-matching layer and regrowth, respectively) [1], [2], butt coupling between laser and photodetector (needing mirror dry etch technique) [3] or the use of surface-emitting lasers and photodiodes (requiring high-quality dry-etched mirrors) [4], have been developed to address the integration issue.

We present in this letter a technique for the monolithic integration of a distributed Bragg reflector (DBR) laser with transparent waveguide and photodetector, using VED for the definition of the transparent and absorbing regions [5], [6]. The VED process requires no regrowth to define the transparent areas after epitaxial growth and allows a considerably higher conversion efficiency of laser output power into detector current than previous approaches. Although a rapid thermal anneal (RTA) of 960 °C and 24 s is necessary for the process, no degradation in the performance of lasers or photodetectors was noted. We thereby demonstrate the utility of VED for selectively blue-shifting the absorption edge of a single-quantum well double-heterostructure and thus for direct application to PIC fabrication.

Manuscript received March 21, 1995; revised June 6, 1995.

The authors are with the Paul Scherrer Institute Zurich, Badenerstrasse 569, 8048 Zurich, Switzerland.

IEEE Log Number 9413522.

II. Vacancy-Enhanced Quantum-Well Disordering Mechanism

Through a partial disordering of a quantum well (QW) in a double-heterostructure waveguide, the bandgap energy can be increased by up to 60 meV. This results in a blue-shift of the absorption edge and therefore drastically reduces the absorption losses of a waveguide. The disordering is due to interdiffusion of Al and Ga between the GaAs QW and the $Al_{0.3}Ga_{0.7}As$ core region at elevated temperatures, and is greatly increased in the presence of a high concentration of column-III-vacancies. VED relies upon the outdiffusion of Ga ions into a SiO_2 capping layer to generate these vacancies, which diffuse into the heterostructure promoting intermixing. SrF_2 as a dielectric capping material inhibits vacancy generation, such that very little interdiffusion occurs in the regions of the crystal covered by the SrF_2 cap.

By patterning the wafer surface after growth into regions covered by SiO_2 and SrF_2, we are easily able to produce a pattern of transparent and absorbing waveguide sections. The blue-shift due to VED under the SiO_2-cap is temperature and anneal-time dependent, as seen in Table I. A wavelength shift of up to 68 nm under the SiO_2-cap and less than 10 nm under the SrF_2-cap was seen for a 90-s anneal at 960 °C. For the devices described in this letter, we applied only a 24-s anneal in order to minimize p-dopant diffusion into the n-type lower cladding layer. The PL wavelength of the as-grown material used for these experiments was 812 nm, that of the SrF_2-capped material 810 nm, and that of the SiO_2-capped material 793 nm. Fabry–Pérot lasers fabricated from all these types of material showed comparable properties. As-grown material lasers: $\lambda = 827$ nm, $J_{th} = 600$ A/cm^2, $\eta = 0.52$ W/A; SiO_2-capped lasers: $\lambda = 805$ nm, $J_{th} = 500$ A/cm^2, $\eta = 0.42$ W/A; SrF_2-capped lasers: $\lambda = 825$ nm, $J_{th} = 700$ A/cm^2, $\eta = 0.36$ W/A.

III. Fabrication

A metal-organic vapor phase epitaxy (MOVPE) grown layer structure on an n-type Si-doped (10^{18} cm^{-3} Si) GaAs substrate was used for waveguides, photodetectors, and lasers. The layers included an undoped 165-nm-thick $Al_{0.3}Ga_{0.7}As$ core containing a single GaAs quantum well (7 nm), sandwiched between a 1.1-μm-thick $Al_{0.8}Ga_{0.2}As$ lower cladding layer (n-

1041–1135/95$04.00 © 1995 IEEE

TABLE I
PHOTOLUMINESCENCE WAVELENGTH SHIFT OF SiO_2-CAPPED AND SrF_2-CAPPED MATERIAL AFTER A RAPID THERMAL ANNEAL OF 30, 60, AND 90 s AND AT DIFFERENT TEMPERATURES

anneal temperature [°C]	wavelength shift SrF_2 [nm]	wavelength shift SiO_2 [nm]
910	0.3 / 1.5 / 3.8	5.1 / 10.9 / 20.5
920	1.6 / 3.4 / 4.9	7.3 / 19.1 / 35.9
930	1.2 / 2.2 / 3.5	10.2 / 24.3 / 40.2
940	2.0 / 4.5 / 8.4	14.4 / 30.2 / 50.6
950	2.6 / 5.9 / 9.3	22.0 / 46.4 / 62.8
960	4.1 / 7.4 / 10.8	28.9 / 48.0 / 68.0

doped 1.5×10^{18} cm^{-3} Si) and a 0.8-μm-thick $Al_{0.8}Ga_{0.2}As$ upper cladding layer (p-doped 10^{18} cm^{-3} Mg). A 100-nm-thick highly p-doped (8×10^{18} cm^{-3} Zn) GaAs cap layer completed the structure.

Processing started with a 200-nm-thick e-beam-evaporated SiO_2 layer, patterned by standard photolithography and reactive ion etching (RIE) using a CF_4 plasma. Without stripping the photoresist, a 250-nm-thick SrF_2 layer was then thermally evaporated. Subsequent lift-off resulted in a nearly planar surface covered completely either with SiO_2 or SrF_2. The samples were then annealed by RTA for 24 s at 960 °C. During anneal, a GaAs proximity cap helps to prevent surface damage of the sample by generating a local As overpressure [7]. Both SrF_2 and SiO_2 were then removed, the former in diluted HCl (HCl/H_2O 1:9, 20 s) and the latter by CF_4 RIE.

Ridge-waveguide DBR lasers were fabricated in this selectively shifted substrate by dry-etching ridge waveguides in a process described previously [8]. The third-order grating had a period of 380 nm, 1:1 mark to space ratio, and a depth of 100 nm. There was a 30-nm buffer layer between grating and waveguide core, giving a coupling coefficient of approximately 100 cm^{-1}. 1200-μm and 1700-μm-long bars were cleaved, yielding two different types of devices: the 1700-μm bars consisted, as shown in Fig. 1, of 500-μm-long pumped sections with 2, 3, and 4-μm ridge widths, 50- to 150-μm-long nonabsorbing DBR grating sections, 500- to 650-μm-long transparent waveguides, and 500-μm-long absorbing photodiodes at the end of the waveguides. We describe in the following only devices with a 150-μm-long grating recess (grating length = 130 μm) and a ridge width of 4 μm. The 1200-μm bars were made out of the former ones by subsequent cleaving of the photodiode and the waveguide, and applying an AR coating after each cleave.

IV. CHARACTERIZATION

The DBR lasers were driven cw at room temperature; maximum output power was 5 mW from the cleaved facet alone, threshold current was 22 mA (J_{th} = 1.1 kA/cm^2), and slope efficiency was on the order of 0.2 W/A. This latter value could be further improved by ensuring a closer wavelength match between the Bragg peak of the grating (814 nm) and the semiconductor gain peak (825 nm). The laser emission from the cleaved facet, as seen in Fig. 2, was single transverse

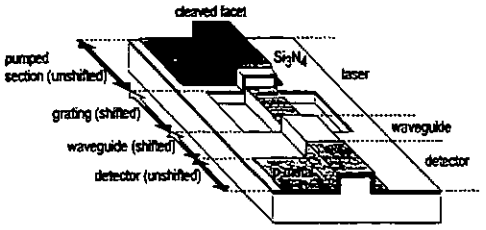

Fig. 1. Schematic diagram of DBR laser monolithically integrated with a transparent waveguide and a photodetector.

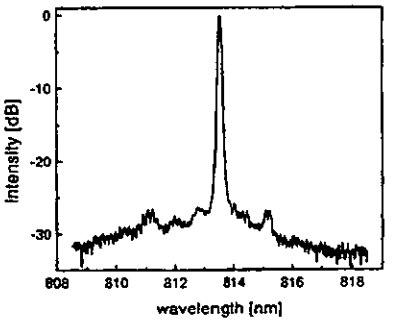

Fig. 2. Optical output spectrum of the DBR laser.

and longitudinal mode with a primary emission peak at λ = 814 m, a sidemode suppression ratio (SMSR) of 25 dB, and a FP mode spacing of 0.155 nm was obtained. The latter value corresponds to a cavity length of 630 μm or an effective grating length of 130 μm. The primary emission peak could be temperature-tuned between 7 and 25 °C without mode hops, leading to a temperature-tuning coefficient of 0.06 nm/°C (Fabry–Pérot lasers: 0.25 nm/°C). Repeated plasma exposure of the contact region during SiO_2-patterning, SiO_2-stripping, and Si_3N_4-contact hole etch increased the series resistance of the lasers drastically (37 W) and resulted in a relatively high threshold voltage, $V(I_{th})$, of 3.3 V.

Due to the moderate grating reflectivity (30–40%) and the relatively high losses in the short transparent waveguide (30 dB/cm), we observed external quantum efficiencies of η = 0.21 W/A from the cleaved facet and η = 0.13 W/A from the AR-coated grating-side facet. This corresponds to a total internal quantum efficiency of 20%. In addition, no significant optical power emitted vertically from the grating was noted. Small ripples are noticeable in the light versus current (L–I) curves from both the cleaved facet and the grating. The presence of these features indicates that the laser is undergoing an optimization of its internal stored energy under changing phase conditions due to carrier- and temperature-induced refractive index changes as current is increased, and are unique features of a laser with one cleaved (nonwavelength selective) and one grating (wavelength selective) reflector. These undulations, which were reproducible and without hysteresis, were less pronounced for emission from the grating side of the laser than from the cleaved facet. This occurs, we believe, because a

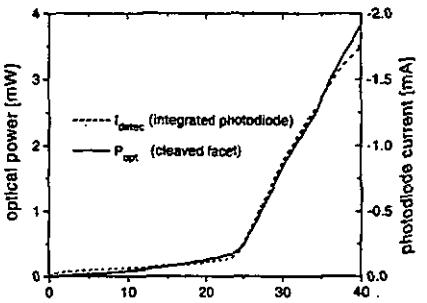

Fig. 3. Optical power and integrated photodetector current versus laser injection current.

decrease in grating reflectivity induces a simultaneous decrease of the laser internal power, resulting in nearly constant laser output power from the grating since the output power is the product of internal power and mirror transmission.

The 1700-μm-long devices added an absorbing 500-μm-long photodetector to these laser/waveguide structures. The resistances parallel to the reverse-biased diodes and between them were all between 3 and 5 kΩ. These small resistances generated large leakage currents across the p-o-junctions and are caused by the incomplete electrical isolation of the remaining upper p-clad between laser and detector. As shown in Fig. 3, we simultaneously measured the cleaved facet output power with an external photodetector and the output power of the grating side with the integrated photodetector. Loss measurements showed that wavelength-shifted waveguides had optical losses comparable to as-grown transparent waveguides and are on the order of 1.5 dB for the short lengths employed. Due to the long absorbing length of the photodiode and based upon the measured small amount of transmitted light (typically 1% of the laser output power), we can assume a high responsivity (>0.6 A/W) of the photodiode; implying >90% quantum efficiency. Conversion of laser output power into detector current was slightly lower (0.47 A/W), if we assume that the laser output from the grating and the cleaved facet are roughly equal. No obvious performance differences between annealed and nonannealed photodetectors was noted.

V. Conclusion

DBR lasers monolithically integrated with a nonabsorbing grating section, a transparent waveguide and an absorbing photodetector have been fabricated while requiring only a single MOVPE growth step. The absorbing and transparent areas on the wafer were defined after growth by VED using two different surface dielectrics, SiO_2 for the transparent regions and SrF_2 for the absorbing segments. The lasers operated cw at room temperature and emitted 5 mW at 814 nm in a single transverse and longitudinal mode. Conversion of laser output power into detector current was typically 0.47 A/W. Device performance is not adversely affected by the VED process, and the simplicity and flexibility of the approach is useful for the design and fabrication of PIC's for numerous applications.

Acknowledgment

The authors gratefully acknowledge the help of M. Moser and H. P. Schweizer for crystal growth, D. Jeggle and A. Vonlanthen for processing assistance, J. Söchtig for enlightening discussions, and M. T. Gale, H. W. Lehmann and R. Dändliker (University of Neuchâtel) for their generous support.

References

[1] R. J. Deri, W. Doldissen, R. J. Hawkins, R. Bhat, J. B. D. Soole, L. M. Schiavone, M. Seto, N. Andreadakis, Y. Silberberg, and M. A. Koza, "Efficient vertical coupling of photodiodes to InGaAsP rib waveguides," *Appl. Phys. Lett.*, vol. 58, pp. 2749–2751, 1991.

[2] K.-Y. Liou, U. Koren, E. C. Burrows, M. Oron, B. J. Miller, M. Young, G. Raybon, and C. A. Burrus, "Operation of integrated InGaAsP/InP optical amplifier-monitoring detector with feedback control circuit," *IEEE Photon. Technol. Lett.*, vol 2, pp. 878–880, 1990.

[3] P. Vettinger, M. K. Benedict, G.-L. Bona, P. Buchmann, E. C. Cahoon, K. Datwyler, H.-P. Dietrich, A. Moser, H. K. Seitz, O. Voegeli, D. J. Webb, and P. Wolf, "Full-wafer technology—A new approach to large-scale laser fabrication and integration," *IEEE J. Quantum Electron.*, vol. 27, pp. 1319–1331, 1991.

[4] C.-H. Chen and S.-C. Lee, "Monolithic integration of an AlGaAs/GaAs surface emitting laser diode and a photodetector," *Appl. Phys. Lett.*, vol. 59, pp. 3592–3594, 1991.

[5] I. Gontijo, T. Krauss, J. H. Marsh, and R. M. De La Rue, "Postgrowth control of GaAs/AlGaAs quantum well shapes by impurity free vacancy diffusion," *IEEE J. Quantum Electron.*, vol. 30, pp. 1189–1195, 1994.

[6] H. P. Zappe, D. Hofstetter and H. E. G. Arnot, "Quantum well engineering for semiconductor integrated optical sensors," *Proc. SPIE*, vol. 2213, pp. 205–212, 1994.

[7] L. J. Guido, N. Holonyak, K. C. Hsieh, R. W. Kaliski, W. E. Plano, R. D. Burnham, R. L. Thornton, J. E. Epler and T. L. Paoli, "Effects of dielectric encapsulation and As overpressure on Al–Ga interdiffusion in $Al_xGa_{1-x}As/GaAs$ quantum well heterostructures," *J. Appl. Phys.*, vol. 61, pp. 1372–1379, 1987.

[8] D. Hofstetter, H. P. Zappe, J. E. Epler and J. Schöttig, "Single growth-step GaAs/AlGaAs distributed Bragg reflector lasers with holographically-defined recessed gratings," *IEE Electron. Lett.*, vol. 30, pp. 1858–1859, 1994.

Paper IV

Multiple wavelength Fabry–Pérot lasers fabricated by vacancy-enhanced quantum well disordering

D. Hofstetter,[a] H. P. Zappe, J. E. Epler, and P. Riel
Paul Scherrer Institut Zürich, Badenerstrasse 569, CH-8048 Zürich, Switzerland

(Received 20 March 1995; accepted for publication 1 August 1995)

Wavelength-shifted GaAs/AlGaAs Fabry–Pérot ridge waveguide lasers were fabricated by vacancy-enhanced quantum well disordering using dielectric cap annealing. 500 μm long and 4 μm wide Fabry–Pérot lasers with emission wavelengths selectively shifted by 20 nm were integrated with unshifted lasers on the same chip, characterized and further compared with lasers fabricated from as-grown material. These investigations showed that the absorption edge of a single-quantum well double heterostructure can be selectively blueshifted after epitaxial growth without compromising diode laser performance. © *1995 American Institute of Physics.*

Postgrowth control of a quantum well (QW) profile has important applications for monolithic integration of active and passive optoelectronic components. A straightforward realization of many concepts in integrated optoelectronics requires a postgrowth conversion of a semiconductor heterostructure into a pattern of transparent and absorbing regions. The absorbing sections become light sources and detectors while the transparent regions could be low-loss waveguides, phase modulators, or distributed Bragg reflectors. The most promising processes are based upon a local partial intermixing of a quantum well to blueshift the energy band gap by several tenths of nm. Demonstrated techniques include impurity-induced disordering using various impurity species[1,2] and vacancy-enhanced disordering (VED).[1–7] VED by dielectric cap annealing has the advantage that only partial intermixing occurs, leaving waveguiding structures intact, and that the electrical properties of the material are not strongly affected. Recently, VED has been used to blueshift the absorption edge of the grating section of a DBR laser.[8] However, threshold currents were increased by either Zn diffusion into the active layer[9,10] or a mismatch between Bragg peak of the grating and gain peak of the material raising doubts about the applicability of the process. Our results indicate that VED can be employed in integrated optoelectronics without the drawbacks listed above. In this letter we describe the use of VED to locally shift the band gap of a single-QW separate-confinement double heterostructure. Ridge waveguide Fabry–Pérot lasers were fabricated from unshifted and shifted sections on the same laser bar. Both showed cw output powers up to 12 mW per facet, threshold currents less than 14 mA and a slope efficiency of 0.42 W/A. These values are comparable with those of unannealed devices fabricated from the same material.

The layer structure for these experiments was a MOVPE-grown separate-confinement double heterostructure grown on an n-type, Si-doped (10^{18} cm^{-3} Si) GaAs substrate and consisted of the following layers: a 1.1 μm thick $Al_{0.8}Ga_{0.2}As$ lower cladding layer (n-doped 1.5×10^{18} cm^{-3} Si), an undoped 165 nm thick $Al_{0.3}Ga_{0.7}As$ core containing a single GaAs QW (7 nm) and an 0.8 μm thick $Al_{0.8}Ga_{0.2}As$ upper cladding layer (p-doped 10^{18} cm^{-3} Mg) covered with a 100 nm thick highly p-doped 10^{18} cm^{-3} (8×10^{18} cm^{-3} Zn) GaAs cap layer.

Dielectric cap annealing, which is used for the VED, has been described extensively in Refs. 5 and 9; therefore, we will give only a brief introduction. Using standard processing techniques, the sample was completely covered with a single layer of either e-beam evaporated SiO_2 or thermally evaporated SrF_2. During rapid thermal annealing (RTA) at 960 °C for 30 s, group-III vacancies are generated under the SiO_2 cap, but not under the SrF_2 cap. Under the SiO_2, the vacancies promote intermixing of the Ga in the GaAs quantum well with column-III atoms [Al,Ga] of the adjacent $Al_{0.3}Ga_{0.7}As$ core, thereby increasing the effective Al content and the energy band gap of the QW. Transmission electron microscope pictures of such intermixed quantum wells fabricated in this material system are shown in Ref. 11. Figure 1 shows the achievable blueshifts of the photoluminescence spectrum excited with an argon-ion laser (λ=488 nm, P=10 mW) and measured at room temperature. After RTA of 30, 60, and 90 duration, at temperatures between 910 and

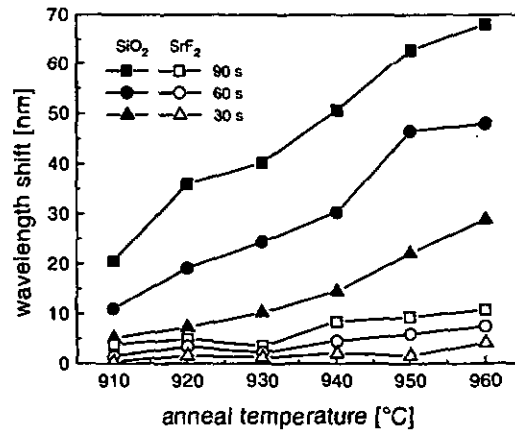

FIG. 1. Photoluminescence wavelength shift of SiO_2-capped and SrF_2-capped material after vacancy-enhanced disordering at different anneal temperatures and anneal times.

[a]Electronic mail: hofstetter@psi.ch

 0003-6951/95/67(14)/1978/3/$6.00 © 1995 American Institute of Physics

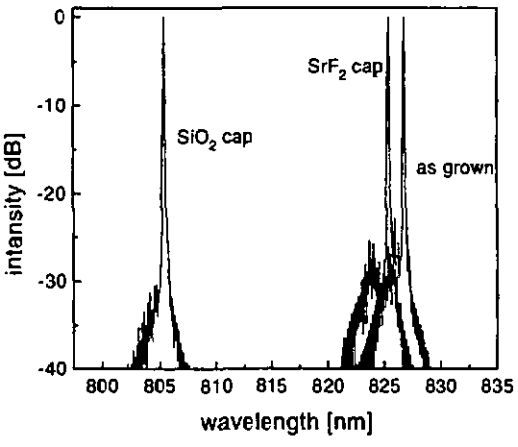

FIG. 2. Optical spectra of SiO_2-capped, SrF_2-capped, and as-grown material Fabry–Pérot lasers.

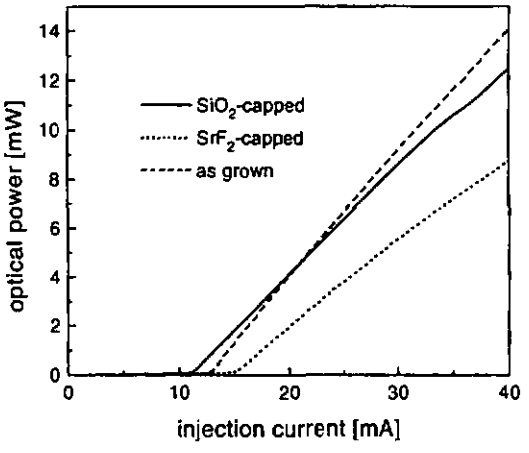

FIG. 3. L–I curves of SiO_2-capped, SrF_2-capped, and as-grown material Fabry–Pérot lasers.

960 °C, we measured blueshifts of the photoluminescence spectrum of 25 to 70 nm under the SiO_2 cap and less than 10 nm under the SrF_2 cap.

Lasers were then fabricated in both the shifted and the unshifted regions and in as-grown material. The process has been described previously[12] and is based upon dry etching of 4 μm wide ridges to within 100 nm of the waveguide core. 250 nm of Si_3N_4 was used as a passivating and electrically isolating layer on the shoulders and the sidewalls of the ridges. The material was cleaved into 500 μm long bars containing shifted and unshifted areas. The different types of lasers were separated by 250 μm and were tested unbonded in bar form, under cw conditions and at room temperature.

Figure 2 shows the emission spectra of three representative lasers driven cw above threshold, all at approximately the same current density. The as-grown, SrF_2-, and SiO_2-capped devices exhibit a peak spontaneous emission of 826, 823, and 805 nm, respectively; i.e., wavelength shifts of 3 and 21 nm. The corresponding photoluminescence wavelength shifts measured in this material are 2 and 19 nm ($\lambda_{initial}$=812 nm). These values are slightly smaller than those of the corresponding photoluminescence spectra (triangles at 960 °C in Fig. 1) because of the shorter anneal time (24 s instead of 30 s). The lasing wavelengths are located at or 1 nm to the long wavelength side of the spontaneous emission peak, typical for our Fabry–Pérot lasers. All devices are single mode with a side mode suppression ratio of 20 dB when driven at $I=3\times I_{th}$.

In Fig. 3 are shown the cw light versus current (L–I) data for the three devices of Fig. 2. The as-grown laser had a threshold current of 12 mA (J_{th}=600 A/cm^2) and a slope efficiency of 0.52 W/A. A maximum output power of 14 mW at $I=4\times I_{th}$ was achieved. In comparison, the L–I curve of the SiO_2-capped laser had a lower threshold current of 10 mA (J_{th}=500 A/cm^2), while the SrF_2-capped device had a somewhat higher threshold current of 14 mA (J_{th}=700 A/cm^2). The slope efficiencies of the SiO_2-capped laser (0.42 W/A) and the SrF_2-capped laser (0.36 W/A) are lower then that of the as-grown laser. Measurements of several lasers of each type gave nearly identical results.

I–V curves of the three lasers are shown in Fig. 4. The characteristics of the as-grown and the SiO_2-capped lasers are comparable with threshold voltages, $V(I_{th})$, of 2.1 and 2.15 V and series resistances of 30 and 24 Ω, respectively. The higher threshold voltage of 3.3 V and series resistance of 37 Ω of the SrF_2-capped laser may be a result of a displaced p-n junction caused by dopant diffusion during the RTA. However, no evidence of Zn diffusion into the n side was observed in stain-etched cross sections of the material. Another possible cause is the exposure of the contact region of the SrF_2-capped devices during three plasma processes (SiO_2 patterning, SiO_2 strip and Si_3N_4 contact hole etch). The SiO_2-capped lasers experienced only one plasma exposure (Si_3N_4 contact hole etch). The higher threshold voltage

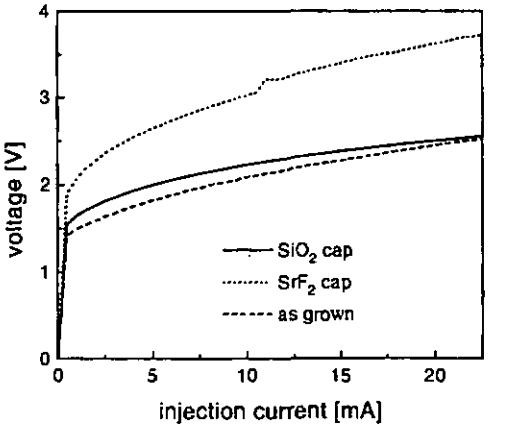

FIG. 4. I–V curves of SiO_2-capped, SrF_2-capped, and as-grown material Fabry–Pérot lasers.

and series resistance of the SrF_2-capped laser may explain the higher threshold current and reduced slope efficiency. Although no systematic lifetime measurements were done, we could not see any degradation of the laser performance during these measurements.

In conclusion, Fabry–Pérot lasers with two different emission wavelengths have been fabricated on the same bar. The wavelength shift of 20 nm was achieved through a post-growth process, vacancy-enhanced disordering. As opposed to earlier experiments,[9] the performance of these devices is comparable with that of as-grown material lasers. We could not see any Zn diffusion into the active region and furthermore, we were able to achieve cw operation of all our devices.

We are grateful to M. Moser and H. P. Schweizer for crystal growth, D. Jeggle and A. Vonlanthen for processing assistance, J. Söchtig for helpful discussions and H. W. Lehmann, M. T. Gale and R. Dändliker (IMT, University of Neuchâtel) for their generous support.

[1] G. F. Redinbo, H. G. Craighead, and J. M. Hong, J. Appl. Phys. **74**, 3099 (1993).
[2] R. L. Thornton, W. J. Mosby, and T. L. Paoli, J. Lightwave Technol. **6**, 786 (1988).
[3] D. G. Deppe, L. J. Guido, N. Holonyak, Jr., K. C. Hsieh, R. D. Burnham, R. L. Thornton, and T. L. Paoli, Appl. Phys. Lett. **49**, 510 (1986).
[4] J. H. Marsh, S. J. Hansen, A. C. Bryce, and R. M. De La Rue, Opt. Quantum Electron. **23**, 941 (1991).
[5] *I. Gontijo, T. Krauss, J. H. Marsh, and R. M. De La Rue, IEEE J. Quantum Electron.* **QE-30**, 1189 (1994).
[6] H. P. Zappe, D. Hofstetter, and H. E. G. Arnot, Proc. SPIE **2213**, 205 (1994).
[7] I. Gontijo, Y. S. Tang, R. M. De La Rue, C. M. Sotomayor Torres, J. S. Roberts, and J. H. Marsh, J. Appl. Phys. **76**, 5434 (1994).
[8] S. G. Ayling, J. Beauvais, and J. H. Marsh, *Proceedings of the 6th European Conference on Integrated Optics and Technical Exhibit* (ECIO, 1993), pp. 7–10.
[9] S. G. Ayling, A. C. Bryce, I. Gontijo, J. H. Marsh and J. S. Roberts, Semicond. Sci. Technol. **9**, 2149 (1994).
[10] S. O'Brien, J. R. Shealy, F. A. Chambers, and G. Devane, J. Appl. Phys. **71**, 1067 (1992).
[11] L. J. Guido, N. Holonyak, Jr., K. C. Hsieh, R. W. Kaliski, W. E. Plano, R. D. Burnham, R. L. Thornton, J. E. Epler, and T. L. Paoli, J. Appl. Phys. **61**, 1372 (1987).
[12] D. Hofstetter, H. P. Zappe, J. E. Epler, and J. Söchtig, Electron. Lett. **30**, 1858 (1994).

Paper V

Monolithically integrated optical displacement sensor in GaAs/AlGaAs

D. Hofstetter, H.P. Zappe and R. Dändliker

Indexing terms: Displacement measurement, Optical sensors, Integrated optoelectronics

A monolithically integrated displacement sensor has been fabricated in the GaAs/AlGaAs material system. The device is configured as a Michelson interferometer and consists of a DBR laser, a directional coupler, transparent waveguides and a photodetector. Interference fringes could be seen at a measurement distance of up to 45cm, requiring only the alignment of an external GRIN lens for beam collimation.

Introduction: The monolithic integration of lasers and interferometers is one of the most important steps towards the realisation of photonic integrated circuits for sensing applications. For displacement measurement using an integrated optical approach, Michelson interferometers based on glass, $LiNbO_3$ or silicon have been presented [1 – 4]; all of these technologies, however, require external mounting and alignment of a light source, since monolithic integration of a laser is not yet possible in these materials.

We present here the first demonstration, to our knowledge, of a GaAs-based monolithically integrated displacement sensor. The device is configured as a Michelson interferometer and consists of a DBR laser, a photodetector and transparent waveguides, all monolithically integrated on a single piece of GaAs. The fabrication of such monolithically integrated sensors requires a simple laser fabrication technology, compatible with the interferometer fabrication process, and a postgrowth bandgap engineering process to define transparent areas for the Bragg reflector and the waveguides and absorbing sections for the laser and the photodetector. Furthermore, the measurement of small optical signals needs good electrical isolation between laser and photodetector. The first of these three requirements was fulfilled by the use of a so-called grating recess, allowing the fabrication of the DBR laser without regrowth [5]. The second was accomplished by vacancy-enhanced quantum well disordering (VED) [6], while the third could be achieved with a proton implantation step.

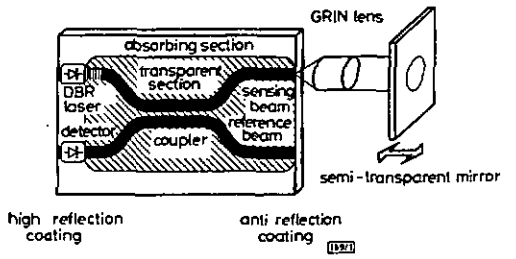

Fig. 1 *Schematic diagram of monolithically integrated Michelson interferometer with characterisation setup*

Fabrication process: The displacement sensor is shown schematically in Fig. 1. The light generated by the DBR laser is divided into a reference and a measurement beam by the directional coupler. After reflection at the cleaved facet and from the external object mirror, the two beams interfere and are detected in the

photodetector. The ridge waveguides were 3mm wide and had curve radii of 500μm, therefore requiring strong index-guiding achieved by etching through the waveguide core. Three different coupler lengths (100/275/450μm) and two Bragg reflector lengths (150/200μm) were employed. The pumped laser sections and the photodetectors were both 500μm long.

The fabrication technology of this device was similar to that published previously [7]. The layer structure was a MOVPE-grown single-quantum-well double-heterostructure with a 160nm core and two 1μm cladding layers. For the VED process, 200nm of SiO_2 were evaporated on the transparent sections (Bragg reflector, waveguides, coupler), while a 250nm thick SrF_2 layer was used on top of the absorbing sections (laser, photodetector) to prevent intermixing. VED was accomplished by a rapid thermal anneal at 960°C for 30s, followed by the complete removal of the dielectric layers from the wafer surface. A photoluminescence shift difference of 20nm was seen after this annealing step.

Proton implantation for electrical device isolation (a dose of 4×10^{15}cm^{-2} at three different energies, 40/70/100keV) was done everywhere outside the waveguiding areas; in addition, 2μm wide stripes were implanted across the waveguides between active devices to electrically isolate the components without markedly increasing the waveguide losses. The processing was then completed using standard waveguide etch and metallisation techniques.

On the cleaved facet of the DBR laser (left side of Fig. 1), a high reflectance Al-mirror was evaporated to improve laser threshold (60nm SiO_2 for isolation, 120nm Al as mirror), while on the measurement side of the interferometer (right side of Fig. 1), an antireflection coating (Balzers PASO III) was used to reduce coupling losses of the measurement beam and to attenuate the reflected reference beam. The remaining reflectance of 2% was still sufficient for the reference beam to produce a distinct interference signal.

Characterisation and measurement results: For performing a displacement measurement, the DBR laser was driven CW at room temperature with an injection current of 50mA. Its threshold current of ~35mA resulted in a threshold current density of 2.2kA/cm^2; emission wavelength was 820nm.

The photodetector was reverse biased at −5V and had a leakage dark current of 500pA; responsivity of such detectors is typically 0.5A/W. The electrical resistance between the laser diode and the adjacent photodiode was measured to be in the order of 10GΩ. Since the absorption edge was blue-shifted by only 20nm, the waveguide losses were relatively high (40dB/cm) owing to band-edge absorption.

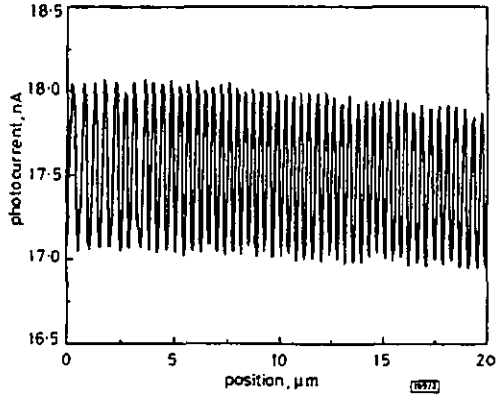

Fig. 2 *Interferogram for 13cm mirror distance and 95% mirror reflectance as measured by integrated photodetector*

The interferometer chips were tested in bar form and were Peltier temperature-stabilised to better than 0.1K. The measurement beam, collimated by an external GRIN lens, was directed onto a semitransparent mirror through which the reflected beam position could be observed by a CCD camera. Observation was necessary to adjust the beam properly into autocollimation. The semitransparent mirror was fixed to a piezo-driven, gimbal-mounted holder with which the measurement distance could be varied between 3 and 45cm. With this arrangement, we were able to measure a 20μm movement (limited by the travel of the piezo-actuator) which led to 49 interference fringes, each of them corresponding to a mirror movement of 410nm (see Fig. 2). Displacements of a quarter of a fringe, or approximately 100nm, were resolvable. The measured interference signal showed a good temporal stability but was very sensitive to vibration of the external components.

A large constant offset in the photodiode current, dominated by optical crosstalk between laser and photodiode, was seen. To evaluate this current, we removed the external optics and measured the signal magnitude. Since we know the approximate reflectivity of the AR-coated facet (2%), we were able to estimate the crosstalk current from this measurement, leading to a value of 16.7nA. This value agreed well with a more comprehensive measurement involving the use of five different external mirrors with differing reflectivities. Subtracting the crosstalk current from the signal values shown in Fig. 2 results in a considerably improved contrast.

The crosstalk current can be reduced by an isolation trench between laser and photodiode. For practical use, the functionality of the interferometer must be enhanced by the inclusion of a phase shifting element as part of a double-arm interferometer allowing quadrature detection for determination of displacement direction as well as magnitude.

Conclusion: A single monolithically integrated Michelson interferometer chip used as an optical displacement sensor was designed, fabricated and tested. Interference fringes were seen at a distance of up to 45cm. The only element requiring alignment was the external GRIN lens for the collimation of the measurement beam.

Acknowledgments: The authors gratefully acknowledge the help of M. Moser, J.E. Epler and H.P. Schweizer for crystal growth, P. Riel, A. Vonlanthen, D. Jeggle and the PSI workshop team for technical assistance and J. Söchtig and M.T. Gale for helpful discussions.

© IEE 1995
17 October 1995

Electronics Letters Online No: 19951455

D. Hofstetter and H.P. Zappe (*Paul Scherrer Institute, Badenerstrasse 569, 8048-Zürich, Switzerland*)

R. Dändliker (*Institute of Microtechnology, University of Neuchâtel, 2000-Neuchâtel, Switzerland*)

References

1 JESTEL, D., BAUS, A., and VOGES, E.: 'Integrated-optic interferometric microdisplacement sensor in glass with thermo-optic phase modulation', *Electron. Lett.*, 1990, 26, pp. 1144–1145

2 ULBERS, G.: 'An integrated-optics sensor on silicon for the measurement of displacement, force and refractive index', *SPIE Microoptics II*, 1991, 1506, pp. 99–110

3 TODA, H., HARUNA, M., and NISHIHARA, H.: 'Integrated-optic heterodyne interferometer for displacement measurement', *J. Lightwave Technol.*, 1991, LT-9, pp. 683–687

4 HELLESØ, O.G., BENECH, P., and RIMET, R.: 'Interferometric displacement sensor made by integrated optics on glass', *Sens. Actuators*, 1995, 46–47, pp. 478–481

5 HOFSTETTER, D., ZAPPE, H.P., EPLER, J.E., and SÖCHTIG, J.: 'Single growth-step distributed Bragg reflector laser with a holographically-defined recessed grating', *Electron. Lett.*, 1994, 30, pp. 1858–1859

6 HOFSTETTER, D., ZAPPE, H.P., EPLER, J.E., and RIEL, P.: 'Multiple wavelength Fabry-Pérot lasers fabricated by vacancy-enhanced quantum well disordering', *Appl. Phys. Lett.*, 1995, 67, pp. 1978–1980

7 HOFSTETTER, D., ZAPPE, H.P., EPLER, J.E., and RIEL, P.: 'Monolithically integrated DBR laser, detector and transparent waveguide fabricated in a single growth step', *IEEE Photonics Technol. Lett.*, 1995, 7, pp. 1022–1024

Paper VI

A Monolithically Integrated Double Michelson Interferometer for Optical Displacement Measurement with Direction Determination

D. Hofstetter, H. P. Zappe, and R. Dändliker

Abstract— A monolithically integrated optical displacement sensor fabricated in the GaAs-AlGaAs material system is reported. The single-chip device consists of a distributed Bragg reflector laser, two photodetectors, two phase modulators, two Y-couplers, and two directional couplers. It is configured as a double Michelson interferometer and allows the determination of both magnitude and direction of a displacement. The detection of two 90° phase-shifted interferometer signals also resulted in an improved phase interpolation of $\phi/20$. Despite the relatively simple fabrication process, the integration of rather complex optical functions could be realized.

I. Introduction

INTEGRATED OPTICAL circuitry using III–V-semiconductors offers the possibility of monolithically integrating active and passive optical components. Such an integration is advantageous because of enhanced design flexibility, reduced or eliminated need for physical alignment procedures, greater robustness and potential for mass production.

Integrated optical displacement sensors have to date been fabricated on glass substrates using ion-exchanged strip waveguides by Jestel [1] and on silicon substrates with slab or ridge waveguides by Ulbers [2] and Voirin [3]. Two approaches employing III–V-semiconductor material, with the potential for integration as noted above, have been reported by Suhara [4] and by us [5]. Our previously reported device was single-Michelson-type, and, in contrast to the glass and silicon-based interferometers, not able to detect the direction of the movement. To the best of our knowledge, no III–V-based device allowing the measurement of two independent phase-shifted interference signals with an integrated laser has yet been published.

In this work, we describe a double Michelson interferometer consisting of one DBR laser, two photodetectors, two phase modulators, two Y-couplers, and two directional couplers with which both magnitude and direction of a movable external object could be measured. As can be seen in the schematic of Fig. 1, the light of the DBR laser was divided into two nearly independent Michelson interferometers by a Y-coupler. A relative phase shift between the two reference arms was generated by phase modulators allowing the detection of two interference signals in phase quadrature and thus the changes in displacement direction. Interference signals could be measured at mirror distances of up to 20 cm with sub-100 nm resolution.

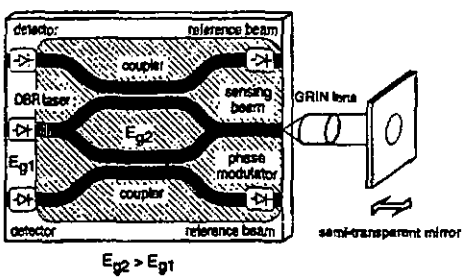

Fig. 1. Schematic of the monolithically integrated double Michelson displacement sensor with direction determination. The diode symbols in the reference beams represent the phase modulators.

This displacement measurement chip was fabricated on a double heterostructure layer sequence requiring only a single growth step. A vacancy-enhanced disordering (VED) process was employed to define absorbing photodetector and pumped laser areas as well as transparent waveguiding sections [6]. In addition, a simplified DBR laser process using a grating recess allowed the integration of all necessary optical functions with a relatively simple technology.

II. Technology

The layer structure used for these devices was grown by metal-organic vapor phase epitaxy on a GaAs substrate (n-doped 10^{18} cm^{-3} Si) and included an undoped 165-nm-thick $Al_{0.3}Ga_{0.7}As$ waveguide core containing a single GaAs quantum well (7 nm). This layer was sandwiched between a 1.1-μm-thick $Al_{0.8}Ga_{0.2}As$ lower cladding layer (n-doped 1.5×10^{18} cm^{-3} Si) and an 0.85-μm-thick $Al_{0.8}Ga_{0.2}As$ upper cladding layer (p-doped 10^{18} cm^{-3} Mg). A 160-nm-thick highly p-doped (5×10^{18} cm^{-3} Zn) GaAs cap layer completed the structure.

Integration of lasers, photodetectors, modulators and waveguides requires compatible process technologies for all necessary components of the circuit. For this work, we employed processes reported previously, namely the fabrication of a single growth step DBR laser [7], [8] and the selective, partial

Manuscript received May 30, 1996; revised July 1, 1996.

D. Hofstetter and H. P. Zappe are with the Paul Scherrer Institute, Badenerstrasse 569, 8048 Zurich, Switzerland.

R. Dändliker is with the Institute of Microtechnology, University of Neuchâtel, Rue A.-L. Breguet 2, 2000 Neuchâtel, Switzerland.

Publisher Item Identifier S 1041-1135(96)07439-3.

1041-1135/96$05.00 © 1996 IEEE

intermixing of quantum wells for postgrowth bandgap-shifting [9]. Proton implantation (H^+, 4×10^{15} cm^{-2}, 40/70/100 keV) was used to generate a high electrical resistance between laser and photodetectors (>10 GΩ), and the reduction of optical crosstalk between these two elements was achieved by dry etching an isolation trench. This trench was filled with the p-metallization layers to prevent the light from going directly from the laser into the photodetector.

III. Interferometer Description

The optical circuits described in this letter were configured as double Michelson interferometers, shown schematically in Fig. 1. The ridge width of the waveguides was 3 μm and the curve radii were 500 μm. All passive waveguides were fabricated in the areas with intermixed quantum wells and had an absorption loss of 35–45 dB/cm, due to the relatively small bandgap difference of 45 meV between intermixed *(bandgap energy E_{g2})* and nonintermixed *(bandgap energy E_{g1})* sections. Since the total waveguide length did not exceed 3 mm, this relatively high absorption loss was not overly detrimental for interferometer performance.

For the splitting of the incoming light into the reference and sensing arms, we used either directional couplers with a length of 500 μm or, in an alternative design, Y-couplers. Depending on the type of coupler used, the total cleaved chip length was 1.95 mm for devices with Y-couplers or 2.6 mm for those with directional couplers. Modulator length was 340 μm; when driven at −12-V reverse voltage, we measured a one-pass phase shift of $\pi/16$.

Both the pumped laser section and photodetectors were fabricated in the nonintermixed, and thus absorbing, areas of the chip and had a length of 500 μm each. The length of the nonabsorbing DBR grating section was 200 μm; we used a 3rd order grating with a period of 380 nm, a depth of 150 nm and a 1:1 line-to-space ratio. A 70-nm thin buffer layer between the bottom of the grating and the waveguide core resulted in a calculated grating coupling coefficient of 100 cm^{-1}; this gave the desired grating reflection coefficient of about 95%. The left cleaved facet of the interferometer served as second laser mirror.

The DBR lasers of our displacement sensors were driven CW at room temperature. Typical threshold currents were 30 mA, corresponding to a threshold current density of 2 kA/cm^2. The emission wavelength was 822 nm and the spectrum showed a sidemode suppression ratio of approximately 25–30 dB. For interferometric measurements, the lasers were usually operated at 50 mA. At this current level, 2 mW of optical power was emitted from the left cleaved facet of the device. A measurement of the output power from the grating side was performed indirectly by coupling its light through a straight waveguide into a photodetector. Under the assumption of 40 dB/cm waveguide loss, we estimated the output power into the interferometer to be around 2 μW. This asymmetry of the optical output power was due to the different reflectances (facet: 30%, grating: 95%) of the two laser mirrors.

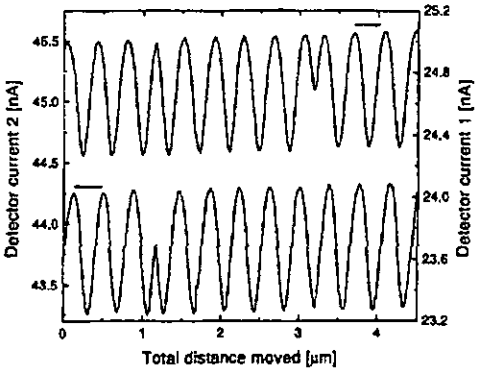

Fig. 2. The two detector currents $I(\phi)$ of the double Michelson interferometer for 3.5 cm mirror distance and 67% mirror reflectance showing the two interference signals. Direction changes occurred at 1.2 μm and at 3.3 μm.

IV. Performance

The measurement setup for interferometer characterization consisted of a Peltier temperature-stabilized mount for the interferometer bars, an external, independently movable GRIN lens (pitch = 0.23) for measurement beam collimation and a piezo-driven, semitransparent mirror as measurement object (67% reflectance). A CCD camera-based imaging system allowed rough alignment of the measurement beam into autocollimation. Fine adjustment was performed by optimizing the detector signals during the measurement. The travel of the displacement piezoactuator was restricted to 20 $d\mu$m; the movement was stimulated by a symmetric sawtooth voltage signal from a function generator. The amplitude of the voltage was adjusted to change the direction of the movement after every 2 μm of displacement.

Fig. 2 shows the result of an interferometric measurement at a mirror distance of 3.5 cm. The dc components of the interferometer signal, defined by

$$I(\phi) = I_{\text{cross}} + \frac{I_0}{2}(1 + V \cdot \cos\phi)$$

include a constant offset in the detector current signal, I_{cross}, due to optical crosstalk between laser and detector, as well as the component $I_0/2$ due to visibility, $V = (I_{\max} - I_{\min})/(I_{\max} + I_{\min})$, less than unity. In Fig. 2, there are two changes of the movement direction: one at 1.2 μm and another at 3.3 μm. One interference fringe corresponds to a mirror movement of one half of the measurement wavelength, namely 411 nm. The amplitudes of the detector current signals, $(I_0V/2)$, were 0.5 nA and 0.4 nA. Optical crosstalk signals of 35 nA and 16 nA, respectively, were seen because of the insufficiently deep isolation trench. The value of the crosstalk could be accurately determined by measuring the latter in an uncleaved interferometer bar; this approach suppressed all reflections at the measurement facet.

Plotting the two interferometer detector currents, $I(\phi)$, against each other resulted in a Lissajous-figure as shown in Fig. 3. The ratio of the two normalized ellipse main-axes allowed an estimate of the phase shift between the two signals, approximately 75–80°. With a longer phase modulator, it

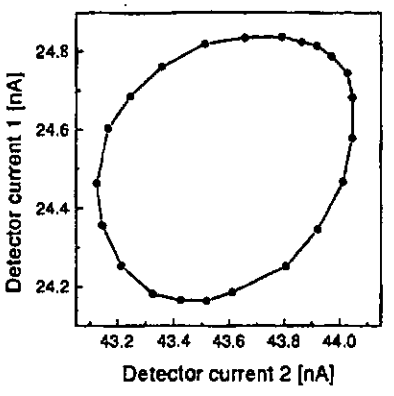

Fig. 3. Lissajous-figure of the two detector currents for 3.5-cm mirror distance and 67% mirror reflectance. Resolution of the measurement is about $\Delta\phi_{min} = \phi/20$.

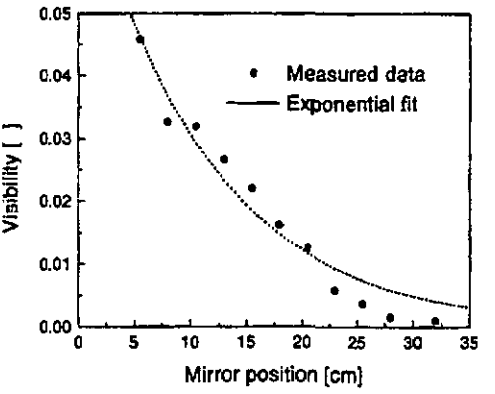

Fig. 4. Signal visibility versus mirror distance of a simple Michelson interferometer of the same fabrication run. This result implies a laser linewidth of $\Delta\nu = 800$ MHz.

should be possible to adjust the phase shift to the desired value of 90°. Nevertheless, a phase interpolation of $\phi/20$, resulting in 20-nm resolution of the displacement measurement, should be possible.

The slightly distorted sine- and cosine-shape of the two signals results from the parasitic reflection at the right cleaved facet of the sensing beam. This reflection at the measurement facet and the reflection at the object mirror generate a Fabry–Pérot interferometer cavity, whose optical field interferes with the one from the reference arm. We studied the behavior of such a three-mirror interferometer by simulation and were able to predict the experimentally measured asymmetric shape of the interferograms when changing the intrinsic phase between reference and sensing arm.

Fig. 4 shows the interference signal visibility, V, as a function of mirror distance for a single Michelson interferometer. A Fourier-transformation of this so-called autocorrelation function allowed a determination of the laser linewidth. Although typical DBR lasers, with a linewidth of 1 MHz or less, have coherence lengths of several hundred meters, the rapid decay of visibility with increasing distance as seen in the figure results from an enhanced linewidth of about 800 MHz. This increase is probably caused by the perturbation of the DBR laser through feedback from the cleaved right facet. In addition, the modal behavior of the sensing beam waveguide was not ideal; we could occasionally observe higher order waveguide modes under different coupling conditions. This effect also reduced the visibility and gave raise to "mode hopping" in the feedback, which was clearly indicated by spontaneous changes of the phase between the two interferometer signals.

V. Conclusion/Outlook

A monolithically integrated double Michelson interferometer for displacement measurement with direction determination was designed, fabricated and characterized. The device consisted of a DBR laser, detectors, modulators and waveguides, all fabricated on a single GaAs-AlGaAs-chip. Displacement measurements were performed using only one external element for beam collimation and a movable mirror as measurement object. Although using relatively simple standard processing technologies, we could demonstrate the fabrication of an advanced monolithic device with complex optical functions.

Acknowledgment

The authors are grateful to J. E. Epler and H. P. Schweizer for crystal growth; P. Riel, D. Jeggle and A. Vonlanthen for processing assistance; and J. Söchtig, M. T. Gale, and H. W. Lehmann for their generous support.

References

[1] D. Jestel, A. Baus and E. Voges, "Integrated-optic interferometric microdisplacement sensor in glass with thermo-optic phase modulation," *Electron. Lett.*, vol. 26, no. 15, pp. 1144–1145, 1990.

[2] O. Ulbers, "An integrated optim sensor on silicon for the measurement of displacement, force and refractive index," *Proc. SPIE, Micro-Optics II*, vol. 1506, 1991, pp. 99–110.

[3] O. Voirin, L. Falco, O. Boillat, O. Zogmal, P. Regnault, and O. Parriaux, "Monolithic double interferometer displacement sensor with wavelength stabilization," *Proc. Eur. Conf. Integrat. Opt. 93*, 1993, pp. 12-28–12-29.

[4] T. Suhara, T. Taniguchi, M. Uemukai, H. Nishihara, T. Hirata, S. Iio, and M. Suehiro, "Monolithic integrated-optic position/displacement sensor using waveguide ratings and QW-DFB laser," *IEEE Photon. Technol. Lett.*, vol. 7, no. 10, pp. 1195–1197, 1995.

[5] D. Hofstetter, H. P. Zappe, and R. Dändliker, "Monolithically integrated optical displacement sensor in GaAs/AlGaAs," *Electron. Lett.*, vol. 31, no. 24, pp. 2121–2122, 1995.

[6] J. Beauvais, J. H. Marsh, A. H. Kean, A. C. Bryce, and C. Button, "Suppression of bandgap shifts in GaAs/AlGaAs quantum wells using strontium fluoride caps," *Electron. Lett.*, vol. 28, pp. 1670–1672, 1992.

[7] D. Hofstetter, H. P. Zappe, J. E. Epler and J. Söchtig, "Single-growth-step GaAs/AlGaAs distributed Bragg reflector lasers with holographically-defined recessed gratings", *Electron. Lett.*, vol. 30, pp. 1858–1859, 1994.

[8] D. Hofstetter, H. P. Zappe, and J. E. Epler, "Ridge waveguide DBR lasers with nonabsorbing grating and transparent integrated waveguide," *Electron. Lett.*, vol. 31, no. 12, pp. 980–982, 1995.

[9] D. Hofstetter, H. P. Zappe, J. E. Epler, and P. Riel, "Multiple wavelength Fabry-Pérot lasers fabricated by vacancy-enhanced quantum well disordering," *Appl. Phys. Lett.*, vol. 67, pp. 1978–1980, 1995.

Paper VII

Submitted to *IEEE Journal of Lightwave Technology*, D. Hofstetter, 31.08.96

Optical displacement measurement with GaAs/AlGaAs-based monolithically integrated Michelson interferometers

Daniel Hofstetter, Hans P. Zappe, and René Dändliker

Abstract— **Two monolithically integrated optical displacement sensors fabricated in the GaAs/AlGaAs material system are reported. These single chip microsystems are configured as Michelson interferometers and comprise a distributed Bragg reflector laser, photodetectors, phase shifters and waveguide couplers. While the use of a single Michelson interferometer allows measurement of displacement magnitude only, a double Michelson interferometer with two interferometer signals in phase quadrature also permits determination of movement direction. In addition, through the use of two 90 ° phase-shifted interferometer signals in the latter device, a phase interpolation of $\phi/20$ is possible, leading to a displacement resolution in the range of 20 nm. The integration of these complex optical functions could be realized with a relatively simple fabrication process.**

I. Introduction

A.A. Michelson carried out the first measurements using the interferometer which bears his name in 1881 [1], [2], [3]; this historical experiment proved that the speed of light was not influenced by the motion of the earth relative to a hypothetical ether. The same experimental setup was subsequently used for spectroscopic and displacement measurements. In that age, gas vapor discharges were the only available spectrally pure light sources, such that displacement measurements were limited to distances of about 1 meter due to the limited coherence length of the source. Using highly coherent laser light, interferometric displacement measurement is possible at distances exceeding 100 m [4] and represents an important research and industrial tool.

Using the technology of integrated optics, light is propagated in waveguides instead of free space, implying that extremely small optical circuits can be fabricated. Integrated optical sensors using waveguides are thus very compact and physically robust and may easily be fabricated by mass-production techniques [5]. For these reasons, integrated optical Michelson interferometers have become very attractive for optical displacement measurement, both in the laboratory and for applications in the field.

We present in this paper the design, fabrication technology and characterization of III-V semiconductor-based, monolithically integrated displacement sensors. These fully integrated measurement microsystems include all active interferometer components on a single semiconductor chip. Following a brief survey of previous work in this field, we will present the required processes for the fabrication of a semiconductor-based interferometer, discuss distributed Bragg reflector lasers as light sources and selective bandgap shifting for on-chip transparency. We will then present the performance characteristics of both the single Michelson interferometer (SMI) [6] and the double Michelson interferometer (DMI) with two 90 ° phase-shifted reference beams [7] and conclude with a comparison of these structures and existing displacement sensors.

II. Summary of IO displacement sensors

Due to the attractive features of an integrated optical (IO) approach, numerous workers have developed Michelson interferometer-based displacement sensors using various technologies. One of these approaches has been described by Ulbers [8] and was commercially available for some time (Hommelwerke Sensor GmbH) [9]. This device consisted of a Michelson interferometer on a silicon chip where waveguiding was by planar waveguides. An external gradient index (GRIN) lens was used for the collimation of the measurement beam; in addition, an external diode laser and photodetectors were required for stimulation and signal measurement.

The IO Michelson interferometer fabricated by Jestel [10] (University of Dortmund) used ion-exchange stripe waveguides on a glass substrate, thermo-optic phase shifters to define the relative phase shift between the two reference arms and directional couplers to divide the incoming light into reference and sensing beam. This device consisted of two combined Michelson interferometers (often referred to as a double Michelson interferometer) and

O. Hofstetter was with the Paul Scherrer Institute, Badenerstrasse 569, 8048 Zurich, Switzerland and is now with the Xerox Palo Alto Research Center, 3333 Coyote Hill Road, Palo Alto, CA 94304

H.P. Zappe is with the Paul Scherrer Institute, Badenerstrasse 569, 8048 Zurich, Switzerland

R. Dändliker is with the Institute of Microtechnology, University of Neuchâtel, Rue A.-L. Breguet 2, 2000 Neuchâtel, Switzerland

allowed direction determination of the movable object. It also required an external diode laser and external photodetectors, plus one externally mounted beam-shaping element.

The measurement of displacement is also possible with Mach-Zehnder type interferometers; Voirin [11] (CSEM Neuchâtel) reported a Mach-Zehnder interferometer for this application. This sensor was fabricated in glass with ion-exchange stripe waveguides and wavelength-stabilized to within 10^{-6}. The usual external elements, namely laser, detectors and GRIN lens, were again necessary to operate the interferometer.

Recently, Suhara [12] published a monolithically IO position sensor. This III-V-semiconductor-based device was configured as a double Michelson interferometer and consisted of a DFB laser, planar waveguides and grating couplers but without a phase shift between the two reference beams. The grating coupler served as beam splitter and also as collimation lens for the measurement beam. A similar device with two phase-shifted interference signals but without an integrated DFB laser was demonstrated in 1989 [13].

III. III-V PROCESSING

Monolithically integrated optical circuits, fabricated in a III-V semiconductor system, have been extensively developed for telecommunication applications; the material systems used have been chosen for their suitability for the fabrication of lasers at the required wavelengths. Integration of the components necessary for an optical circuit requires the ability to fabricate an integratable laser, a means to selectively define transparency across the chip, and techniques for achieving electrical and optical isolation between devices. We will provide here an overview of the more salient aspects of the fabrication processes required for the interferometers.

A single layer structure was used for all required devices and was grown by metal-organic vapor phase epitaxy on a GaAs substrate (n-doped 10^{18} cm^{-3} Si). An undoped 165 nm thick $Al_{0.3}Ga_{0.7}As$ waveguide core containing a single GaAs quantum well (7 nm) was sandwiched between a 1.1 µm thick $Al_{0.8}Ga_{0.2}As$ lower cladding layer (n-doped $1.5x10^{18}$ cm^{-3} Si) and an 0.85 µm thick $Al_{0.8}Ga_{0.2}As$ upper cladding layer (p-doped 10^{18} cm^{-3} Mg). A 160 nm thick highly p-doped ($5x10^{18}$ cm^{-3} Zn) GaAs cap layer completed the structure.. As we discuss below, a post-growth bandgap shifting technique was used to selectively define transparency across the wafer, such that only a single epitaxy step was required.

Using a standard dry etch chemistry, 3 µm wide ridge waveguides were etched to a depth of 100 nm above the waveguide core; this was followed by the dry etch of a 500 nm deep optical isolation trench between laser and detectors, which was subsequently filled with p-metal layers. Passivation and electrical isolation of the ridge sidewalls was achieved through a 250 nm thick PECVD-grown Si_3N_4-layer. Proton implantation (H^+, $4x10^{15}$ cm^{-2}, 40/70/100 keV) and a cap etch, outside all contact areas, were used to generate a high electrical resistance between laser and photodetectors (>10 GΩ). After a contact hole etch on top of the ridges, standard p- and n-metal layers were evaporated.

Fabrication of the DBR grating involved the dry etch of a grating recess to a depth of about 230 nm above the core. The 3rd order grating was then defined by holographic exposure and subsequent dry etching. Cleaving of the bars to the desired length and evaporation of suitable facet coatings completed the processing. On the left laser facet, we used a high-reflection (HR) coating in order to reduce the laser threshold current; and on the right interferometer facet, an anti-reflection (AR) coating was evaporated to improve interferometer signal contrast.

A. *Selective bandgap shifting*

The combination of lasers and transparent waveguides requires the definition of sections with different bandgap energies on the same substrate. The methods to solve this problem can be divided into growth- and intermixing approaches. The most popular among the growth methods are selective area growth [14], [15], [16] and etch and epitaxial regrowth on a non-planar patterned substrate [17], [18]. The first allows the *simultaneous* epitaxy using different growth rates, and, therefore, the growth of quantum wells with different thicknesses. In contrast to this, the second uses a *subsequent* growth of material with different quantum well (QW) thicknesses. Other possibilities are selective partial intermixing of the QW using impurities [19], [20] or vacancies [21]. The primary advantage of the intermixing methods is that they require no additional regrowth, whereas the high temperature rapid thermal annealing (RTA) step necessary can lead to dopant migration. We employed an impurity-free intermixing approach, vacancy-enhanced disordering (VED), for the definition of transparent regions.

The VED technique required that the sample be completely covered with a single layer of either e-beam evaporated SiO_2 or thermally evaporated SrF_2. During RTA at 960 °C for 30 s, group-III-vacancies are generated under the SiO_2-cap but not under the SrF_2-cap. Under SiO_2, the vacancies promote intermixing of the Ga in the initially pure GaAs QW with Al of the adjacent $Al_{0.3}Ga_{0.7}As$ core, thereby increasing the Al-content and the energy bandgap of the QW. The final effect is an anneal temperature-

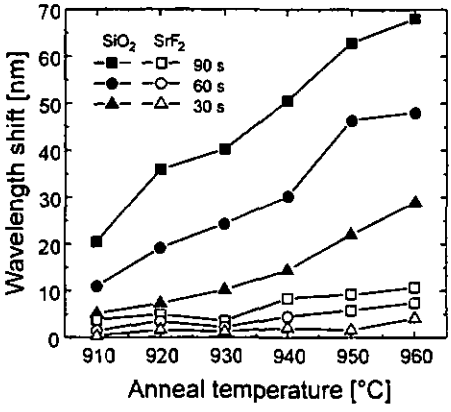

Fig. 1 - Photoluminescence wavelength shift of SiO_2-capped and SrF_2-capped material after vacancy-enhanced disordering at different anneal temperatures and anneal times. Excitation of the photoluminescence was accomplished with an argon-ion laser (λ = 488 nm, P = 10 mW) and measured at room temperature.

dependent blue-shift of the photoluminescence (PL) spectrum. Figure 1 shows the achieved blue-shifts as a function of temperature and anneal time. After an RTA of 30, 60 and 90 s duration, and at temperatures between 910 °C and 960 °C, we measured blue-shifts of 5 to 68 nm under the SiO_2-cap and less than 10 nm under the SrF_2-cap. Both dielectrics are stripped by wet or dry etchants after the anneal step.

This means to selectively promote a blue-shift in the absorption wavelength can then easily be used to define transparent regions in a quantum well, waveguide-based optical circuit; for the applications discussed below, the passive waveguides and couplers were fabricated in regions covered with SiO_2 during anneal, whereas the lasers and photodetectors were defined in the unshifted regions defined by SrF_2.

B. *Bandgap-shifted Fabry-Pérot lasers*

In order to demonstrate the good laser quality of material subject to a VED anneal, we fabricated Fabry-Pérot lasers in both the shifted and the unshifted regions of annealed material, as well as in as-grown material in a process described previously [22]. The lasers were 500 µm long with a ridge width of 4 µm and were tested in bar form under CW conditions at room temperature. The spectra of representative as-grown, SrF_2-, and SiO_2-capped devices showed laser emission at wavelengths of 826, 823, and 805 nm, respectively; thus the VED-induced wavelength shifts were 3 nm and 21 nm.

The as-grown laser had a threshold current of 12 mA (J_{th} = 600 A/cm^2) and a slope efficiency of 0.52 W/A. A maximum output power of 14 mW at I = 4 x I_{th} was achieved. In comparison, the P-I-curve of the SiO_2-capped laser had a lower threshold current of 10 mA (J_{th} = 500 A/cm^2) while the SrF_2-capped

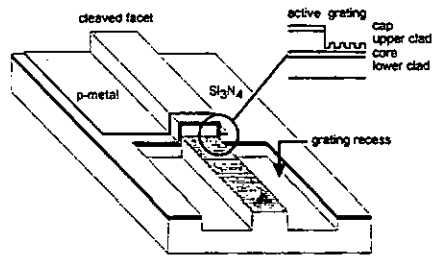

Fig. 2 - Schematic picture of a single-growth-step OBR laser with a holographically-defined, grating fabricated in a grating recess.

device had a somewhat higher threshold current of 14 mA (J_{th} = 700 A/cm^2). The slope efficiencies of the SiO_2-capped laser (0.42 W/A) and the SrF_2-capped laser (0.36 W/A) were lower than that of the as-grown laser. The higher thresbold current and lower slope efficiency of the SrF_2-capped laser were probably caused by repeated plasma exposure of its contact region during SiO_2 removal, SiO_2 patterning and Si_3N_4 patterning.

C. *DBR laser*

Numerous approaches have been developed for the integration of a laser with an optical circuit; these include evanescent coupling between waveguides and emitting regions (requiring an additional impedance matching layer and regrowth) [23], [24], butt coupling between laser and photodetector (needing a mirror dry etch technique) [25] or the use of surface emitting lasers and photodiodes (requiring high-quality dry-etched mirrors) [26]. For the present work, the use of a simplified, single-growth-step, two section DBR laser, described previously [27], [28], represents an attractive solution with respect to both process compatibility and feedback stability for an integrated interferometer.

The pumped section of the laser was fabricated in an area of the chip not subject to a bandgap shift during VED, while the Bragg reflector was etched into the shifted, thus transparent, region. The use of a so-called grating recess (see figure 2) allowed accurate vertical placement of the grating [28]; this recess was dry etched to within 150 nm of the active region, leaving an accurately-defined layer for the Bragg reflector. The holographically-defined 3rd order grating had a period of 375 nm, 1:1 line-to-space ratio and 100 nm depth. The 50 nm thick buffer layer between grating and waveguide core determined the coupling coefficient, approximately 100 cm^{-1}.

Performance evaluation of discrete DBR lasers was carried out CW at room temperature. As seen in the inset to figure 3, maximum output power was 5 mW from the cleaved facet, threshold current was 26 mA (J_{th} = 1.3 kA/cm^2) and slope efficiency was on

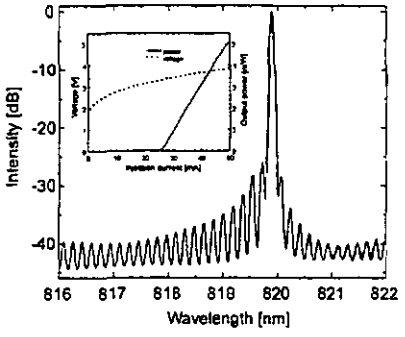

Fig. 3 - Optical spectrum of a DBR laser with a 500 μm long pumped and a 130 μm long grating section driven at 2.3 x I_{th}. The inset shows the I-V- and the P-I-curve.

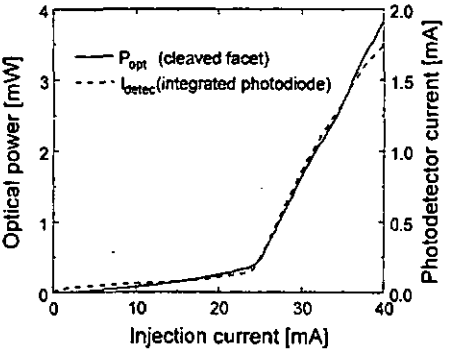

Fig. 4 - Cleaved facet optical output power and photodetector current versus laser injection current of a DBR laser monolithically integrated with a transparent waveguide and an absorbing photodetector.

the order of 0.21 W/A. The latter value could be further improved by ensuring a closer wavelength match between the Bragg peak of the grating (820 nm) and the semiconductor gain peak (825 nm). The laser spectrum, as shown in figure 3, was single transverse and longitudinal mode with a primary emission peak at λ = 820 nm and had a sidemode suppression ratio (SMSR) of 27 dB. Self-heterodyne measurements of the laser spectrum gave a spectral linewidth of 500 kHz.

From the Fabry-Pérot mode spacing of 0.16 nm, we could calculate the effective cavity length to be about 630 μm implying an active grating length of approximately 130 μm. The primary emission peak could be continuously temperature-tuned between 15 and 35 °C, leading to a temperature tuning coefficient of 0.06 nm/°C.

D. Integration: laser, waveguide and photodetector

To test the suitability of these DBR lasers and the VED technique for bandgap shifting described above, a simple optical circuit consisting of 500 μm long pumped laser sections, 130 μm long non-absorbing DBR reflectors, 570 μm long transparent waveguides and 500 μm long absorbing photodiodes was fabricated. The entire chip, 1700 μm long, was traversed by a single 4 μm wide waveguide.

As shown in figure 4, we simultaneously measured the cleaved facet output power with an external photodetector and the output power from the grating side of the laser with the integrated photodetector; for current values up to 35 mA, the two curves follow each other closely. Above this current level, the integrated photodetector seems to saturate, likely because no reverse bias voltage was applied. This operating condition was chosen because the resistance parallel to the reverse biased photodiode is about 5 kΩ and thus leakage currents were relatively high.

The wavelength-shifted waveguides had optical losses comparable to as-grown transparent waveguides and were on the order of 1.5 dB for the short lengths (0.57 mm) employed. Photodiodes of this design typically have a high responsivity (>0.6 A/W), implying >90 % quantum efficiency. If we assume that the laser output from the grating side (with reflectivity 30 - 40 %) and the cleaved facet side (reflectivity 31%) are roughly equal, we can determine a total conversion efficiency of laser output into detector current of 0.47 A/W; no obvious performance differences between annealed and non-annealed photodetectors were noted.

IV. INTERFEROMETER DESIGN AND CHARACTERIZATION

The optical circuits we describe in this paper were configured either as single Michelson interferometers (SMI), or as double Michelson interferometers (DMI); both of them are shown schematically in figures 5a and 5b. The SMI devices included a DBR laser, a photodetector, and waveguides forming a directional coupler, while the DMIs consisted of one DBR laser, two photodetectors, two Y-couplers, two directional couplers, and two phase shifters. The ridge width of the waveguides was 3 μm and all curve radii were 500 μm. The passive waveguides were fabricated in the areas with intermixed quantum wells and had, because of the relatively small bandgap difference of 45 meV between intermixed and non-intermixed sections, an absorption loss of 35 - 45 dB/cm. Since the total waveguide length did not exceed 3 mm, this relatively high absorption loss was not overly detrimental for interferometer performance. The total chip lengths were 1.95 mm for SMIs and 2.6 mm for DMIs.

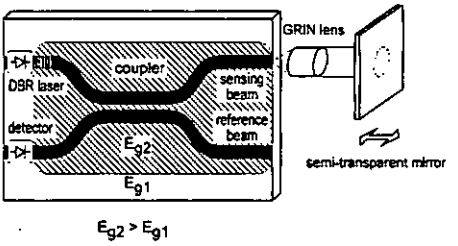

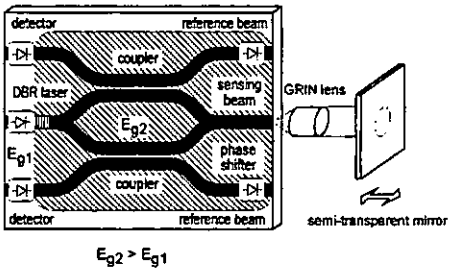

Fig. 5a - Schematic representation of a single Michelson interferometer for optical displacement measurement.

Fig. 5b - Schematic representation of a double Michelson interferometer for optical displacement measurement with direction determination.

Both the pumped laser section and photodetectors were fabricated in the non-intermixed, and thus absorbing, areas of the chip and had a length of 500 µm each. The length of the non-absorbing DBR grating section was 200 µm; here, we used a 3rd order grating with a period of 380 nm, a depth of 160 nm and 1:1 line-to-space ratio. A 70 nm thin buffer layer between the bottom of the grating and the waveguide core resulted in a calculated grating coupling coefficient of 100 cm^{-1}; this gave the desired grating reflection coefficient of about 95 %. The left cleaved facet of the interferometer served as the second laser mirror.

These interferometer chips were tested in bar form and were temperature-stabilized to within ±50 mK using a thermo-electric cooler. The measurement beam, collimated by an external GRIN lens (pitch = 0.23), was directed onto a semi-transparent, 67 % reflecting mirror through which the reflected beam position could be observed by a CCD camera. Observation was necessary to adjust the beam properly into autocollimation. By using a pitch of 0.23 instead of 0.25, we could prevent physical contact of the GRIN lens with the cleaved interferometer facet, reducing the probability of facet damage. The semi-transparent mirror was fixed to a piezo-driven, gimbal-mounted holder with which the measurement distance could be varied between 3 cm and 45 cm. Tilt control of this mirror was performed by piezo-

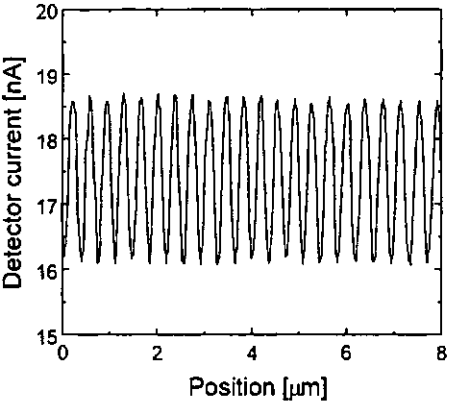

Fig. 6 - Interferogram for 3 cm mirror distance and 95 % mirror reflectance as measured by integrated photodetector using a SMI.

actuators, resulting in a tilt accuracy of 0.33 µrad/V in the horizontal and of 0.67 µrad/V in the vertical direction. With this arrangement, we were able to produce either a 20 µm unidirectional movemeot, or a movement with periodically (T = 60 s) changing direction. The unidirectional movement was used to test the SMIs and led to 49 interference fringes, each of them corresponding to a mirror movement of 410 nm (see figure 6). The displacement with periodical direction changes every 2 µm was used to measure the characteristics of a DMI.

V. SMI Performance

The photodetector of the SMI was reverse biased at -5 V and had a leakage dark current of 500 pA; responsivity of such detectors is typically 0.6 A/W. The electrical resistance between the laser diode and the adjacent photodiode was measured to be on the order of 10 GΩ. The measured interference signal is shown in figure 6; it exhibited a good temporal stability but was very sensitive to vibration of the external components. Displacements of a quarter of a fringe, or approximately 100 nm, were resolvable. With this single Michelson interferometer configuration, no determination of a change in movement direction is possible.

A large constant offset in the photodiode current, dominated by optical crosstalk between laser and photodiode, was seen. The interferometer signal, defined by

$$I(\phi) = I_{cross} + \frac{I_0}{2}\left(1 + V \cdot \cos\phi\right)$$

includes a constant offset in the detector current signal, I_{cross}, due to optical crosstalk between laser and detector, as well as a constant component $I_0/2$ due to visibility, $V = (I_{max} - I_{min})/(I_{max} + I_{min})$, less than unity. This crosstalk current was reduced, but not completely eliminated, by the isolation trench between laser and

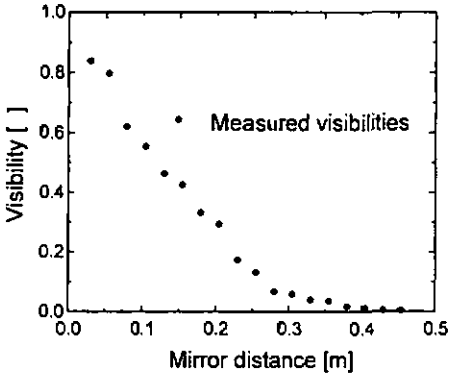

Fig. 7 - Signal contrast as a function of mirror distance using a 67 % reflecting mirror for the SMI.

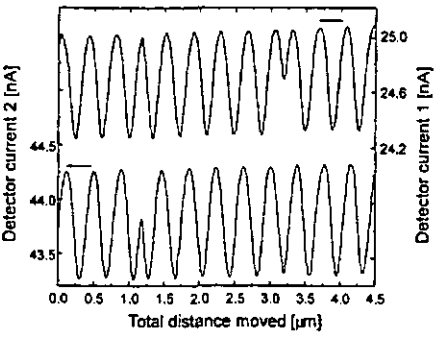

Fig. 8 - The two detector currents of the double Michelson interferometer for 3.5 cm mirror distance and 67 % mirror reflectance showing the two interference signals. Direction changes occurred at 1.2 µm and at 3.2 µm.

photodiode. To evaluate this offset curreot, we removed the external optics and measured the signal magnitude. Since we know the reflectivity of the AR-coated facet (~ 2 %), we were able to estimate a value of 15.8 nA for the crosstalk current from this measurement. This value agreed well with a more comprehensive measurement involving the use of five different external mirrors with differing reflectivities. Subtracting the crosstalk current from the signal values shown in figure 6 results in a considerably improved contrast (V = 0.8 instead of V = 0.1).

A plot of the corrected signal contrast (after subtraction of the crosstalk current) as a function of mirror distance is shown in figure 7. The Fourier-transformation of this auto-correlation function allows the estimation of the DBR laser linewidth; we calculated a value of 500 MHz, which is a factor of 10^3 larger than the value obtained with a discrete DBR laser. An investigation of the laser spectrum using a scanning Fabry-Perot resonator exhibited an irregularly flickering spectrum with approximately the linewidth calculated above, and not the expected broadened Lorentzian-shaped laser line. These observations indicate clearly that the laser sees numerous external cavities caused by facet reflections and tries to optimize their phase conditions. The short coherence length of the integrated DBR lasers therefore provides a fundamental system limitation; current work is focusing on the improvement of integrated laser linewidth.

VI. DMI Performance

The DMIs were characterized with the same setup as described above; the application of electrical bias to the phase shifters in the two reference arms allowed determination of changes in movement direction in addition to the magnitude of displacement. The DBR lasers operated at a current level of 60 mA and a reverse voltage of -12 V was applied to the photodetectors. The length of the phase shifters was 340 µm which gave a one-pass phase shift of $\pi/16$ when driven at -12 V bias voltage. Figure 8 presents the result of an interferometric measurement with a DMI at a mirror distance of 3.5 cm. Two changes of movement direction are clearly visible in the figure: one at 1.2 µm and another at 3.2 µm. Again, one interference fringe corresponds to a mirror movement of one half of the measurement wavelength, namely 410 nm. The amplitudes of the detector current signals, (I_0·V/2), were 0.5 nA and 0.4 nA, with optical crosstalk signals of 35 nA and 16 nA, respectively.

Plotting the two interferometer detector currents against each other resulted in the elliptical Lissajous-figure shown in figure 9. The ratio of the two normalized ellipse main axes allowed an estimate of the phase shift between the two reference signals, between 75 - 80°. Since one rotation (360°) of the characteristic corresponds to a mirror movement of 400 nm, we obtain a system measurement resolution of approximately 1.1 nm/°. If we conservatively estimate the angular interpolation to be limited to $\phi/20$, or 18°, an interferometer displacement resolution of 20 nm is easily achieved. A further improvement of the resolution can be achieved by using an exactly circular Lissajous characteristic; this requires a 90° phase shift between the two interference signals, achievable with a slightly longer phase shifter.

The slightly distorted sine- and cosine-shape of the two signals results from the parasitic reflection at the right cleaved facet of the sensing beam. This reflection at the measurement facet and the reflection at the object mirror generate a Fabry-Pérot interferometer cavity, whose electric field interferes with the one from the reference arm. We studied the behavior of such a three-mirror interferometer by simulation and were able to predict the asymmetric shape of the interferograms when changing the intrinsic phase between reference and sensing arm, as

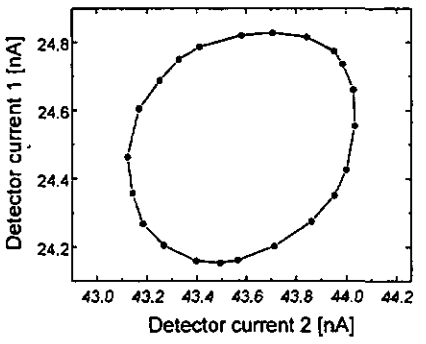

Fig. 9 - The two detector currents of the double Michelson interferometer for 3.5 cm mirror distance and 67 % mirror reflectance plotted as a function of each other; the signal rotates around the figure at a rate of 1.1 nm/°.

seen experimentally and in agreement with a similar, more comprehensive study in the literature [29].

The maximum measurement distance for the DMI was 25 cm, corresponding to a laser linewidth of about 1 GHz. In addition to optical feedback into the laser, the modal behavior of the sensing beam waveguide was not ideal; higher order waveguide modes could be observed under different coupling conditions. This effect further reduced the contrast and gave rise to occasional "mode hopping", which was clearly indicated by spontaneous changes of the phase between the two interferometer signals.

VII. Conclusions

Monolithically integrated single Michelson interferometers and double Michelson interferometers for contactless optical displacement measurement and direction determination have been demonstrated. The devices consisted of a DBR laser, detectors, modulators and waveguides, all fabricated on a single GaAs/AlGaAs-chip. Displacement measurements were performed using only one external element for beam collimation and a movable mirror as measurement object.

The monolithic double Michelson interferometer was demonstrated to have a displacement resolution of 20 nm for measurement distances of up to 5 cm. In comparison, 250 nm displacement resolution at distances of 25 cm have been reported for non-monolithic integrated optical implementations [7], [9] and 1 nm resolution, at a distance of several centimeters, has been reported [8] for a glass-based double interferometer. A 100 nm resolution for short distances has also been demonstrated for a monolithic interferometer [12], but without phase-shift between the measurement signals.

Concerning design improvements, we expect a considerable crosstalk reduction by etching an isolation trench with a depth of at least 800 nm and subsequent p-metal coating of the trench sidewalls. Furthermore, a maximized laser output power and a symmetric splitting ratio of the directional couplers will result in larger detector signals without increasing feedback of light into the laser cavity. Finally, AR-coated facets may reduce feedback and help to enlarge the coherence length of the laser.

Possible applications for this device are short range displacement measurements in microsystems, in order to monitor the deflection of an AFM cantilever or the movement of a diaphragm. A further interesting area of application is displacement measurement at longer distances, for example in height gauges or in precision machine tools. For both of the above applications, a measurement resolution of 10^{-6}, achieved by locking the laser frequency on a Cs or Rb absorption line, would be necessary.

VIII. Acknowledgments

The authors are grateful to J.E. Epler and H.P. Schweizer for crystal growth; P. Riel, D. Jeggle and A. Vonlanthen for processing assistance; Y. Salvadé for laser linewidth measurements; J. Söchtig for valuable discussions; and M.T. Gale and H.W. Lehmann for their generous support.

IX. References

[1] A.A. Michelson, "The relative motion of the earth and the luminiferous ether", *Amer. J. Sci.*, vol. 22, pp. 120 - 129, 1881

[2] A.A. Michelson, "On the application of interference methods to spectroscopic measurements", *Phil. Mag.*, vol. 34, pp. 280 - 299, 1892

[3] M. Born and E. Wolf, "Interference and interferometers", *Principles of optics*, Oxford, Pergamon Press, 6th edition, 1984, pp. 256 - 323, 1984

[4] F.T. Arecchi and A. Sona, "Long distance interferometry with a He-Ne-laser", *Journal of Applied Physics and Mathematics*, vol 16, pp. 128 - 129, 1965

[5] H.P. Zappe, H.E.G. Arnot, and R.E. Kunz, "Technology for III-V-based integrated optical sensors", *Sensors and Materials*, vol. 6, pp. 261 - 270, 1994

[6] D. Hofstetter, H.P. Zappe, and R. Dändliker, "Monolithically integrated optical displacement sensor in GaAs/AlGaAs", *Electron. Lett.*, vol 31, pp. 2121 - 2122, 1996

[7] D. Hofstetter, H.P. Zappe, and R. Dändliker, "A monolithically integrated double Michelson interferometer for optical displacement measurement with direction

determination", to appear in *IEEE Photonics Technol. Lett.*, vol. 8, October 1996

[8] G. Ulbers, "An integrated optics sensor on silicon for the measurement of displacement, force and refractive index", *Proc. SPIE*, vol. 1506 "Micro-Optics II", pp. 99 - 110, 1991

[9] Hommelwerke Sensor GmbH, Laser interferometer HC 250

[10] D. Jestel, A. Baus and E. Voges, "Integrated-optic interferometric microdisplacement sensor in glass with thermo-optic phase modulation", *Electron. Lett.*, vol. 26, pp. 1144 - 1145, 1990

[11] G. Voirin, L. Falco, O. Boillat, O. Zogmal, P. Regnault and O. Parriaux, "Monolithic double interferometer displacement sensor with wavelength stabilization", *Proc. European Conference of Integrated Optics 93*, pp. 12-28 - 12-29, 1993

[12] T. Suhara, T. Taniguchi, M. Uemukai, H. Nishihara, T. Hirata, S. Iio, and M. Suehiro, "Monolithic integrated-optic position/displacement sensor using waveguide gratings and QW-DFB laser", *IEEE Photonics Technol. Lett.*, vol. 7, pp. 1195 - 1197, 1995

[13] S. Ura, T. Suhara and H. Nishihara, "Integrated-optic interferometer position sensor", *IEEE J. Lightwave Technol.*, vol. 7, pp. 270 - 273, 1989

[14] K. Yamaguchi, K. Okamoto, and T. Imai, "Selective area growth of GaAs by metalorganic chemical vapor deposition", *Jpn. J. Appl. Phys.*, vol 24, pp. 1666 - 1671, 1985

[15] D. Trommer, "Photonic integration on InP", *Proc. ECIO'95 (Delft, The Netherlands)*, pp. 93 - 98, 1995

[16] R.M. Lammert, T.M. Cockerill, D.V. Forbes, and J.J. Coleman, "Dual-channel strained-layer InGaAs/GaAs/AlGaAs WDM source with imegrated coupler by selective-area MOCVD", *IEEE Photonics. Technol. Lett.*, vol. 6, pp. 1167 - 1169, 1994

[17] D. Remiens, B. Rose, M. Carre, and V. Hornung, "GaInAsP/InP integrated ridge laser with a butt-joined transparent optical waveguide fabricated by single-step metalorganic vapor-phase epitaxy", *J. Appl. Phys.*, vol. 68, pp. 2450 - 2453, 1990

[18] V. Hornung, D. Remiens, D. Robein, A. Gloukhian, and M. Carre, "Simple approach for monolithic integration of DFB laser and passive waveguide", *Electron. Lett.*, vol. 27, pp. 1683 - 1685, 1990

[19] K. Meehan, P. Gavrilovic, N. Holonyak, Jr., R.D. Burnham, and R.L. Thornton, "Stripe-geometry $Al_xGa_{1-x}As$ quantum well heterostructure lasers defined by Si diffusion and disordering", *Appl. Phys. Lett.*, vol. 46, pp. 75 - 77, 1985

[20] R.L. Thornton, J.E. Epler, and T.L. Paoli, "Monolithic integration of a transparent dielectric waveguide into an active laser cavity by impurity-induced disordering", *Appl. Phys. Lett.*, vol. 51, pp. 1983 - 1985, 1987

[21] J. Beauvais, S.G. Ayling, and J.H. Marsh, "Low-loss extended cavity lasers by dielectric cap disordering with a novel masking technique", *IEEE Photon. Technol. Lett.*, vol. 4, pp. 372 - 373, 1993

[22] D. Hofstetter, H.P. Zappe, J.E. Epler and P. Riel, "Multiple wavelength Fabry-Pérot lasers fabricated by vacancy-enhanced quantum well disordering", *Appl. Phys. Lett.*, vol. 67, pp. 1978 - 1980, 1995

[23] R.J. Deri, W. Doldissen, R.J. Hawkins, R. Bhat, J.B.D. Soole, L.M. Schiavone, M. Seto, N. Andreadakis, Y. Silberberg and M.A. Koza, "Efficient vertical coupling of photodiodes to InGaAsP rib waveguides", *Appl. Phys. Lett.*, vol. 58, pp. 2749 - 2751, 1991

[24] K.-Y. Liou, U. Koren, E.C. Burrows, M. Oron, B.J. Miller, M. Young, G. Raybon and C.A. Burrus, "Operation of integrated InGaAsP/InP optical amplifier-monitoring detector with feedback control circuit", *IEEE Photon. Technol. Lett.*, vol 2, pp. 878 - 880, 1990

[25] P. Vettinger, M.K. Benedict, G.-L. Bona, P. Buchmann, E.C. Cahoon, K. Dätwyler, H.-P. Dietrich, A. Moser, H.K. Seitz, O. Voegeli, D.J. Webb and P. Wolf, "Full-wafer technology - a new approach to large-scale laser fabrication and integration", *IEEE J. Quantum Electron.*, vol. QE-27, pp. 1319 - 1331, 1991

[26] C.-H. Chen and S.-C. Lee, "Monolithic integration of an AlGaAs/GaAs surface emitting laser diode and a photodetector", *Appl. Phys. Lett.*, vol. 59, pp. 3592 - 3594, 1991

[27] D. Hofstetter, H.P. Zappe, J.E. Epler and J. Söchtig, "Single-growth-step GaAs/AlGaAs distributed Bragg reflector lasers with holographically-defined recessed gratings", *Electron. Lett.*, vol. 30, pp. 1858 - 1859, 1994

[28] D. Hofstetter, H.P. Zappe and J.E. Epler, "Ridge waveguide DBR lasers with nonabsorbing grating and transparent integrated waveguide", *Electron. Lett.*, vol. 31, pp. 980 -982, 1995

[29] W.E. Ward, Z. Pasturczyk, W.A. Gault, and G.G. Shepherd, "Multiple reflections in a wide-angle Michelson interferometer", *Applied Optics*, vol. 24, pp. 1589 - 1598, 1985

CURRICULUM VITAE

Daniel Hofstetter-Hefti

Born on December 31, 1966

Married to Gabriela Hofstetter-Hefti, one child

Citizen of Schänis SG, Switzerland

1973 - 1979	Primary School in Oberwil ZG
1979 - 1982	Secondary School in Zug
1982 - 1986	Apprenticeship as an electrical mechanic at Landis & Gyr in Zug
1986	Swiss Army Service
1986 - 1988	Employee as a physics technician at Landis & Gyr in Zug
1988	Comprehensive entrance examination at ETH Zurich
1988 - 1993	Studies of Physics at ETH Zurich
1993	Dipl. phys. ETH
1993 - 1996	PhD work under the supervision of H.P. Zappe and R. Dändliker at the Paul Scherrer Institute in Zurich
1996	PhD thesis entitled "Monolithically integrated interferometer for optical displacement measurement"